

**EVALUATION OF MEASURED AND FACIES-BASED EFFECTIVE PERMEABILITY AND  
THE SIGNIFICANCE FOR RESERVOIR MAPPING AND CONNECTIVITY**

**by**

**CHRISTOPHER MICHAEL RYBOWIAK**

**B.A., University of Colorado at Boulder, 2010**

A thesis submitted to the  
Faculty of the Graduate School of the  
University of Colorado in partial fulfillment  
Of the requirement for the degree of  
Master of Science  
Department of Geological Sciences

2012

This thesis entitled:  
Evaluation of Measured and Facies-Based Effective Permeability and the Significance for  
Reservoir Mapping and Connectivity  
written by Christopher Michael Rybowski  
has been approved for the Department of Geological Sciences.

---

Matthew J. Pranter

---

David A. Budd

---

Shemin Ge

Date \_\_\_\_\_

The final copy of this thesis has been examined by the signatories, and we  
find that both the content and the form meet acceptable presentation standards of  
scholarly work in the above mentioned discipline.

Rybowiak, Christopher M. (M.S., Geology [Department of Geological Sciences])

Evaluation of Measured and Facies-Based Effective Permeability and the Significance for Reservoir Mapping and Connectivity

Thesis directed by Associate Professor Matthew J. Pranter

This study addresses how reservoir-scale permeability models vary depending on the scale of investigation of the input permeability values. A common practice in reservoir modeling is to directly use permeability measurements from core-plugs or probe permeametry in petrophysical modeling. Three-dimensional permeability model cells are often several orders of magnitude larger than the scale of investigation (volume support) of the permeability measurement. This scale difference can produce unrealistic results in the permeability model which may not be representative of the reservoir heterogeneity.

To explore this issue, 3-D core lithofacies and permeability models of the Terry Formation in the Denver Basin, Colorado were created with permeability values measured using a mini-probe permeameter. These measured-permeability values were acquired by facies and lamina type and flow-based upscaling was used to generate effective-permeability values by facies. After upscaling, the range of permeability is reduced, and the average permeability is decreased by as much as 50%.

Using the original- and effective-permeability values, the significance of fine-scale permeability heterogeneity associated with lithofacies that exist below the resolution of reservoir model cells was investigated through comparative analysis of field-scale, 3-D permeability models and resulting static connectivity of permeability distributions. Statically connected reservoir volumes to producing wells defined by permeability cutoffs shows that for relatively lower permeability cutoffs, there is a distinct difference in connected volume between original- and effective-permeability models. In some cases, this difference is 50% lower for connectivity in the effective-permeability model. This is significant because it represents the reservoir

volume connected to wells for potential production. As the permeability cutoff (reservoir definition) increases, static connectivity decreases and the differences between the original- and effective-permeability models is reduced. The differences between original- and effective-permeability values and models indicate why it is important to utilize scale-dependent, facies-based permeability values for reservoir mapping at the field scale.

## **Dedication**

I would like to dedicate my thesis to my family, Mike, Susie and Sarah. Without your support and encouragement over the years I would not be where I am today or finishing this thesis.

## Acknowledgements

I would like to thank many people who have helped me complete this research over the last two years. First I would like to thank my advisor, Dr. Matthew Pranter for his patience, encouragement, and guidance throughout the project and for revising this thesis. I'd also like to acknowledge my thesis committee, Dr. David Budd and Dr. Shemin Ge for their input and guidance in completing my thesis.

I'd like to thank Stephen Hilfiker and Patrick Boulas for their assistance in collecting permeability data. Without their hard work and patience in taking measurements this thesis would not have been completed. They put in many hours of hard work in order to collect all of the data necessary to complete this work.

Many professionals also contributed to this thesis and I would like to thank them for their assistance and input. Dr. Gus Gustason, Scott Larson, and Louise Kiteley provided invaluable information on core and outcrop analysis on the Terry and Hygiene Formations. I'd like to thank Louise Kiteley for taking time and securing permission to look at Terry Formation outcrops in Colorado. I would like to thank the many people who provided data for this project including: Marshall Deacon of Noble Energy, Sara Smaltz of EnCana, and Steve Kuntz of Anadarko for providing digital well-log data for this project and to the United States Geological Survey (USGS) for allowing us to collect permeability data on one core.

Software was provided by several companies for this project; SBED by Geomodeling Corporation and Petrel by Schlumberger. I would like to thank Tofer Lewis of EnerPlus who helped in setting up software, projects, and answered numerous software questions. I would also like to thank Les Dabek and Rex Knepp of Geomodeling Corporation for providing exceptional technical support and information on the use of SBED.

I'd like to thank my fellow office mates over the last two years for their help and support through all of this including: Rob Jaecks, Gabriela Keeton, Kim Hlava, Ali Sloan, Sait Baytok, Whitney Mathias, John McFadden, Daniel Allen, Tuba Evsan, Aya Attar, and Ellen Wilcox.

This thesis was conducted at the Reservoir Characterization and Modeling Laboratory in the Department of Geological Sciences at the University of Colorado at Boulder. Funding was supplied through the National Energy Technology Laboratory under the U.S. Department of Energy and by the Department of Geological Sciences at the University of Colorado at Boulder. Funding was also provided in part by the Shell Student Ambassador Scholarship through the Department of Geological Sciences at the University of Colorado at Boulder. Without the support of these groups, this thesis would not have been possible.

## Contents

ABSTRACT.....	iii
DEDICATION.....	v
ACKNOWLEDGEMENTS.....	vi
CONTENTS.....	viii
LIST OF TABLES.....	x
LIST OF FIGURES.....	xi
I.    INTRODUCTION.....	1
II.   GEOLOGIC SETTING.....	6
III.  FACIES AND RESERVOIR STRATIGRAPHY.....	9
IV.  FINE SCALE FACIES AND PERMEABILITY MODELING AND UPSCALING.....	12
V.   FIELD-SCALE 3-D FACIES, POROSITY, AND PERMEABILITY MODELING.....	22
VI.  STATIC CONNECTIVITY.....	31
VII. DISCUSSION.....	37
a.  FACIES.....	37
b.  PERMEABILITY UPSCALING.....	37
c.  STATIC CONNECTIVITY.....	39



VIII.	CONCLUSIONS.....	39
	REFERENCES.....	42
	APPENDIX.....	46
	a. APPENDIX A: FACIES AND CORE DESCRIPTIONS.....	46
	b. APPENDIX B: PERMEABILITY ACQUISITION AND RESULT .....	64
	c. APPENDIX C: UPSCALING AND UPSCALING RESULTS.....	85
	d. APPENDIX D: FIELD-SCALE MODELING.....	103
	e. APPENDIX E: STATIC CONNECTIVITY.....	119

**LIST OF TABLES:**

Table 1: Original- and Effective-Permeability Values for McHale #1 Core (Terry Formation)...18

Table 2: Static Connectivity Percentages for Permeability Analysis.....33

Table 3: Original- and Effective-Permeability Values for Champlin 369 Core (Hygiene Formation).....92

Table 4: Effective-Permeability Values by Depth for McHale #1 Core (Terry Formation).....95

Table 5: Effective-Permeability Values by Depth from Champlin 369 Core (Hygiene Formation).....98

Table 6: Formation Tops and Stratigraphic Horizons for Model Wells.....105

Table 7: Layering scheme sorted by zone within the 3-D model framework.....107

Table 8: Variogram Analysis of Facies Log determined from McHale #1 core.....110

Table 9: Variogram Analysis of Porosity Log from McHale #1 core.....115

Table 10: Static Connectivity Volumes and Percentages of Terry Formation 3-D Reservoir Models.....121

Table 11: Reservoir-Defined Volumes and Percentages of Terry Formation 3-D Reservoir Models.....122

Table 12: Pore Volumes and Percentages of Terry Formation 3-D Reservoir Models.....125

**LIST OF FIGURES:**

Figure 1: Denver Basin and Core Location Map.....	4
Figure 2: Model Area Location and Data Map.....	5
Figure 3: Stratigraphic Section of Spindle Field, Denver Basin.....	8
Figure 4: Lithofacies Chart.....	10
Figure 5: Type Well for the Terry Formation, Denver Basin.....	11
Figure 6: N-S, E-W Cross-Section Through Model Area.....	13
Figure 7: Comparison of Fine-Scale Facies and Permeability Models to Core Photographs....	16
Figure 8: Histograms of Original- and Effective-Permeability Values for Terry and Hygiene Formations.....	21
Figure 9: Three-Dimensional Model Framework and Cell Size.....	23
Figure 10: Three-Dimension Sandstone Probability Volume Model.....	25
Figure 11: Three-Dimensional Facies Models.....	27
Figure 12: Three-Dimensional Porosity Models.....	28
Figure 13: Three-Dimensional Permeability Models.....	30
Figure 14: Static Connectivity Percentage Graphs.....	34
Figure 15: Cross-Sectional View of Static Connectivity.....	35
Figure 16: Denver Basin Structural Boundaries.....	48
Figure 17: Core Description of McHale #1.....	49
Figure 18: Core Description of Champlin 369.....	50
Figure 19: Facies Percentage in McHale #1 Core.....	53
Figure 20: Facies Percentage in Champliln 369 Core.....	54
Figure 21: Paleogeographic Map during Terry Formation Deposition.....	57
Figure 22: Depositional Environment Schematic.....	58
Figure 23: Well Log Interpretation Chart.....	59
Figure 24: Stratigraphic Nomenclature Chart for Denver Basin.....	61

Figure 25: McHale #1 Core Photographs with Reservoir Zonation.....	63
Figure 26: Permeameter Calibration Chart.....	67
Figure 27: McHale #1 Permeability Data.....	70
Figure 28: Champlin 369 Permeability Data.....	74
Figure 29: Sidwell #1 Permeability Data.....	77
Figure 30: Moser #1 Permeability Data.....	81
Figure 31: Comparison of Core Photograph, 3-D Facies Model, 3-D Measured Permeability Model, and Upscaled Permeability Values for McHale #1 Core.....	87
Figure 32: Boundary Conditions for Permeability Upscaling.....	91
Figure 33: Histogram of Original-Permeability Data by Facies for Terry Formation.....	99
Figure 34: Histogram of Effective-Permeability Data by Facies for Terry Formation.....	100
Figure 35: Histogram of Original-Permeability Data by Facies for Hygiene Formation.....	101
Figure 36: Histogram of Effective-Permeability Data by Facies for Hygiene Formation.....	102
Figure 37: Mudrock Probability Volume Model.....	108
Figure 38: Histogram for Facies Distribution in Well Log, Upscaled Logs, and 3-D Model Cells.....	111
Figure 39: Location Map of Water Supply and Storage Reservoir Number 3.....	113
Figure 40: Histogram for Porosity Distribution in Well Log, Upscaled Logs, and 3-D Model Cells.....	114
Figure 41: Well Log and Permeability Cross-plots.....	116
Figure 42: Porosity-Permeability Cloud Transformation Cross-plots.....	118
Figure 43: Cross-sectional Representation of Reservoir Volume Percentage.....	124

## Introduction

Sandstone reservoirs commonly contain heterogeneities at different scales that are related to the stratigraphic framework, lithofacies, and sedimentary structures. At the bedding and lithofacies scale, it has been shown that sedimentary structures have a significant control on porosity and permeability heterogeneity and associated fluid flow (e.g., Weber, 1982; Hurst and Rosvoll, 1991; Corbett and Jensen, 1993; Jackson et al. (2003). Therefore, to model fluid flow through reservoirs, it is essential to model the spatial distribution of permeability that is tied to stratigraphy and lithofacies. For 3-D reservoir permeability modeling, it is common to directly use measurements obtained from core plugs or minipermeametry. Yet the volume of a 3-D reservoir model cell (>6 million in<sup>3</sup> [ $\sim 10^8$  cm<sup>3</sup>]) is typically several orders of magnitude greater than the volume evaluated through minipermeametry or the volume of a core plug (0.18-1.8 in<sup>3</sup> [3-30 cm<sup>3</sup>]) (Jackson et al., 2003). If not properly accounted for, the scale difference can produce unrealistic results in the 3-D permeability model that are not representative of the reservoir heterogeneity. This study addresses relationships between probe permeameter-based measurements and upscaled values of permeability due to the differences in scale of volumes associated with the permeability measurements and reservoir model cells. In addition, the significance of fine-scale permeability heterogeneity associated with lithofacies that exist below the resolution of reservoir model cells is investigated through comparative analysis of 3-D permeability models and resulting static connectivity of permeability distributions.

To create 3-D reservoir permeability models using data that are measured at the lamina scale, permeability values should be upscaled to account for the volume difference between the lamina and the size of a typical geologic-model cell. Similar studies have focused on the integration of small-scale core plug or minipermeameter measurements and wire-line well-log data (Haldorsen, 1986; Worthington, 1994; Nordahl et al., 2005). The scaling of permeability (or any property) in this study is referred to as upscaling which results in the generation of an effective property. Upscaling refers to the process of transforming a fine-scale grid that contains

many data points, into a coarser grid using averaging techniques, flow-based simulation, or other methods (Wen and Gomez-Hernandez, 1996). Effective permeability, as used in this study, is described as “the permeability of a homogeneous block which, under the same boundary conditions, will give the same average flows as the region the block is representing” (Pickup et al., 1994; p. 230). Some properties, such as porosity, can be upscaled by using an arithmetic average; however, permeability data should not be upscaled using an arithmetic average as it is not an additive property (Tidwell and Wilson, 1997; Renard and de Marsily, 1997; de Marsily et al., 2005; Nordahl and Ringrose, 2008). Common methods to upscale permeability include using a flow-based simulation to generate a property (e.g. flow-based upscaling or flow-based scale averaging), Monte-Carlo analysis, and data inversions related to solving of flow equations through a small-scale (measurement-scale) embedded in the upscaling block (Wen and Gomez-Hernandez, 1996; Tidwell and Wilson, 1997; de Marsily et al., 2005; Nordahl et al., 2005; Ringrose et al., 2005).

A probe-type permeameter was chosen for this study because it is useful for relatively rapid and accurate data acquisition (Tidwell and Wilson, 1997, Ringrose et al., 2005), and to obtain permeability measurements on lamina (bedding) that are smaller in scale than the dimensions of a core plug. Others have used similar approaches, including Corbett and Jensen (1993) who used a probe-permeameter and upscaling of the fine-scale grid into a coarse grid. While their specific method for upscaling is different, the overall process is similar in that they collected permeability data and used numerical simulations to generate effective properties. Corbett and Jensen (1993) focused on lamina-scale structures for their measurements and have shown that data collected at this scale and upscaled correctly leads to different flow characteristics in the reservoir. Ringrose et al. (2005) detailed a similar approach to the one used in this study for evaluation vertical permeabilities. Permeability data were acquired from laminated Brent Group cores in the North Sea using a probe-permeameter and upscaled using a similar flow-based upscaling algorithm. They showed that effective permeabilities generated

using this approach are better for characterization of oil reservoirs than permeability estimates derived from well logs using numerical calculations. Other previous works that have used processes similar to ones outlined in this study include; Durlofsky (1991), Corbett and Jensen (1993), Ringrose et al. (1993), Tidwell and Wilson (1997), Jackson et al. (2003), and Nordahl et al. (2005). Many of these papers have shown that small-scale sampling of data and upscaling are needed to preserve the permeability anisotropy in the large-scale models.

The study area is located within Spindle Field in the Denver Basin, Colorado (Figures 1 and 2). Spindle Field is one of the oldest producing fields in Colorado, having been discovered and producing since 1971 (Porter and Weimer, 1982; Weimer, 1996). It is the second largest oil and gas field in the basin and has produced over 49.2 million barrels (7.9 billion liters) of oil and over 236 billion ft<sup>3</sup> (6.7 billion m<sup>3</sup>) of natural gas (Weimer, 1996). Within Spindle Field, the Cretaceous Terry and Hygiene formations are two heterogeneous siliciclastic formations that form petroleum reservoirs and are the focus of the analysis in this study. Spindle Field was chosen given the relative abundance and availability of data (digital well and core data) and data density. The data set includes four cores (263 ft [80.1 m] total length) from either Spindle Field or the surrounding area (Figure 1), digital and raster well-log data for 9 wells (Figure 2), 832 minipermeameter measurements by lithofacies that were acquired from the cores, and 1539 minipermeameter measurements acquired from core-plug standards for calibration as part of this study (Appendix B). Two of the cores penetrate the stratigraphically higher Hygiene Formation and three penetrate all or part of the Terry Formation (the Champlin # 369 well samples both formations). Probe permeametry was conducted on individual lamina of sedimentary structures on the 4 cores to determine average permeability values for sandstone and mudrock lamina. Two of the four cores (one Terry Formation and one Hygiene Formation) were modeled using a near-wellbore modeling program to create a fine-scale (inch-scale) model of sedimentary structures in each formation. These models were populated with permeability data acquired from the probe permeameter and upscaled using a flow-based simulation

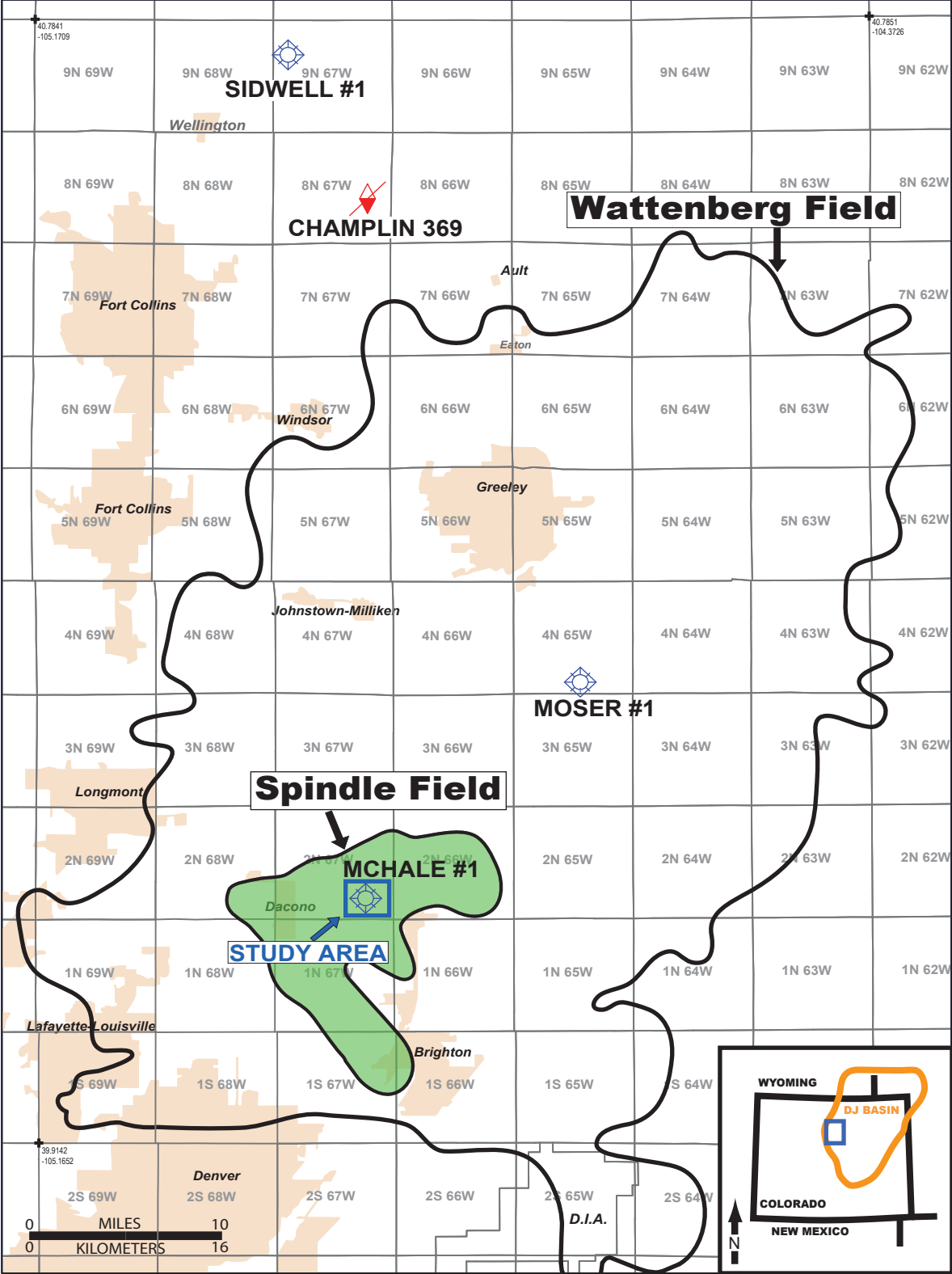


Figure 1. Location map of study area in Spindle Field, Denver Basin, Colorado. Blue box on inset map shows location of the area within the DJ Basin. Wattenberg Field outline from Colorado Oil and Gas Conservation Commission website.



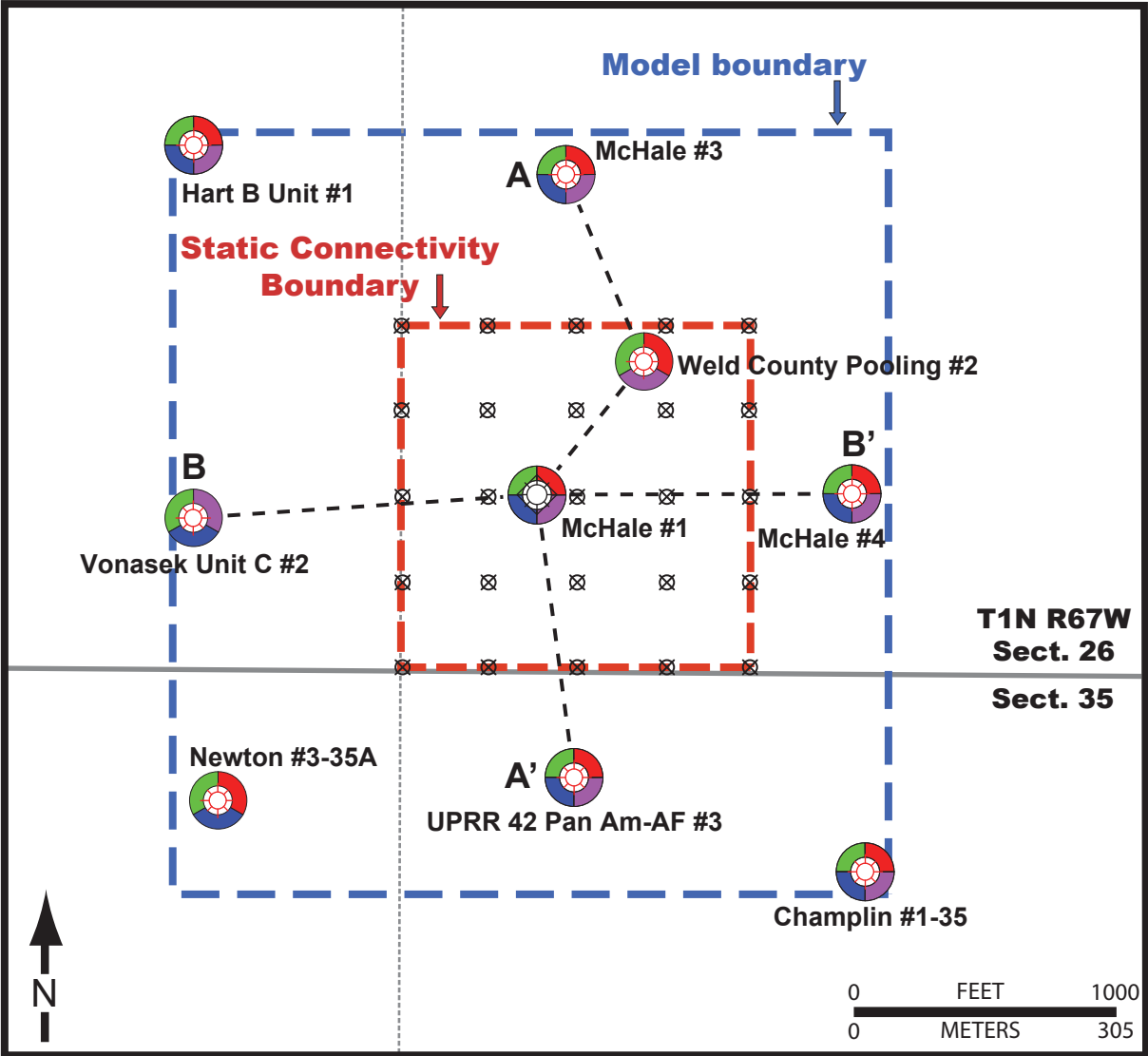


Figure 2. Detailed study area showing well locations with logs present along with static connectivity analysis boundary and pseudowells (⊗) on a 5-ac (2-hectacre) spacing. Distance between wells = 330 ft (100.5 m). Color ring around each well corresponds to the logs present in the Terry Formation. Green=gamma-ray, blue=density porosity, purple=resistivity, red=spontaneous potential. See Figure 1 for location of this area in Spindle and Wattenberg fields. Cross-sections of Figure 6 are shown by dashed lines.

algorithm to generate an effective property. The flow-based upscaling procedure creates an effective permeability value for each facies in the fine-scale model. In order to compare how the effective-permeability values compare to the measured values, the two are evaluated separately through static connectivity analysis. To do this, facies models along with porosity and both types of permeability models were created using well-log and core data (Figure 2). Pseudo-wells were used with a 5-ac (2-hectacre) spacing (Figure 2) and static connectivity to these wells was determined for a series of porosity and permeability cutoffs to compare the differences in permeability variation and connectivity between models based on probe-permeameter measurements (directly) and upscaled values of permeability.

### **Geologic Setting**

The Denver Basin is a Cretaceous foreland basin that spans most of eastern Colorado and southeastern Wyoming (Figure 1; Moredock and Williams, 1976; Pittman, 1989; Weimer, 1996; Higley et al., 2003). The basin was formed as part of the Laramide Orogeny when the basin was downwarped as a result of uplift and movement along basement Precambrian faults (Raynolds, 2002). The basin is classified as a Laramide perimeter basin with a broad asymmetric bowl shape that stretches onto the mid-continent (Dickinson et al., 1988; Pittman, 1988). The basin is bounded on the east by the Front Range portion of the Rocky Mountains but has no definitive structural boundary in the east (Weimer 1996, Dickinson et al., 1988). In the south, the basin is separated from the Raton Basin by the Apishapa Arch (Appendix A). The northern portion of the basin is bounded by the Hartville uplift and Cambridge-Chadron Arch in present day Wyoming. The northern half of the basin is also subdivided by the Greely Arch and creates the Cheyenne sub-basin.

Prior to the Laramide Orogeny, the area that is the Denver Basin was a coastal plain that followed the draining of the Cretaceous Western Interior Seaway (Raynolds, 2002). The uplift of the Rocky Mountains disrupted this coastal plain system and separated it into an eastern and

western section (Dickinson et al., 1988). As the basin formed, sediments were shed from the newly forming Rocky Mountains and other areas and began filling the basin with continental and marine sediments. The sediments were sourced from as far away as present day Utah and Nevada (Kiteley, 1977; Helsley, 1985; Dickinson et al., 1988).

The Terry and Hygiene formations are both members of the prolific Late Cretaceous Pierre Shale located throughout the Denver Basin (Figure 3). The Terry and Hygiene formations have been interpreted as offshore bars (shelf sandstones), beach deposits (shoreface sandstones), and deltaic sediments deposited in the Cretaceous Western Interior Seaway (Weimer, 1976; Kiteley, 1977; Porter and Weimer, 1982; Pittman, 1988, 1989; Imam, 1989; Al-Raisi et al., 1996; Weimer, 1996; Slatt et al., 1997; Ladd, 2005; E. R. Gustason, 2012, personal communication). One hypothesis is that both formations are shelf sandstones that were sourced from the Parkman or time equivalent delta in Wyoming (Kiteley, 1977; Imam, 1989; Porter and Weimer, 1982; Appendix A). Al-Raisi et al. (1996) suggests the Terry Formation was deposited as discrete sandstone bars near a delta whereas Porter and Weimer (1982) suggest that southerly moving storms would have transported sediments from the delta and moved them the distance of approximately 80 mi (133 km) to where the Terry and Hygiene formations both exist today. There is however no direct evidence of storm transportation or any other significant transportation mechanism beyond tidal forces to show how the sediments were moved or that they could have been moved over a great difference distance.

The Late Cretaceous Terry and Hygiene formations in the Denver Basin are commonly referred to as the Sussex and Shannon formations respectively (Kiteley, 1977; Porter and Weimer, 1982; Helsley, 1985; Pittman, 1988, 1989). However, based on biostratigraphic evidence, the Sussex and Shannon formations (of the Powder River Basin) are not time equivalent to the Terry and Hygiene formations of the Denver Basin (Appendix B; Kiteley, 1977). The stratigraphic terminology of Kiteley (1975, 1977) is used in this study for the Terry and Hygiene formations of the Pierre Shale in the Denver Basin (Appendix B).

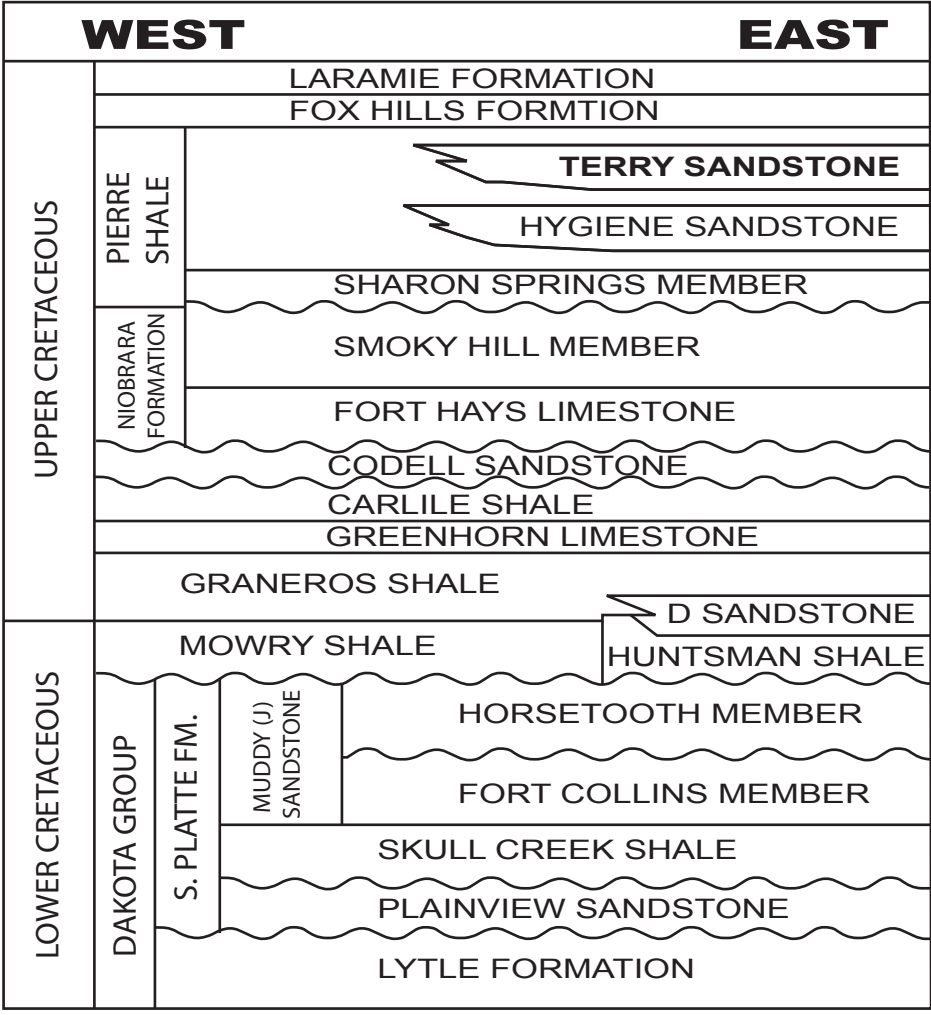


Figure 3. Stratigraphic column for Wattenberg Field, Denver Basin, Colorado. Modified from Higley et al., 2003.

## Facies and Reservoir Stratigraphy

Four lithofacies are interpreted for the Terry and Hygiene formations: wavy-laminated sandstone, planar cross-laminated sandstone, structureless sandstone, and ripple cross-laminated sandstone (Figure 4). The facies are identified based on lithology and sedimentary structures and do not take into consideration the degree of bioturbation. However, bioturbation is prevalent throughout the entire cored interval in both the Terry and Hygiene formations. Among the trace fossils identified in this study and others, the most common are asterosoma, teichichnus, planolites, and paleophycus. Other fossils identified in this area are shown in appendix A figures and are also noted by Helsley (1985).

The Terry and Hygiene formations are both used to evaluate the upscaling effects on permeability. However, the comparison of the two permeability types, measured and upscaled, through static connectivity is only completed on the Terry Formation. As a result, only detailed information on the Terry Formation including reservoir zonation and log response is discussed. Information on the Hygiene Formation upscaling results is presented separately.

The Terry Formation in this area is divided into two reservoir and two non-reservoir zones. The top of the Terry Formation was determined based on core observations (Appendix A) from the McHale #1 well and exhibits a relatively gradational change from interbedded sandstone and mudstone layers to a dominantly sandstone section. The base of the Terry Formation was also determined from the same core and exhibits a fairly sharp contact between the sandstone facies of the Terry Formation and offshore, heavily bioturbated mudstones of the Pierre Shale. Within the Terry Formation, three additional horizons are interpreted based on log responses and core observations that divide the interval into two cleaner, sandstone-rich (reservoir) zones and two sandstone-poor (non-reservoir zones; Figure 5). The non-reservoir, sandstone-poor intervals are wavy-laminated sandstone facies but are referred to as non-reservoir, sandstone-poor intervals due to their higher mudrock content as compared to the sandstones in the reservoir intervals. The reservoir zones are characterized primarily by lower




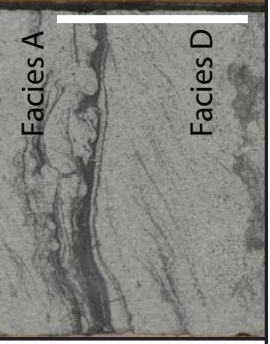
Facies Codes and Facies	Description	Depositional Information	Core Image
<p><b>A - Wavy Laminated Sandstone</b></p>	<p><b>Texture:</b> moderately sorted, upper fine-grained sandstone, siltstone  <b>Structures:</b> Wavy laminations  <b>Average Thickness:</b> 1.90 in. (4.83 cm)  <b>Mudrock Content:</b> 10-70%  <b>Comments:</b> bioturbation likely causing wavy laminations.</p>	<p>Bidirectional currents  Bioturbation  Suspension settling of fine-grained particles</p>	
<p><b>B - Planar Cross-Laminated Sandstone</b></p>	<p><b>Texture:</b> moderate to well sorted, lower fine- to upper fine-grain sandstone, siltstone.  <b>Structures:</b> planar laminations  <b>Average Thickness:</b> 1.42 in. (3.61 cm)  <b>Mudrock Content:</b> 5-15%  <b>Comments:</b> low angle dips present (0-15°)</p>	<p>Unidirectional flow  Unidirectional traction current (upper flow regime)  Rapid deposition in quite water</p>	
<p><b>C - Structureless Sandstone</b></p>	<p><b>Texture:</b> moderately sorted, lower fine- to upper medium grained sandstone.  <b>Structures:</b> none  <b>Average Thickness:</b> 1.38 in. (3.51 cm)  <b>Mudrock Content:</b> 0%  <b>Comments:</b> bioturbation could have homogenized the intervals</p>	<p>Rapid depositions (storm deposit)  Bioturbation</p>	
<p><b>D - Ripple Cross-Laminated Sandstone</b></p>	<p><b>Texture:</b> moderately to well sorted, upper very fine- to lower medium-grained sandstone, mudrock  <b>Structures:</b> unidirectional ripple foresets  <b>Average Thickness:</b> 1.01 in. (2.57 cm)  <b>Mudrock Content:</b> 0-20%  <b>Comments:</b> migration direction unknown, bioturbation disturbs nearly all samples</p>	<p>Unidirectional flow (steady flow)</p>	

Figure 4. Facies codes, facies, and descriptions of the four facies observed in cores and modeled. Scale bars are 1 in (2.54 cm).

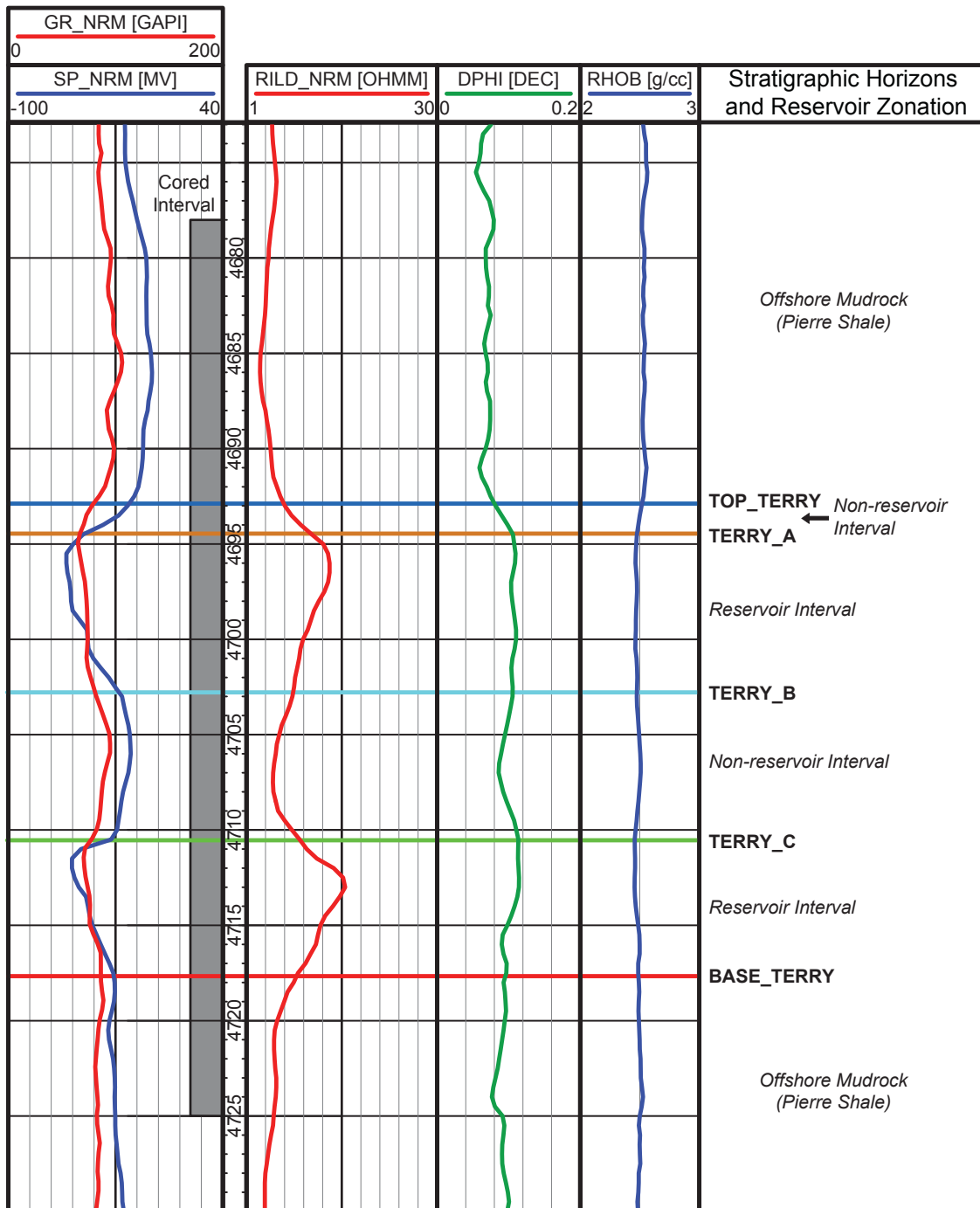


Figure 5. Log suite, reservoir zonation, and cored interval for McHale #1 well (API: 05123076430000) with stratigraphic horizons. Gray bar indicates cored interval. Log response for reservoir intervals includes cleaner GR response, negative SP excursion, and higher porosity. Measured depths in feet. Well location shown in Figure 1.

gamma-ray (GR) values, a negative spontaneous potential (SP) excursion, and slightly higher porosity relative to non-reservoir zones (Figure 5). The non-reservoir sandstone-poor intervals show limited SP response (values near baseline) and relatively higher gamma-ray log values. Deep resistivity (RES-D) shows an increase of several ohm-meters in the reservoir zones and a decreased response in non-reservoir zones (Figure 5). Additionally, relatively higher average porosity (9 to 13%) exists within the sandstone-rich units. However, there are zones within the sandstone-rich intervals that contain relatively lower porosity (7.5 to 9.5%). This could be a result of differential cementation which is observed through microscopes in the cores and documented through core analysis (Larese, 2008).

Across the study area, porosity varies in the reservoir zones, yet shows the same overall trends of higher porosity values compared to non-reservoir zones. Within the reservoir zones, porosity values typically increase upward and have the highest porosities at the top of the reservoir zones (Figure 6). The non-reservoir zones show a smaller amount of pore space than the reservoir zones by several percent depending on location in the study area. A detailed petrographic analysis on a nearby well in Spindle Field (Larese, 2008) indicates that the primary control on reservoir porosity is authigenic clay. Throughout most of the Terry interval, authigenic clay comprises approximately 23% of the total cored volume and is a major pore-filling component. Additionally, a secondary control on porosity is preburial compaction that reduced original porosity by as much as 53% during the time of deposition (Larese, 2008). While this compaction and loss of porosity is significant, authigenic clays found in the pore network reduced porosity and reservoir quality even more (Larese, 2008).

### **Fine-Scale Facies and Permeability Modeling and Upscaling**

Because there is commonly a disparity between the sample volume (sample support) of permeability measurements (e.g., volume of a core plug or probe-permeameter measurement) and the desired scale of analysis and mapping (e.g., volume of a 3-D reservoir



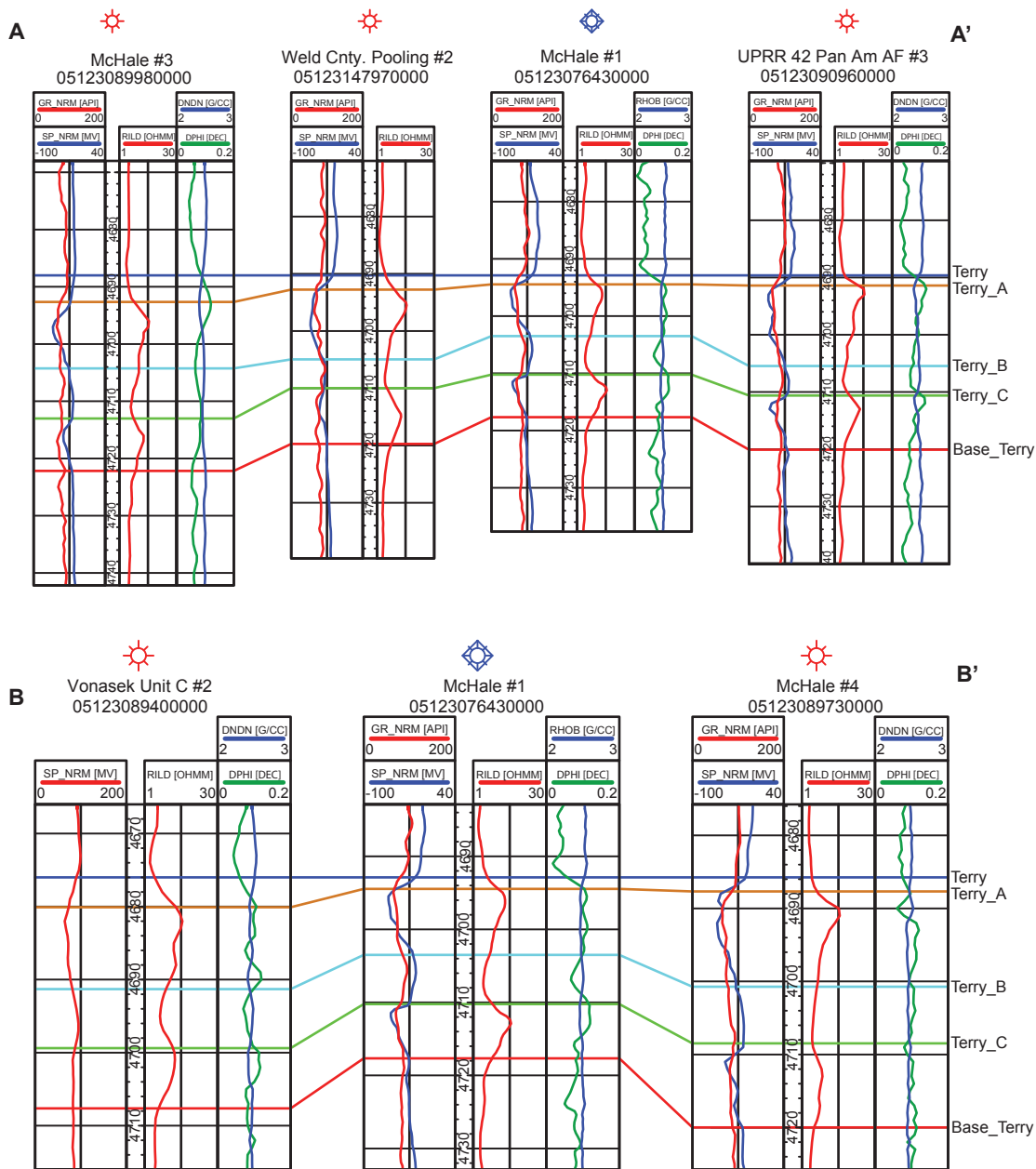


Figure 6. Stratigraphic cross-sections flattened on the top of the Terry Formation showing log suites through the model area. Reservoir intervals are shown with negative SP excursions, higher resistivity, and higher porosity compared to non-reservoir zones. No horizontal scale; distance between wells is uniform. Measured depths are in feet. Locations are shown in Figure 2.

model cell), it is necessary to upscale permeability data. If the reservoir stratigraphy exists as simple layers of uniform permeability, averaging techniques can be applied for upscaling. However, most reservoirs exhibit relatively complex, fine-scale permeability heterogeneity associated with variations in lithofacies and sedimentary structures. To integrate the fine-scale permeability heterogeneity into the upscaling process, numerical, fine-scale 3-D core models (individual cells on the scale of  $\text{in}^3$  [ $\text{mm}^3$ ]), were created for the Terry and Hygiene formations. The fine-scale 3-D core models were then used to generate effective-permeability values by lithofacies using flow-based upscaling. To create 3-D core models, known as near-wellbore models (NWM), a fine-scale surface-based stochastic modeling software was used that models the core at the lamina scale (Wen et al., 1998). Whereas sedimentary process-based modeling methods simulate the fundamental physics of grain transport and deposition, the modeling method used herein produces a geometrical arrangement of sedimentary lamina sets (bedding) by migrating a set of lamina/bedding surfaces so that the resulting fine-scale model framework mimics observed geometries of sedimentary structures (Wen et al., 1998; Ringrose et al., 2005). This type of lamina-scale modeling is an expansion of the work conducted by Ruben (1987) on 3-D synthetic bedform modeling. A near-wellbore model is defined as a “numerical representation of the sedimentological components and petrophysical properties in a rectangular shaped volume along the wellbore” (Nordahl et al., 2005; pg. 18). The near-wellbore modeling process has been shown to have advantages over other statistical methods that are focused on simpler systems (Desbarats, 1987, Deutsch, 1989, Ringrose et al., 2005). These statistical methods are outlined briefly in Ringrose et al. (2005), and a more in-depth review is provided by Renard and Marsily (1997).

Based on detailed core descriptions of sedimentary structures and lithofacies, near-wellbore models were generated for cores of the Terry and Hygiene formations from the McHale #1 and Champlin 369 wells, respectively. The model dimensions are 4 x 4 x 324.48 (10.1 x 10.1 x 824.2 cm; X-, Y-, and Z-directions) for the McHale #1 model (Terry Formation) and 4 x 4

x 564 in (10.1 x 10.1 x 1432.6 cm) for the Champlin 369 model (Hygiene Formation). The models have 40 cells in the X- and Y-directions resulting in lateral cell dimensions of 0.1 x 0.1 in (2.5 x 2.5 mm). Vertically, cell thickness is variable (commonly at the millimeter scale) to represent the curved shapes of cross-stratification and other sedimentary structures. Cell thickness ranges from 0.01 to 1 in (0.25 to 25.4 mm). Given the cell dimensions and length of the cores, 25,988,800 and 21,899,200 cells are present in the McHale #1 and Champlin 369 near-wellbore models, respectively.

As previously discussed, four lithofacies, A) wavy-laminated sandstone, B) planar cross-laminated sandstone, C) structureless sandstone, and D) ripple cross-laminated sandstone were interpreted in cores of the Terry and Hygiene formations. The various facies successions that were observed in the cores were reproduced in the near-wellbore models to create numerical representations of the core (Figure 4). Detailed generic models (referred to herein as submodels) of each of the four facies were generated and used as the basis to construct the numerical facies successions (Appendix A; Figure 7).

To build the 3-D core models, core photographs are cropped and loaded into the modeling software. Each image is depth registered and displayed along with well-log data at the correct depth. The core photographs are then used in conjunction with the core descriptions and actual core to determine what facies is present at what depth. The core photographs allowed for the very detailed placing of facies boundaries and for the fine-tuning of the characteristics for each facies. Each time a facies is seen in the core there are slight changes in the physical properties observed and they must be accounted for. These variations most often consist of changes in the amount of mudrock present, bedding dip angles, and ripple amplitude. All of these variables are controllable and each is manipulated such that the final output of the model matches the actual core observations. Each facies is generated in the modeling software by simulating the processes behind each facies including things like bedform migration, deposition,

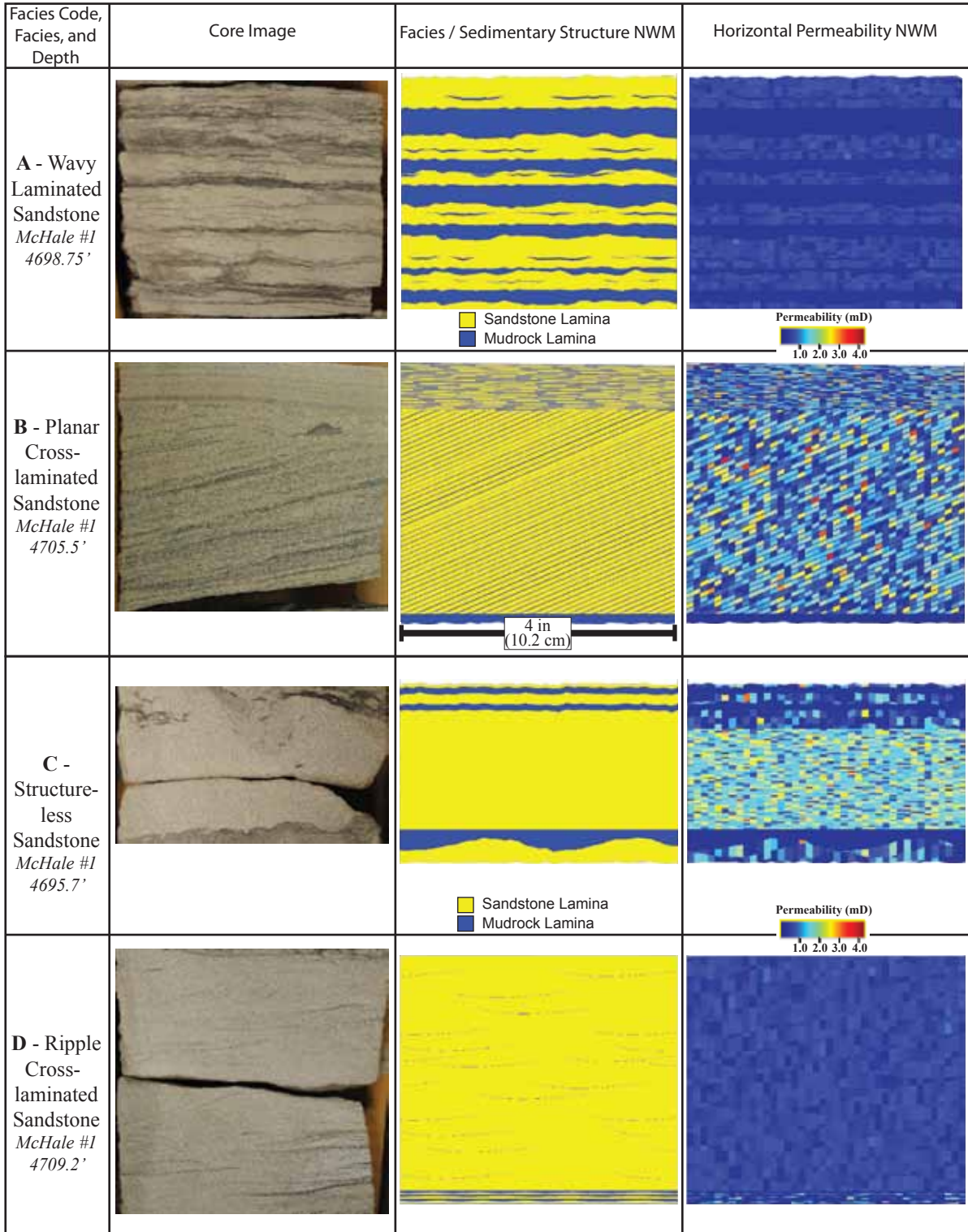


Figure 7. Comparison of facies, near-wellbore models (NWM) of facies, and horizontal permeability. All NWM's and images are 4 in (10.2 cm) wide.

and erosion (SBED Manual). These models are referred to as process-oriented models (Elfenbein et al., 2005).

Following the modeling of the sedimentary structures, the near-wellbore facies models were populated with permeabilities (discussed below). Horizontal permeability values (N=1539; ~500 measurements per core) were measured using a probe-permeameter on the faces of four cores, and the average permeability (geometric mean) and standard deviation were calculated for each facies (Table 1; Appendix B). Because 1-in- (2.54-cm-) diameter core plugs are larger than the thickness of many of the lamina, and measurements could not be directly obtained on the core perpendicular to bedding, vertical permeability measurements were not acquired. Four cores were used to generate a statistically relevant number of permeability values for each facies. The probe-permeameter (TEMCO Mini-Probe Permeameter-410) used in this study calculates permeability by flowing nitrogen gas through a sample. Using the inner and outer tip diameters, flow rate, flow pressure, and ambient pressure, a modified Darcy's equation is used to calculate the permeability of a sample (Appendix B, Goggin et al., 1988). However, this permeability was found to be inaccurate when compared to known permeability values on similar rock types. To correct for this, an empirical calibration was generated by comparing nitrogen flow rates through the permeameter to the known permeability values and using relationship as the equation for calculating permeability. The known standards consisted of 5 core plugs with specific points marked indicating the location of known permeability values (Appendix B).

The number of core permeability measurements was dependent on the frequency of occurrence, and degree of petrophysical change, for each facies (Appendix B). For each facies, the permeability of sandstone and mudrock lamina was measured separately. The tip of the probe-permeameter has an inner diameter of 0.125 in (3.175 mm), which allows lamina larger than this diameter to be measured. In most cases, each target lamina was measured at least three times at different locations across the core face. This was not always possible as some

Facies	Original Horizontal Permeability			Effective Horizontal Permeability		
	N	Sandstone Lamina Avg. (mD)	Sandstone Lamina Std. Dev. (mD)	N	Effective K Avg.	Effective K Std. Dev. (mD)
<b>A</b>	47	0.332	0.532	32	0.098	0.050
<b>B</b>	73	0.660	0.500	22	0.256	0.071
<b>C</b>	7	0.155	0.187	7	0.081	0.006
<b>D</b>	13	1.561	0.580	16	1.466	0.002

Table 1. Permeability statistics for original and effective permeabilities by facies in the McHale #1 core. Original-permeability values are divided by facies and lamina type. Effective-permeability values are derived from near-wellbore models and are representative of the entire facies regardless of lamina type. Original-permeability mudrock values are assumed to be 0.004 mD.

lamina were discontinuous or varied in thickness laterally. Measurements were not acquired near the core's edges due to the decreasing core thickness at the edge. The thickness of the sample must be at least five times the inner radius of the measurement tip in order to use the modified Darcy's equation to calculate the permeability (Instrument manual for mini-permeameter Model MP-401). While the modified Darcy's equation was not used for the final output of permeability numbers, this guideline was still followed to ensure the gas flow rates through the sample were not being affected by insufficient core thickness. For this research, the minimum core thickness based on the tip size is 0.3125 in (0.79 cm). However, to ensure that the permeability data being acquired was not affected by gas leaking through the base of the core, a minimum core thickness of 0.5 in (1.25 cm) was used. Furthermore, to obtain more accurate measurements, the calculated permeability indicated by the permeameter could not vary by more than 10% for a minimum of 25 seconds. It was difficult to measure permeability for the mudrock lamina because of the lower permeability of the mudrock, sensitivity of the probe-permeameter, and condition of the mudrock intervals in the core (e.g., microfractures, parting on bedding planes, physical alteration due to exposure and handling, etc.). Therefore, a constant value of 0.004 mD was assumed for mudrock. The limited permeability data that were obtained suggest that the mudrock lamina act as baffles or barriers to fluid flow; however, not enough data was obtained to define an accurate permeability value for the mudrock lamina.

The permeability measurements were sorted by facies and lamina type and average permeability and standard deviation were calculated for each facies (Table 1). Each facies was built with its own sandstone and mudrock lamina, which allows for each facies to be assigned permeability values separately. Each facies is assigned a permeability average and standard deviation and the model is populated using these values (Figure 7; Table 1; Appendix C). Each time a facies occurs in the near-wellbore model (NWM), it is populated with permeability values between the minimum and maximum permeability values measured for that facies (Appendix A) and in such a way that after every cell was modeled in that facies. The average and standard

deviation for that of the generic facies match what was originally measured. There are options for variograms and correlations to porosity but due to the nature in which the permeabilities were collected a variogram could not be calculated. Additionally the correlation to porosity values was not possible as the only porosity data available was from well logs and the scale difference between the point measurement and well log is too great (Appendix C).

The fine-scale, near-wellbore permeability models of the Terry and Hygiene formations were upscaled to obtain effective-permeability values by facies. The upscaling procedure used in this study was done by submodel boundary. In this method each facies boundary is used as a defining boundary and an effective permeability is generated for each facies occurrence. To generate the effective permeability, a single-phase, flow-based upscaling algorithm is used. While several options for flow-based upscaling exist, upscaling by periodic boundary conditions was used. Previous work conducted on heterogeneous facies indicates that a periodic boundary condition upscaling method is appropriate for this study (Durlafsky, 1991; Pickup et al., 1994). This type of flow-based simulation imposes a head gradient in three directions and using this, calculates effective permeability by facies. The simulation does not impose any zero-flow boundaries around the model and has pressure gradients equal on the surfaces in the XY and XZ planes (Appendix C). The upscaled permeability values are generated in three directions, one for each direction of simulated flow, but for the purposes of this study, only the values in x-direction are used for the comparison of measured- and effective-permeability (Table 1). Typically, an average of permeabilities generated during the upscaling ( $k_x$  and  $k_y$ ) would be used to create a permeability value for the horizontal plane ( $k_h$ ); however, after a qualitative comparison of the permeability values in both directions, the difference between  $k_x$  and  $k_y$  obtain herein was negligible throughout the entire stratigraphic interval (difference < 0.15 mD). This difference led to only  $k_x$  values being used. The differences between measured- and effective-permeability values are shown in Figure 8. Upscaling results for the McHale #1 and Champlin 369 near-wellbore models shows that the effective-permeability data ranges are narrower and



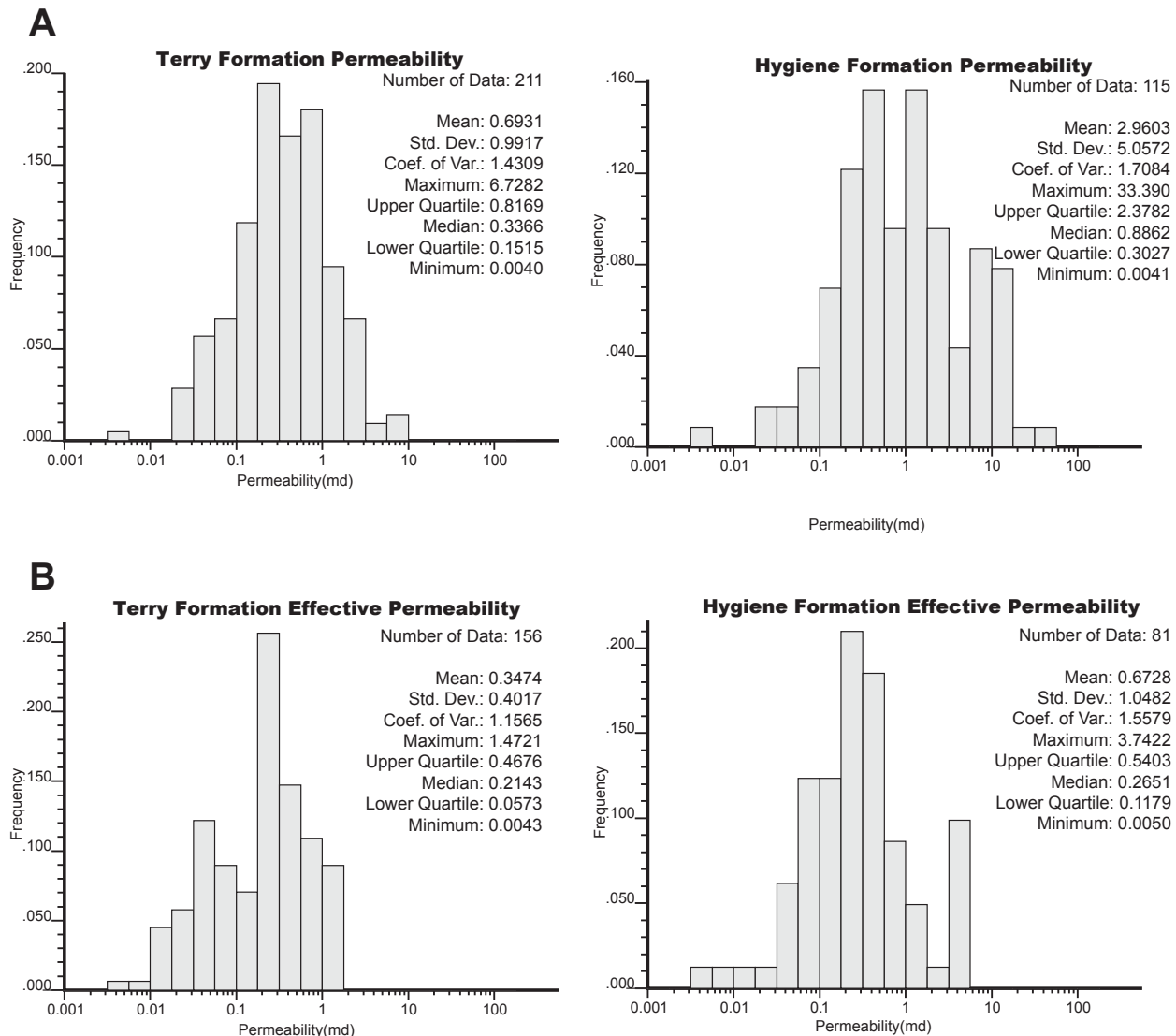


Figure 8. Histograms of A) original and B) effective permeability for the Terry Formation (McHale #1) core and Hygiene Formation (Champlin 369) core.

average permeabilities for the entire interval are reduced by 49.9% and 77.2%, respectively, as compared to the measured-permeability values.

### **Field-Scale 3-D Facies, Porosity, and Permeability Modeling**

The significance of fine-scale permeability heterogeneity associated with lithofacies that exist below the resolution of reservoir model cells was investigated through comparative analysis of 3-D “field-scale” permeability models and associated permeability connectivity. Three-dimensional facies, porosity, and permeability models of the Terry Formation were generated for a 0.28 mi<sup>2</sup> (0.73 km<sup>2</sup>) model area within Spindle Field (Figure 2, Appendix D). The interpreted lithofacies were modeled first and then porosity was modeled using the resulting lithofacies models as a constraint. Measured and upscaled permeability were modeled separately using both lithofacies and porosity models as constraints. The model area contains nine wells with the McHale #1 cored well at the center (Figure 2). All but one well contains gamma-ray (GR), spontaneous potential (SP), deep resistivity (RES), and density porosity (DPHI) logs; all of which were used in the modeling process. The logs were normalized to the Terry Formation interval in the cored McHale #1 well using a scaling algorithm which scales the maximum and minimum values of the Terry Formation interval of each well to the corresponding values in the McHale #1 well. This was done to limit the effect of multiple logging tools used over a 25-year period. Due to a lack of neutron-porosity logs, only density porosity logs were used. The 3-D model dimensions are 2828 x 2900 x 40 ft (length, width, thickness; 826 x 887 x 12.2 m; Figures 2 and 9). Four vertical model zones were created and correspond to the reservoir and non-reservoir zones previously defined. The zones are based on the core-derived facies, gamma-ray, and spontaneous-potential log responses. Individual cells are 29.8 x 30 ft (9.08 x 9.1 m) in area and proportional layers (N=46) were used resulting in 423,890 model cells (average cell/layer thickness is approximately 1 ft [0.3 m]) (Figure 9).

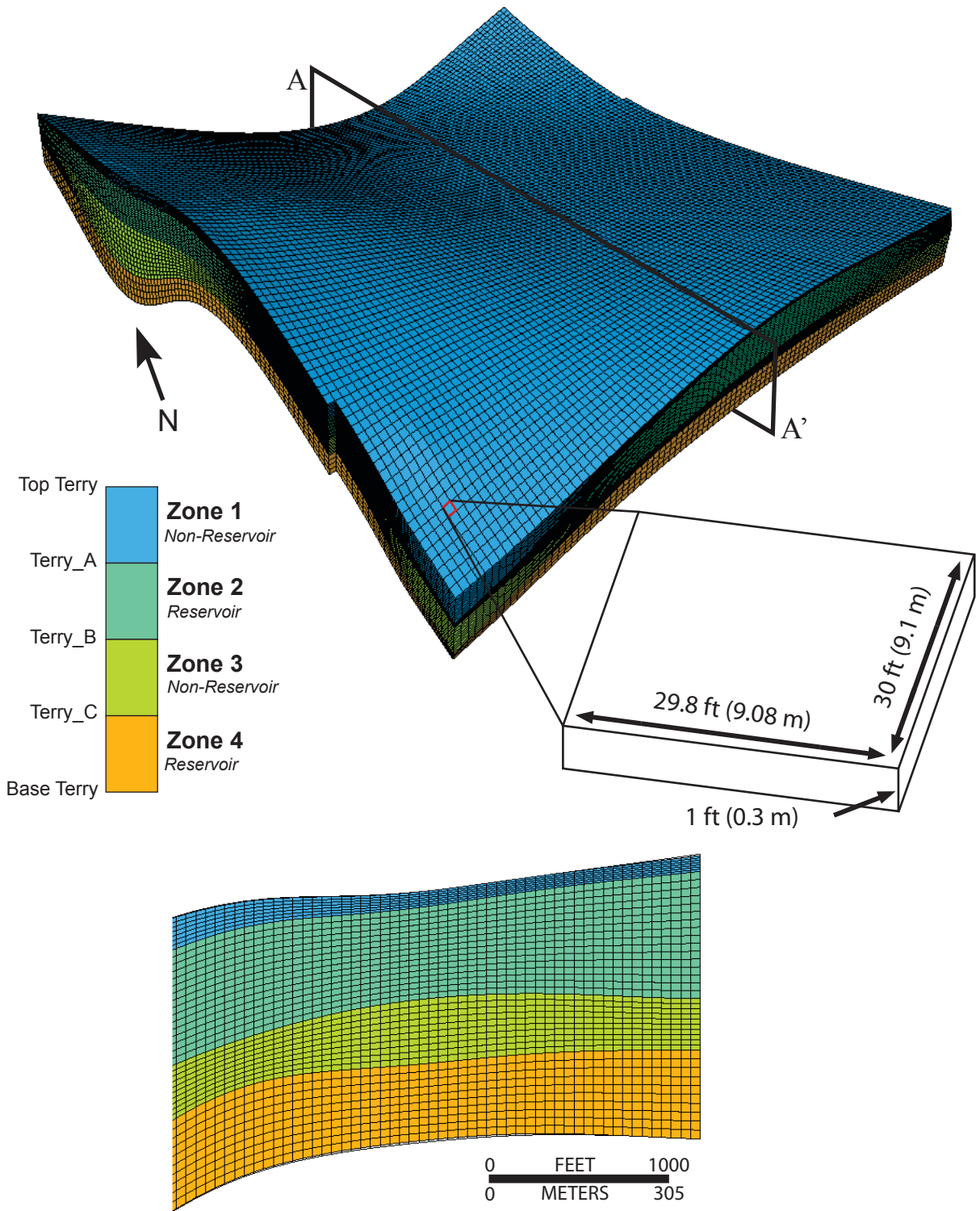


Figure 9. Top: Reservoir model zones and dimensions of a single model cell are shown. Proportional layers (N=46) were used resulting in 423,890 model cells (average cell/layer thickness 1 ft (0.3 m). VE=10x. Bottom: Cross-section A-A' through reservoir model showing reservoir zones (shading) and cells. VE=30x.

Field-scale facies models were generated to map the distribution of the four main lithofacies within this portion of Spindle Field. The 3-D facies NWM's are constrained to the McHale #1 cored well at the center of the model area and lithofacies percentages based on that cored well. Because distinct relationships do not exist between the lithofacies present in core and the associated well-log responses, facies logs could not be estimated in non-cored wells. However, a general relationship does exist between SP response and lithology (sandstone vs. mudrock). The SP logs exhibit negative SP excursions corresponding to more sandstone-rich facies (structureless, ripple cross-laminated, and planar cross-laminated sandstones), whereas the more mudstone-prone facies, wavy-laminated sandstone, approximately corresponds to near-zero SP values within the Terry Formation. Therefore, to further constrain the facies models, a lithology probability volume was generated based on the SP logs and used as a constraint on lithofacies distribution during the modeling process. A 3-D SP model was first generated using the SP logs and sequential-Gaussian simulation (SGS) (Figure 10). The vertical variograms were defined for each zone using the SP logs (Appendix D). Spherical variogram models were used with vertical correlation lengths (ranges) between 1 and 4.8 ft (0.3 and 1.52 m). For the horizontal direction, variograms were modeled using spherical functions and both major- and minor-direction ranges were arbitrarily set to 1000 ft (305 m) or approximately one-quarter the diagonal distance across the model domain. The SP model was converted to a lithology probability volume (model) by non-linear rescaling of the SP model such that 0 and 1.0 correspond to the most positive (mudrock-prone) and negative (sandstone-rich) SP values, respectively (Figure 10). The lithology probability volume (model) was also used as a constraint on the sandstone-rich and mudrock-prone lithofacies during the facies modeling process.

Thirty realizations of the facies models were generated using sequential-indicator simulation (SIS). The vertical variograms were defined for each zone using the facies log from the McHale #1 well (Appendix D). Spherical variogram models were used with correlation

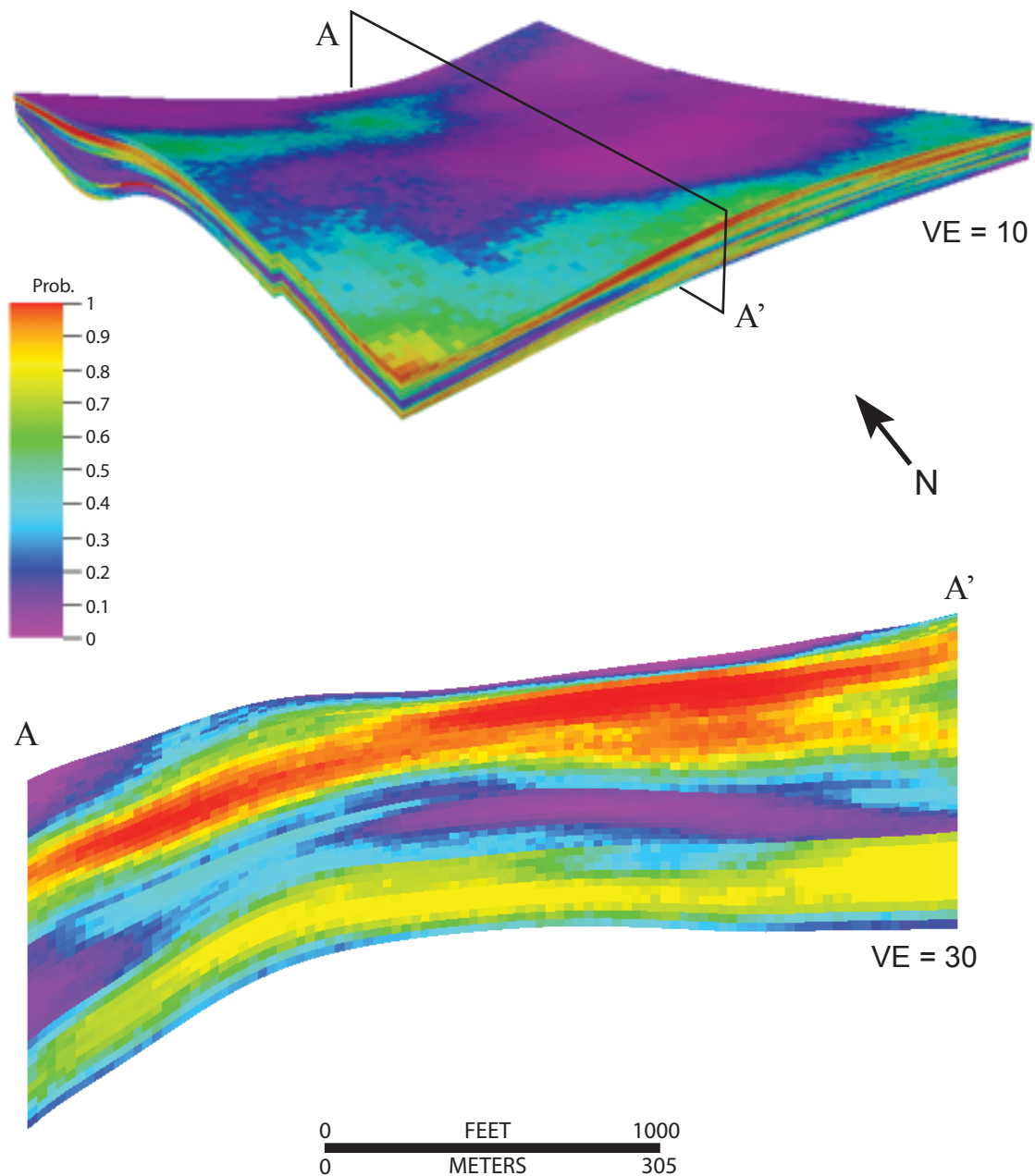


Figure 10. Top: Lithology probability volume (model) used to constrain facies distribution. Higher values indicate a higher probability of sandstone-rich facies. The probability volume is based on the SP response in which negative SP excursions correspond to more sandstone-rich facies and near-zero SP values correspond to more mudstone-prone facies. Bottom: Cross-section through the 3-D lithology probability volume model.

lengths between 1.1 and 8.3 ft (0.34 and 2.53 m). For the horizontal direction, variograms were set using spherical models and ranges were assumed for major- and minor-directions and arbitrarily set to 1000 ft (305 m). The nugget was set to zero for facies modeling. For subsequent modeling and analysis, an average facies model based on the 30 realizations was computed (referred to herein as average facies model, AFM (Figure 11)). The AFM was generated from the thirty facies realizations such that the most common facies to occur in a given cell of the thirty realizations was assigned to that cell in the AFM. The AFM exhibits a smooth facies distribution, relative to a single facies realization, and the AFM is similar to a facies model generated using indicator kriging (Figure 11). This smoother distribution is likely to be more realistic than the more discontinuous single realization model. This was determined based on limited outcrop observations and the interpreted depositional environment (Appendix D).

Porosity models were generated based on normalized density-porosity (DPHI) logs from the nine wells in the model area. Neutron-porosity logs were limited to select wells in the model area and thus were not used in this study. Thirty realizations of the porosity model were generated using sequential-Gaussian simulation constrained to variograms, porosity statistics derived from the DPHI logs, and the AFM (Figure 12). Vertical variograms were defined for each zone and each facies using the normalized DPHI log in the McHale #1 well (Appendix D). This particular log was chosen because of the quality of the log data. Spherical variogram models were used with correlation lengths between 0.6 and 7.3 ft (0.18 and 2.23 m). For the horizontal direction, variograms were set using spherical models with ranges for major- and minor-directions assumed to be and arbitrarily set to 250 ft (76.2 m). The nugget was set to zero for porosity modeling. An average porosity model based on the 30 realizations was computed (referred to herein as average porosity model or APM; Figure 12). The APM was generated using an arithmetic average where, for a given cell, the corresponding porosity values of the thirty realizations were averaged to generate the porosity value in the APM. The

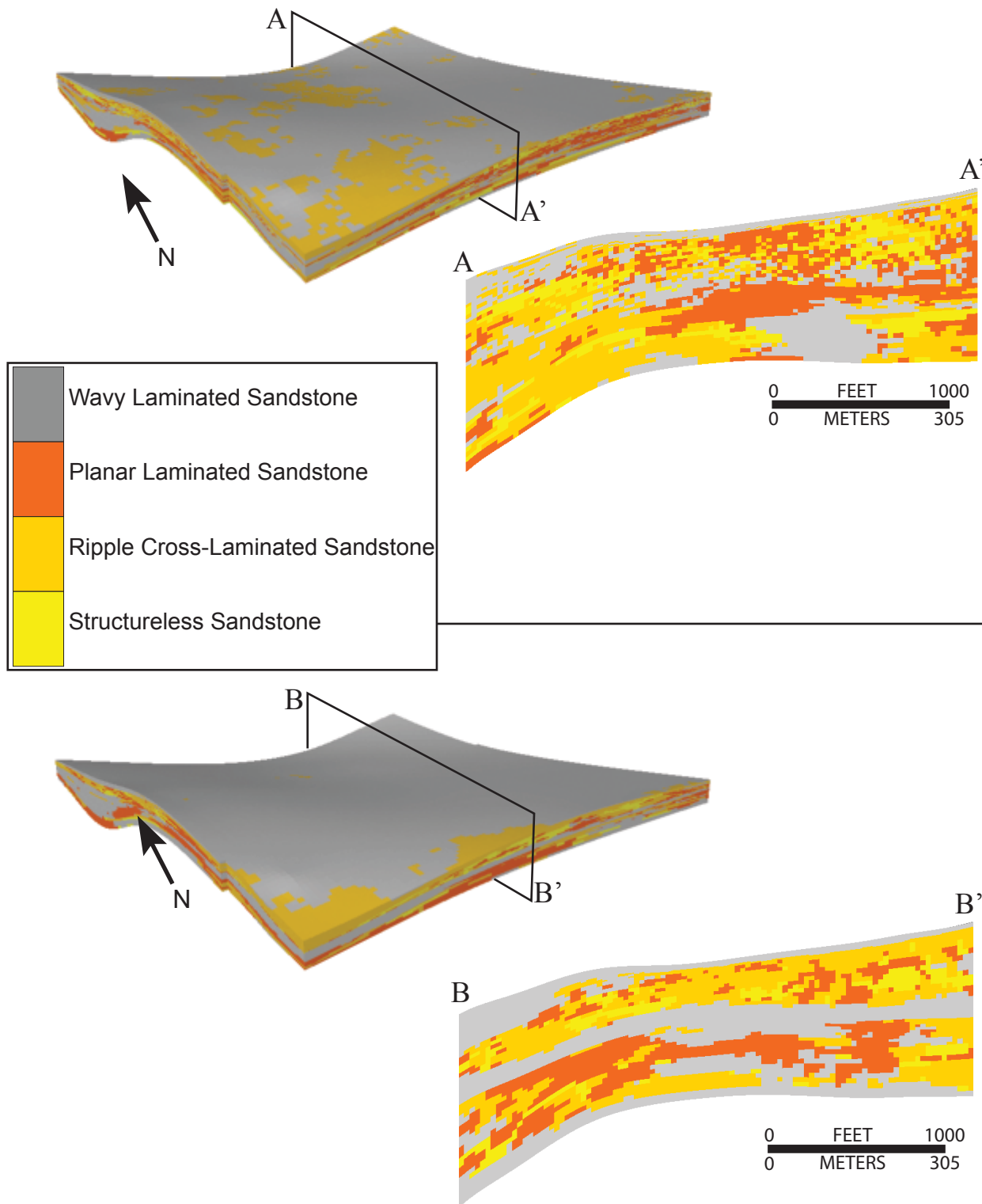


Figure 11. Top: Single facies realization of the lithology probability volume showing a discontinuous distribution of the facies. Bottom: Averaged facies model from 30 realizations (AFM) which shows a more continuous and presumably geologically reasonable distribution of facies as compared to one realization. 3-D models: VE=10; cross-sections: VE=30.

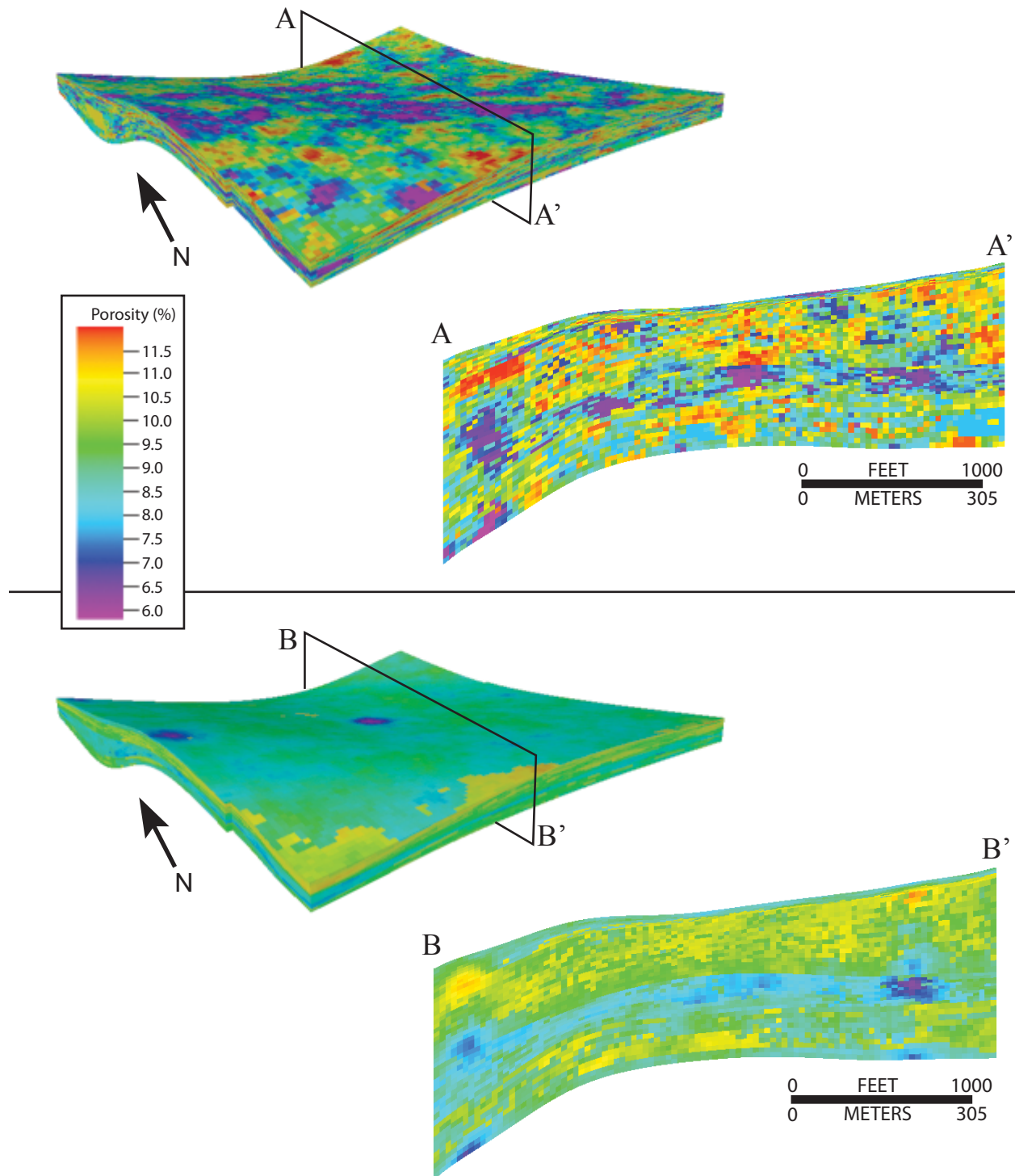


Figure 12. Top: Single porosity realization showing an increasingly discontinuous porosity distribution. Bottom: Average of thirty porosity realizations which shows a more continuous distribution. Porosity models:  $VE=10x$ ; cross-sectional views  $VE=30x$ .



APM, like the average facies model, exhibits a smooth distribution of porosity values as compared to a single porosity realization.

Field-scale models were generated to map the distribution of both measured and effective permeability in this portion of Spindle Field (Figure 13). Thirty permeability realizations were generated using sequential-Gaussian simulation constrained to variograms, permeability statistics derived from the McHale #1 core and near-wellbore model, the APM, and a bivariate transformation (cloud transformation) between porosity and permeability (Appendix D). Low coefficients of determination ( $R^2$  values) associated with linear regressions between porosity and both measured and effective permeability dictated the need for use of a cloud transformation (Sloan, 2012). For the bivariate transformation, a porosity and permeability cross plot was created for both types of permeability. For each cross plot, the porosity scale is divided into ten porosity bins. For a given porosity value within a porosity bin, a range of permeability values is possible because of the low coefficient of determination (data scatter or data cloud). To estimate the permeability values for a model cell, the associated porosity for that cell from the porosity model is considered. The permeability values (from the porosity-permeability cross plot) that fall within the associated porosity bin are used to define (simulate) the permeability value that is assigned to the model cell.

As expected, because the input measured and upscaled (effective) permeability values are honored in the modeling process, the measured-permeability models show higher average permeability values (0.52 mD and 0.53 mD for the single and average models, respectively) than the effective-permeability models (0.14 mD and 0.12 mD for the single and average models, respectively). However, the spatial trends of the permeability distributions within the models are similar between the two types of permeability models.

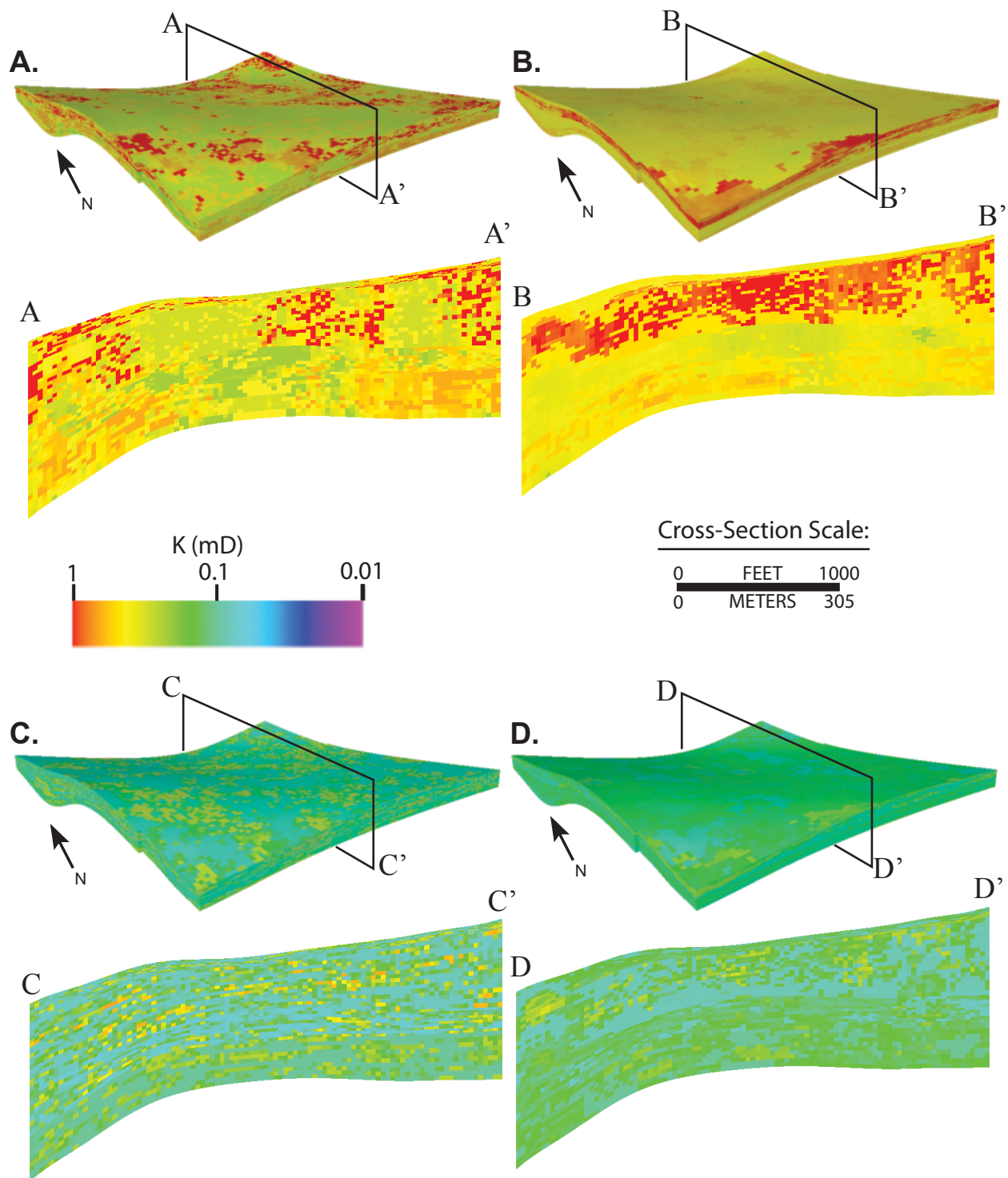


Figure 13. Permeability models using original and effective permeabilities. Models A and B are original (non-upscaled) permeability models. Models C and D are effective (upscaled) permeability models. Models A and C represent a single permeability realization, models B and D represent an average of 30 permeability realizations. 3-D models:  $VE=10$ ; cross-sections:  $VE=30$ . Effective-permeability models show lower permeability values compared to original-permeability models. Average models show smoother distributions compared to a single realization.

## Static Connectivity

Static connectivity is defined and used in this study as the volume sum of reservoir cells connected to a particular pattern of wells (directly or indirectly) divided by the total volume of reservoir cells in the 3-D model and is expressed as a percentage. The static connectivity analysis in this study is primarily a function of permeability and is used to compare the differences in connected volumes between models based on measured- and effective permeability. For each model type, static connectivity was determined using a smaller model area than the field-scale model to avoid edge-effects potentially created during the modeling process (Figure 2). To determine static connectivity, pseudo-wells were used on a 5-ac (2-hectare) spacing (Figure 2). Each model cell was classified as either reservoir or non-reservoir based on a porosity cutoff (reservoir > 8.75%, non-reservoir < 8.75%) and a variable permeability cut-off. The porosity cutoff for this analysis was determined based on the porosity histogram from the porosity models (Appendix D). The value was determined so that approximately one third of all the porosity values fall below the cutoff value. The porosity cutoff value is below the average porosity value for the entire model (9.8%), and is greater than that of the average porosity value in the non-reservoir zones (5.1% and 8.4% for both non-reservoir zones). Having this value greater than non-reservoir zones but less than the overall average porosity, helps ensure that the facies in the previously identified non-reservoir intervals are not included in static connectivity analysis. All of the facies in these zones are not removed as a whole from the static connectivity analysis because it is possible that there are some minor producing facies within these zones and therefore the entire intervals cannot be excluded.

For the permeability portion of the reservoir cell definition, the permeability cut-off was varied by increments of 0.15 mD starting from 0.0 and going to 1.95 mD. This was done to determine how the static connectivity varied among all the models with multiple reservoir permeability definitions. For the permeability models that are constrained to the single porosity model, the connected volume 62.5% for the 0.0 mD cutoffs on both the measured- and

effective-permeability models (Table 2). As the permeability reservoir definition was increased to the maximum cutoff of 1.95 mD, the connected percentage decreased to 0% for both model types. As the permeability cutoff increases from 0.0 mD, the differences in connectivity for the two permeability models become evident (Figure 14). For effective-permeability values, static connectivity drops dramatically (42.6%) after the first 0.15 mD increase (42.6% to 18.9%). As the permeability cutoff increases, static connectivity reaches 0% at 0.75 mD. In contrast, the measured-permeability models show a different connectivity decay. The percentage of connected cells stays nearly the same through a permeability cutoff of 0.30 mD with only minor changes (varies by < 5%). There is no dramatic decrease like the one seen in the effective-permeability models at the lowest permeability reservoir definitions. Subsequently, there is a significant decrease in connectivity to 4.48% at the permeability cutoff of 0.75 mD, after which the connected cell percentage decreases at a slower and more consistent rate. For this permeability type model, the connected percentage reaches 0% at a reservoir permeability definition of 1.95 mD. Figure 15 shows how the connected volumes appear in cross-section at three strategic permeability cutoffs.

The permeability models constrained to the average porosity model behave in a slightly different way. For the effective-permeability model, connectivity decreases almost immediately and the measured values remain constant before decreasing at a similar rate (Table 2). Both models started with 79.6% static connectivity at the 0.0 mD cutoff. Like the effective-permeability model that is constrained to the single porosity realization, the effective-permeability values constrained to the average porosity model decrease immediately and reach 0% connectivity at the 0.75 mD cutoff. The measured values also show a similar decay pattern to the permeability models that are constrained to the single porosity realization after the 0.15 mD cutoff is reached. The model reaches 0% connectivity when the permeability cutoff value reaches 1.8 mD (Figure 14).

Reservoir K (mD)	Original Permeabilities		Effective Permeabilities	
	Connectivity		Connectivity	
	(Single $\Phi$ Model)	(Avg. $\Phi$ Model)	(Single $\Phi$ Model)	(Avg. $\Phi$ Model)
<b>0.00</b>	62.49%	79.55%	62.49%	79.55%
<b>0.15</b>	62.49%	79.55%	18.89%	11.39%
<b>0.30</b>	57.19%	58.70%	4.98%	0.16%
<b>0.45</b>	33.73%	32.90%	0.05%	0.02%
<b>0.60</b>	8.46%	15.79%	0.01%	0.01%
<b>0.75</b>	4.48%	8.81%	0.00%	0.00%
<b>0.90</b>	4.06%	8.11%	0.00%	0.00%
<b>1.05</b>	3.20%	7.23%	0.00%	0.00%
<b>1.20</b>	2.15%	5.95%	0.00%	0.00%
<b>1.35</b>	1.40%	5.39%	0.00%	0.00%
<b>1.50</b>	0.57%	4.88%	0.00%	0.00%
<b>1.65</b>	0.03%	4.23%	0.00%	0.00%
<b>1.80</b>	0.00%	1.39%	0.00%	0.00%
<b>1.95</b>	0.00%	0.00%	0.00%	0.00%

Table 2. Static connectivity percentages for each of the four permeability models given a reservoir porosity cutoff of 8.75% and a variable permeability definition for a reservoir cell.

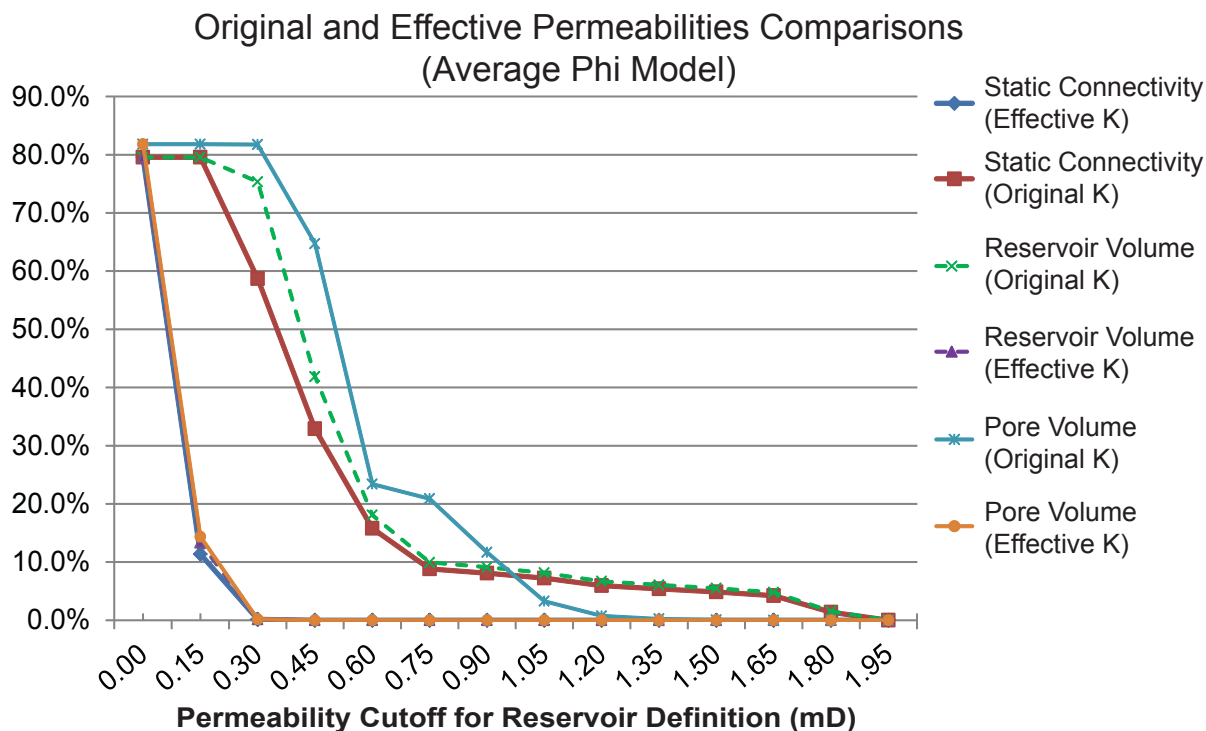
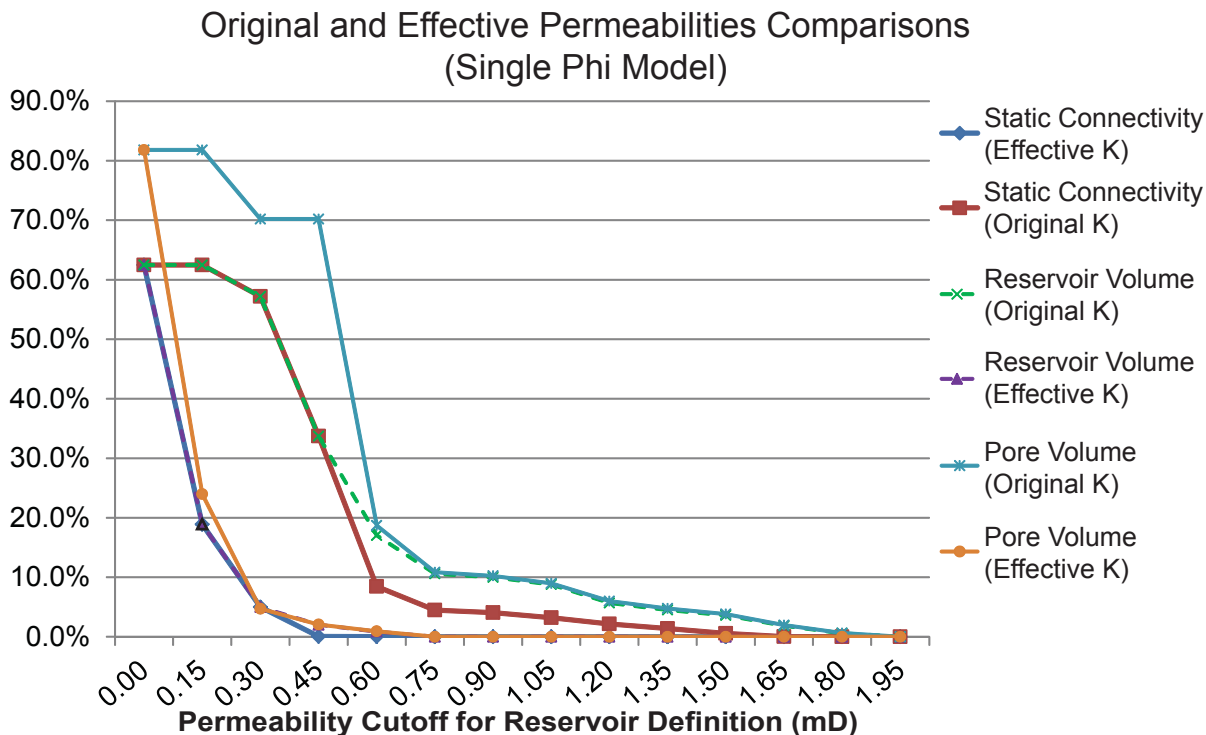


Figure 14. Graphs showing static connectivity, reservoir volume (as percentage of bulk reservoir volume), and pore volume percentage at varying permeability cutoffs. Static connectivity determines illustrates how much of the reservoir is connected. Reservoir volume illustrates how much total reservoir volume there at a cutoff. Pore volume illustrates the amount of pore space of cells that meet a reservoir criteria at a given reservoir definition.

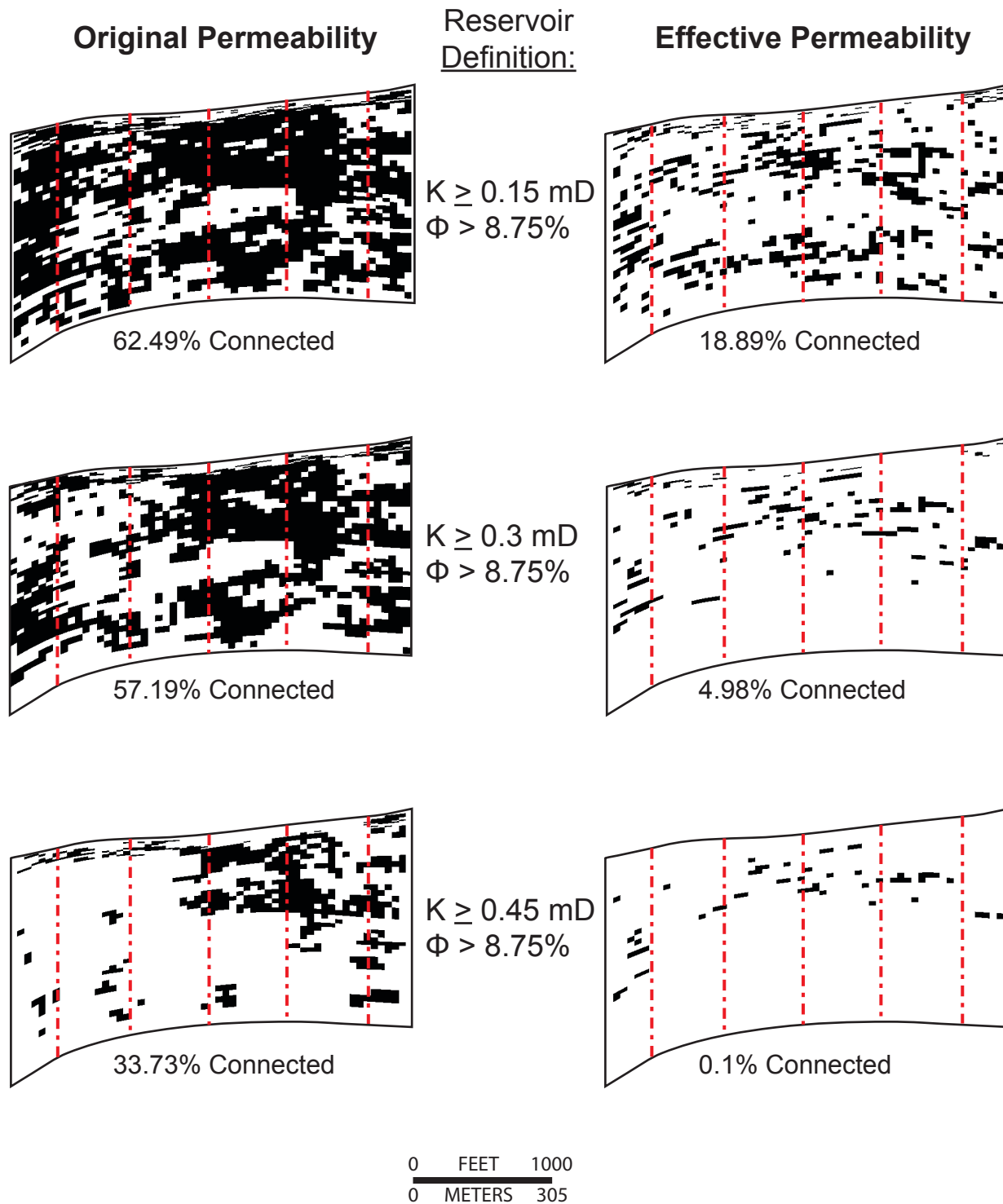


Figure 15. Static connectivity comparison in cross-sectional view (cross-sectional plane: I=54) of single porosity referenced original- and effective-permeability models. This view shows cells in the plane that are connected to a wellbore. Cross-sectional plane is shown in Figure 13 and is consistent with all model cross-sections. Red lines indicate wellbores. VE = 30x

Other comparisons of the permeability models include a comparison of bulk reservoir volume and pore volume of the model at given reservoir definitions (Figure 14). Bulk reservoir volume is used in this study as the total volume of all cells in the model that meet the criteria of a reservoir cell at a given permeability and porosity cutoff and is displayed as percentage of bulk model volume. As with static connectivity, bulk reservoir volumes were determined using a porosity cutoff of >8.75% and a variable permeability cutoff. This is useful to compare how much of total reservoir volume in the model area is being utilized in the static connectivity measurements (Figure 14; Appendix E). The bulk reservoir volume data indicates that the static connectivities at lower permeability values for all model types utilize all of the available reservoir cells. However as the permeability cutoff values are increased, the differences between the bulk reservoir volume and the volume of cells connected becomes more apparent before reaching 0% much like static connectivities (Figure 15). The overall trend of the curve for reservoir volumes follows the same trend as static connectivity. This similar trend is likely due to the 5-acre (2-hectare) spacing which causes nearly all reservoir volumes to be connected to a wellbore. Similar to the other two comparison methods, pore volume for a given reservoir definition shows the same curve shape. Pore volume is displayed as a percentage of total model pore volume given no restrictions on porosity or permeability. As a porosity limit of >8.75% was added and the 0.15mD permeability step was increased, the pore volume decreased at a similar rate to the decline rates of static connectivity and bulk reservoir volume (Figure 14). The decrease shows almost the exact same decrease for the effective-permeability models but has more variability in the measured-permeability based models. The difference is likely caused by the measured-permeability models having higher permeability values and wider range.



## Discussion

### ***Facies and Depositional Environment***

Based on core descriptions, observed facies, and well-log analysis, the interpreted depositional environment for the Terry Formation in the study area is an offshore-bar complex (Porter, 1976; Kiteley, 1977; Pittman, 1988, 1989; Al-Raisi et al., 1996). This interpretation, as previously stated, is one of several possible hypotheses. Four reservoir zones are also interpreted in the Terry Formation based on these data that represent either interbar or sand-bar facies associations. The interbar facies association includes sandstone-poor wavy-laminated facies which was deposited in a quiet-water setting. As the sand bar migrates, an area of quieter water would exist with mud-sized particle deposition being dominant. The sandstones within the bars show a relative upward-coarsening in grain-size which is also characteristic of shelf sandstones (Porter and Weimer, 1982). Glauconite is present in the cores which is a potential indicator of offshore deposition and resonance (Appendix A). Additionally, bioturbation is more prevalent in the wavy-laminated facies indicating a quieter setting in which more organisms lived. The sand-bar facies association includes both ripple- and planar-laminated facies which formed by currents responsible for transporting sediments from a nearby source and depositing them in the area. The structureless sandstone is a more ambiguous as it could have been deposited without any internal structure or it may have been extensively bioturbated making it appear structureless. It is likely that both of these processes occurred.

### ***Permeability Upscaling***

There are different relationships between the measured- and upscaled-permeability values for each facies (Appendix C). For the Terry Formation, the wavy-laminated sandstone facies shows a permeability change from an average measured permeability of 0.332 mD to 0.098 mD for the upscaled (effective) value (Table 1). This represents a 70% decrease and is likely caused by the mudrock lamina (10-70%) within the facies (Figure 4). Due to the near-zero

permeability (0.004 mD) of the mudrock lamina, effective permeability is relatively low. During the upscaling process as flow is simulated through the sample, the mudrock likely acts as a barrier to flow and limits the permeability of the entire facies despite the relatively high permeability of the sandstone lamina (Table 1). This example shows the significance of upscaling permeability data to generate effective permeability values for each facies. A core plug or other small-scale measurement may be acquired in the wavy-laminated sandstone facies and, depending on the sandstone lamina thickness, may indicate that the permeability is an order of magnitude or more higher than the true effective permeability of that sample. Conversely, the structureless sandstone facies is minimally affected by the upscaling process. The structureless sandstone has an average measured permeability of 1.561 mD and, after upscaling, the average effective permeability is 1.466 mD; a 6.1% decrease. The difference between these two values is smaller than that of the mudrock-rich wavy-laminated facies because this facies does not have associated mudrock lamina. Without permeability-inhibiting mudrock lamina, flow through the structureless sandstone facies is not significantly affected during the upscaling process as facies that contain mudrock. It is still important to generate effective-permeability values for this facies because of the decrease in permeability. These facies are abundant in the reservoir and represent a significant rock volume.

Previous upscaling research examines the utility of flow-based upscaling. Refer to Renard and DeMarsily (1997) for a review of details of different types of deterministic and stochastic upscaling techniques. Jackson et al. (2003) discusses the scale differences between core-based measurements (i.e., core plug, probe-permeameter, thin section, etc.) and typical geologic models which are many orders of magnitude greater in terms of volume being analyzed. The conventional process of acquiring small-scale measurements and utilizing them in large-scale modeling does not properly account for heterogeneities that exist at the smaller scale. As reservoir properties are measured at smaller scales (e.g., with unconventional reservoirs), it is important to properly recognize these small-scale heterogeneities and account

for them in reservoir analysis and modeling (Pickup et al., 1994). Facies-based upscaling is one method to address these small-scale heterogeneities and is advantageous as it considers the shape and geometry of bedding structures and calculates their effect on permeability.

### ***Static Connectivity***

For the measured-permeability models, static connectivity is initially 62.5% and 79.6% based on the single and average porosity realizations, respectively (Table 2; Figure 14; Appendix E). Static connectivity for each model remains constant with the initial permeability cutoffs; however, as the permeability cutoff increases, static connectivity decreases significantly and gradually approaches 0% connectivity. This is observed in cross-sectional view through the center of the model area (Figure 15). As the permeability cutoff is increased and approaches the median of the permeability range, sections of the reservoir are no longer connected to wellbores, and the differences between the measured- and effective-permeability models in terms of static connectivity becomes significant. Depending on the type of permeability used, measured or effective, the total volume of reservoir connected at this well spacing is tens of percent different. These differences indicate why it is important to use scale-dependent, facies-based, effective-permeability values for reservoir modeling at the field scale.

## **Conclusions**

The Terry and Hygiene formations in Spindle Field consist of four key lithofacies: 1) wavy-laminated sandstone, 2) planar cross-laminated sandstone, 3) ripple cross-laminated sandstone, and 4) structureless sandstone. The facies are stacked in successions that are characterized as either sandstone-rich or sandstone-poor. The sandstone-poor intervals exhibit alternating patterns of dominantly wavy-laminated sandstone with minor amounts of structureless sandstone and planar cross-laminated sandstone. The sandstone-poor facies associations are interpreted to have formed in an inter-bar setting as part of an offshore-bar

complex. They exhibit relatively low permeability values and are non-reservoir facies. In contrast, the sandstone-rich intervals consist of alternating planar cross-laminated sandstone, ripple cross-laminated sandstone, and structureless sandstone. These deposits are interpreted to represent offshore sand bars. They are considered to be the primary reservoir facies given their relatively higher permeability values.

The results suggest that upscaling permeability data from the scale of individual lamina to a facies scale is an important step in reservoir analysis, proper definition of reservoir-quality rock at the field scale, and mapping of reservoir-quality lithofacies. The estimation and use of facies-based effective properties for reservoir definition and modeling is important as it has a direct impact on the number and type of wells required for reservoir development. The results show that average upscaled permeabilities of each facies are lower by as much as 50% relative to the measured values. The decrease in average permeability varies by facies and only minimally affects the structureless sandstone facies while the greatest effect is observed in the mudstone-rich wavy-laminated facies. Using the measured permeability values from permeametry or core-plug measurements will result in field-scale reservoir maps (models) in which the average permeability values are too high and that exhibit unrealistic distributions of extreme (too high and too low) permeability values. The extreme values of permeability can potentially have a profound effect on fluid-flow simulations and production estimates.

Analysis of the 3-D static connectivity (to producing wells) of reservoir volumes as defined by permeability cutoffs shows that for relatively lower permeability cutoffs, there is a distinct difference in connected volume between measured- and effective permeability models; in some cases, 50% lower connectivity for the effective-permeability model. This is significant because it represents the reservoir volume connected to wells for potential production. Also, for the lower permeability cutoffs, the total volume of potential reservoir rock is essentially the same as the connected volume; all potential reservoir cells are connected to wells. As the permeability cutoff (reservoir definition) increases, static connectivity decreases and the

differences between the measured and effective permeability models is reduced. The differences between measured and effective permeability values and models indicate why it is important to utilize scale-dependent facies-based permeability values for reservoir mapping at the field scale.

## References

- Al-Raisi, M. H., R. M. Slatt, and M. K. Decker, 1996, Structural and stratigraphic compartmentalization of the Terry Sandstone and effects on reservoir fluid distributions; Latham Bar Trend, Denver Basin; Colorado, *The Mountain Geologist*, vol. 33, no. 1, p. 11-30.
- Cant, D. J., 1992, Subsurface facies analysis, St. Johns, NL, Canada (CAN), Geological Association of Canada, St. Johns, NL.
- Corbett, P. W. M. and J. L. Jensen, 1993, Application of probe permeametry to the prediction of two-phase flow performance in laminated sandstones (lower Brent Group, North Sea), *Marine and Petroleum Geology*, vol. 10, no. 4, p. 335-346.
- de Marsily, G., F. Delay, J. Goncalves, P. Renard, V. Teles, and S. Violette, 2005, Dealing with Spatial Heterogeneity, *Journal of Hydrology*, vol. 13, p. 161-183.
- Delbari, M., P. Afrasiab, and W. Loiskandl, 2009, Using sequential Gaussian simulation to assess the field-scale spatial uncertainty of soil water content, *Catena*, vol. 79, no. 2, p. 163-169.
- Desbarats, A. J., 1987, Numerical estimation of effective permeability in sand-shale formations, *Water Resources Research*, vol. 23, no. 2, p. 273-286.
- Deutsch, C., 1989, Calculating effective absolute permeability in sandstone/shale sequences, *SPE Formation Evaluation*, vol. 4, no. 3, p. 343-348.
- Dickinson, W. R., M. A. Klute, M. J. Hayes, S. U. Janecke, E. R. Lundin, M. A. McKittrick, and M. D. Olivares, 1988, Paleogeographic and paleotectonic setting of Laramide sedimentary basins in the central Rocky Mountain region, *Geological Society of America Bulletin*, vol. 100, no. 7, p. 1023-1039.
- Durlofsky, L. J., 1991, Numerical calculation of equivalent grid-block permeability tensors for heterogeneous porous media, *Water Resources Research*, vol. 27, no. 5, p. 699-708.
- Elfenbein, C., P. S. Ringrose, and M. Christie, 2005, Small-scale reservoir modeling rool optimizes recovery offshore Norway, *World Oil*, vol. 226, no. 10, p. 45-50.
- Goggin, D. J., R. L. Thrasher, and L. W. Lake, 1988, A theoretical and experimental analysis of minipermeameter response including gas slippage and high velocity flow effects, *In Situ*, vol. 12, no. 1-2, p. 79-116.
- Haldorsen, H. H., 1986, Simulator parameter assignment and the problem of scale in reservoir engineering, *in* Lake, L. W. and H. B. Carroll, eds., *Reservoir Characterization*, Orlando, Academic Press, p. 293-340.
- Helsley, R., 1985, Terry Sandstone Member of the Pierre Shale, Upper Cretaceous, Spindle Field, Denver Basin, Colorado, Master's thesis.

Higley, D. K., D. O. Cox, and R. J. Weimer, 2003, Petroleum system and production characteristics of the Muddy (J) Sandstone (Lower Cretaceous) Wattenberg continuous gas field, Denver Basin, Colorado, AAPG Bulletin, vol. 87, no. 1, p. 15-37.

Hurst, A. and K. J. Rosvoll, 1991, Permeability variations in sandstones and their relationship to sedimentary structures, San Diego, CA, United States (USA), Acad. Press, San Diego, CA.

Imam, M. B., 1989, Comparison of burial diagenesis in some deltaic to shallow marine reservoir sandstones from different basins, Journal of the Geological Society of India, vol. 33, no. 6, p. 524-537.

Jackson, M. D., A. H. Muggeridge, S. Yoshida, and H. D. Johnson, 2003, Upscaling Permeability Measurements Within Complex Heterolithic Tidal Sandstones, Mathematical Geology, vol. 35, no. 5, p. 499-520.

Kiteley, L. W., 1978, Hydrocarbon accumulation in Cretaceous shallow-marine sandstones of the northern Denver Basin, vol. P 1100, p. 20.

Kiteley, L. W., 1975, Chart showing correlation of Upper Cretaceous rocks in the northern Denver Basin, Colorado and Wyoming, with other areas in eastern Wyoming, , vol. OF 75-0033.

Kiteley, L. W., 1977, Shallow marine deposits in the Upper Cretaceous Pierre Shale of the northern Denver Basin and their relation to hydrocarbon accumulation; Exploration frontiers of the central and southern Rockies, Field Conference - Rocky Mountain Association of Geologists, vol. 1977, p. 197-211.

Ladd, J. H., 2005, An Overview and Development History of the Wattenberg Field, Rocky Mountain Association of Geologists.

Larese, R. E., 2008, Petrographic Analysis of Selected Sussex-Shannon Sandstone Core Plug Specimens from the Haller CR 32-11 #1 Well, Spindle Field, Weld County, Colorado, , vol. REL-2008-30.

Moredock, D. E. and S. J. Williams, 1976, Upper Cretaceous Terry and Hygiene sandstones; Singletree, Spindle and Surrey fields; Weld County, Colorado, Professional Contributions of the Colorado School of Mines, no. 8, p. 264-274.

Nordahl, K., P. S. Ringrose, and R. Wen, 2005, Petrophysical characterization of a heterolithic tidal reservoir interval using a process-based modelling tool, Petroleum Geoscience, vol. 11, no. 1, p. 17-28.

Nordahl, K. and P. S. Ringrose, 2008, Identifying the Representative Elementary Volume for Permeability in Heterolithic Deposits Using Numerical Rock Models, Mathematical Geosciences, vol. 40, no. 7, p. 753-771.

Pickup, G. E., P. S. Ringrose, J. L. Jensen, and K. S. Sorbie, 1994, Permeability tensors for sedimentary structures, Mathematical Geology, vol. 26, no. 2, p. 227-250.

Pittman, E. D., 1988, Diagenesis of Terry Sandstone (Upper Cretaceous), Spindle Field, Colorado, *Journal of Sedimentary Petrology*, vol. 58, no. 5, p. 785-800.

Pittman, E. D., 1989, Nature of the Terry Sandstone reservoir, Spindle Field, Colorado, Denver, CO, United States (USA), *Rocky Mt. Assoc. Geol.*, Denver, CO.

Porter, K. W., 1976, Marine shelf model, Hygiene Member of the Pierre Shale, Upper Cretaceous, Denver Basin, Colorado; *Studies in Colorado field geology*, Professional Contributions of the Colorado School of Mines, no. 8, p. 251-263.

Porter, K. W. and R. J. Weimer, 1982, Diagenetic sequence related to structural history and petroleum accumulation; Spindle Field, Colorado, *AAPG Bulletin*, vol. 66, no. 12, p. 2543-2560.

Raynolds, R. G., 2002, Upper Cretaceous and Tertiary stratigraphy of the Denver Basin, Colorado; Paleontology and stratigraphy of Laramide Strata in the Denver Basin (Part I), *Rocky Mountain Geology*, vol. 37, no. 2, p. 111-134.

Renard, P. and G. de Marsily, 1997, Calculating equivalent permeability; a review, *Advances in Water Resources*, vol. 20, no. 5-6, p. 253-278.

Ringrose, P. S., K. Nordahl, and R. Wen, 2005, Vertical permeability estimation in heterolithic tidal deltaic sandstones, *Petroleum Geoscience*, vol. 11, no. 1, p. 29-36.

Ringrose, P., K. Sorbie, F. Feghi, G. Pickup, and J. Jensen, 1993, Relevant Reservoir Characterization - Recovery Process, Geometry, and Scale, *In Situ*, vol. 17, no. 1, p. 55-82.

Rubin, D. M., 1987, Cross-bedding, bedforms, and paleocurrents, Tulsa, OK, United States (USA), *Soc. Econ. Paleontol. and Miner.*, Tulsa, OK, 187 p.

Slatt, R. M., D. H. Edington, and A. A. Fursova, 1997, Shoreface sequence stratigraphy of the Upper Cretaceous Terry Sandstone in Denver Basin, Colorado; *AAPG Rocky Mountain Section meeting; abstracts*, *AAPG Bulletin*, vol. 81, no. 7, p. 1234.

Sloan, J. A., 2012, Stratigraphic architecture and connectivity of a low net-to-gross fluvial system: Combining outcrop analogs and multiple-point geostatistical modeling, lower Williams Fork Formation, Piceance Basin, Colorado, M.S. thesis, University of Colorado at Boulder, United States -- Colorado.

Tidwell, V. C. and J. L. Wilson, 1997, Laboratory method for investigating permeability upscaling, *Water Resources Research*, vol. 33, no. 7, p. 1607-1616.

Walker, R. G. and K. M. Bergman, 1993, Shannon Sandstone in Wyoming; a shelf-ridge complex reinterpreted as lowstand shoreface deposits, *Journal of Sedimentary Petrology*, vol. 63, no. 5, p. 839-851.

Weber, K. J., 1982, Influence of common sedimentary structures on fluid flow in reservoir models, *JPT. Journal of Petroleum Technology*, vol. 34, no. 3, p. 665-672.



Weimer, R. J., 1978, Influence of transcontinental arch on Cretaceous marine sedimentation; a preliminary report, Rocky Mountain Association of Geologists, vol. 1978, p. 211-222.

Weimer, R. J., S. A. Sonnenberg, and G. B. C. Young, 1986, Wattenberg Field, Denver Basin, Colorado; Geology of tight gas reservoirs, AAPG Studies in Geology, vol. 24, p. 143-164.

Weimer, R. J. and S. A. Sonnenberg, 1996, Guide to the petroleum geology and Laramide Orogeny, Denver Basin and Front Range, Colorado, Bulletin - Colorado Geological Survey, Department of Natural Resources, p. 127.

Wen, R., A. W. Martinius, A. Naess, and P. Ringrose, 1998, Three-dimensional simulation of small-scale heterogeneity in tidal deposits—a process-based stochastic simulation method, *in* Buccianit, A., G. Nardi, and R. Potenza, eds., Proceedings of the 4th annual conference of the International Association of Mathematical Geology (IAMG), Ischia, p. 129-134

Wen, R., 2008, Upscaling core plug data to reservoir modelling grid; a small-scale heterogeneity modelling approach, *Reservoir*, vol. 35, no. 6, p. 12.

Wen, X. and J. J. Gomez-Hernandez, 1996, Upscaling hydraulic conductivity in heterogeneous media; an overview, *Journal of Hydrology*, vol. 183, no. 1-2, p. ix-xxxii.

Worthington, P. F., 1994, Effective integration of core and log data, *Marine and Petroleum Geology*, vol. 11, no. 4, p. 457-466.

## **Appendix A**

### Facies and Core Descriptions

### ***Geologic Setting and Information***

During the deposition of the Hygiene Formation, the Denver Basin was part of the Cretaceous Western Interior Seaway (Raynolds, 2002; Weimer, 1996). Deep marine shales were deposited in the Western interior seaway, which in the Denver Basin correspond to the Pierre Shale. Correlative deep marine shales are also present in other Rocky Mountain basins as well and are all associated with the seaway. The Cretaceous Western Interior Seaway was partitioned during the Laramide orogenic event and drained when the entire area was uplifted. During this time the Denver Basin was formed as episodic downwarping of the crust caused structural lows to form just to the west of the rising mountain ranges. The Denver Basin is bounded by structural features in the north, south, and west but has no definitive structural boundary in the east (Figure 16) (Weimer, 1996). In the west the Rocky Mountain Front Range provides the structural boundary for the basin while the basin is bounded in the south by the Apishipa Arch. In the north the basin is bounded by the Hartville uplift and Cambridge-Chadron Arch. Additionally in the north a small sub-basin within the broader Denver Basin is seen. It contains the same structural boundaries to the north, east, and west but is separated from the deeper Denver Basin by the Greely Arch in the south.

### ***Core and Facies Descriptions***

This study utilized four cores located around the Wattenberg and Spindle field areas of the Denver Basin. The cores for this study were chosen based on the availability and accessibility of the cores, log data availability for cored wells, and clarity of facies for ease of identification and modeling. Three of the four cores are located at the University of Colorado-Boulder while the fourth is located at the USGS Core Research Center in Golden, Colorado. While two of these cores were used for near-wellbore modeling, the other two cores were only used for permeability acquisition. The McHale #1 and Champlin 369 cores used for the modeling were described in detail (Figures 17; Figure 18). The Moser #1 and Sidwell cores

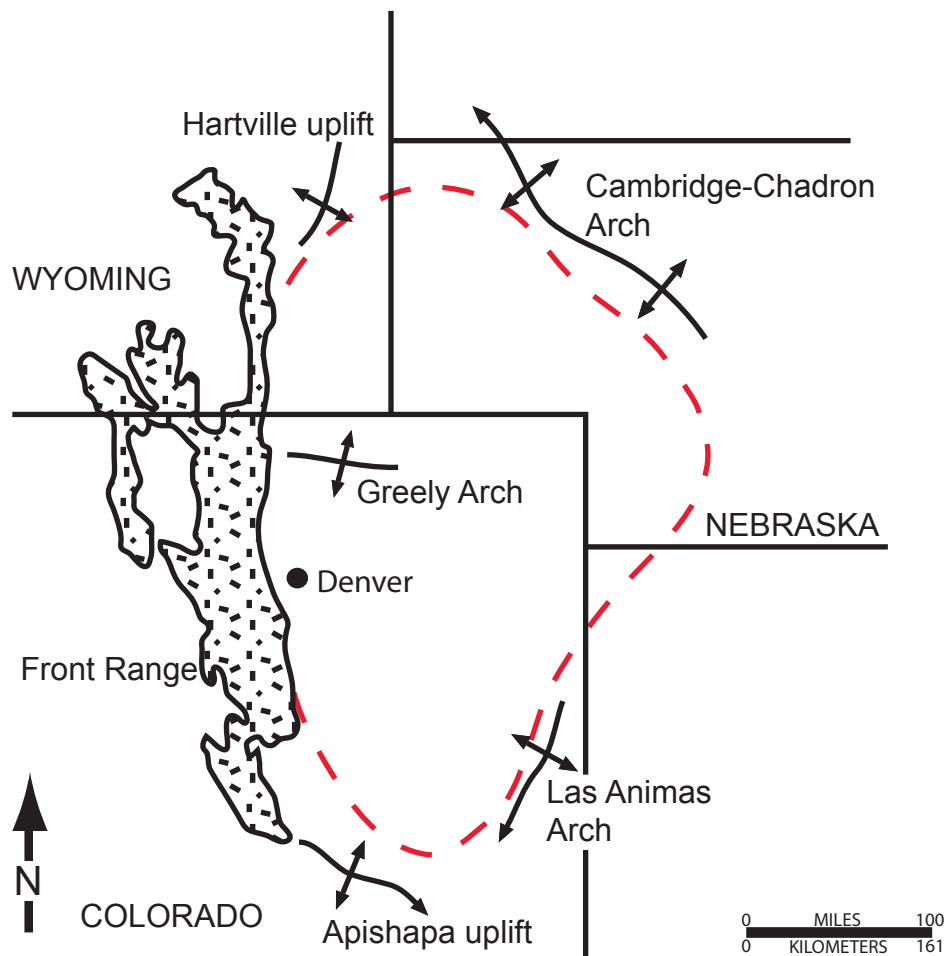


Figure 16. Schematic map of Denver Basin (outlined in red) showing the structural boundaries in the north, south, and west. There is no defined structural boundary in on the east side of the basin. Modified from Weimer et al. (1986) and Dickinson et al. (1988).







were used to acquire permeabilities from the Terry and the Hygiene formations and combined with the data collected from the McHale #1 and Champlin 369 cores create the full permeability data set used.

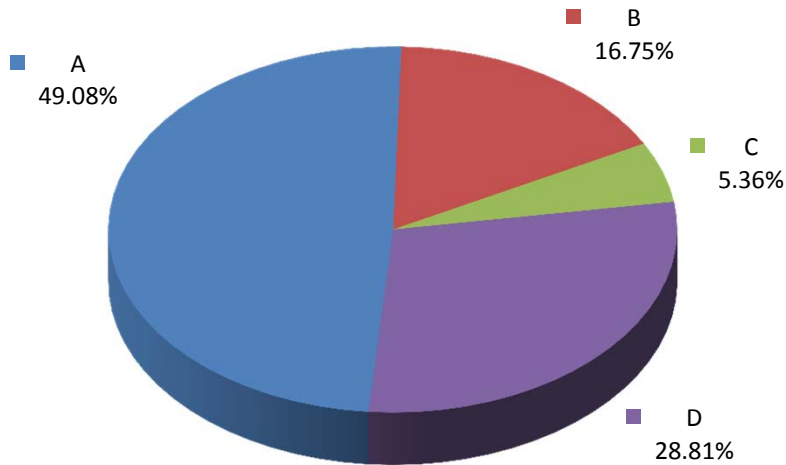
Detail sedimentary descriptions of the cores lead to the identification of four lithofacies based on sedimentary structures and lithology. These lithofacies were identified in all four cores (Figure 4) and include wavy laminated sandstone, planar cross-laminated sandstone, ripple cross-laminated sandstone, and structureless sandstone. These facies are repeated throughout the entire Terry and Hygiene formations and with varying thicknesses and abundances (Figure 19; Figure 20). Similar facies were identified by previous studies and indicate several potential depositional environments (Kiteley, 1976; Porter, 1976; Al-Raisi et al, 1996; Helsley, 1985; L. Kiteley, personal communication).

Facies A is a wavy laminated sandstone that consists of alternating sandstone and mudstone laminae and comprises approximately 50% of the total cored interval (Figure 19). Bioturbation is present and is the likely cause of some to all of the wavy beds. The bioturbated sandstone and mudrock lamina both have similar petrophysical properties to other non-bioturbation lamina elsewhere in the core. Facies A is considered a silty sandstone based on the amount of mudrock present in the samples. Mud laminations comprise between 10 and 50% of the facies with wave amplitude and wavelength of only several centimeters. The variation in mud is associated with both the bioturbation, creatures bringing mud in from above or below, as well as with changes in depositional environment. The more mud-dominated wavy laminated facies are likely formed in quiet water settings indicating that sea level may have dropped locally for a short period of time, causing shelf currents to move further offshore which did not affect this area.

Facies B, planar laminated sandstone, represents approximately 20% of the facies identified in all of the cores. The planar laminated sandstones have dips ranging from 0-15° with the majority dipping around 5-10°. As the cores were not oriented, dip direction could not be



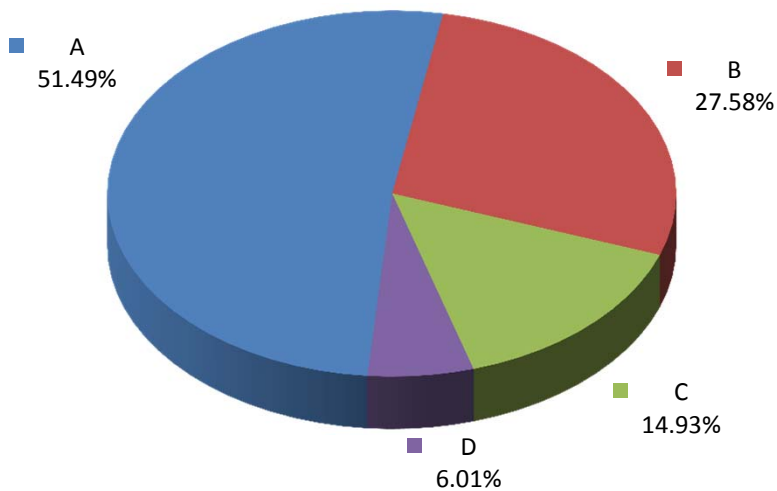
Facies Code	Total Footage (ft)	Total %	Arithmetic Average (in)	Standard Deviation (in)
A	13.27	49.10%	2.488	1.938
B	4.53	16.80%	1.754	1.025
C	1.45	5.40%	2.032	1.628
D	7.79	28.70%	1.160	0.607



Facies A - Wavy Laminated Sandstone  
Facies B - Planar Laminated Sandstone  
Facies C - Ripple Cross-laminated Sandstone  
Facies D - Structureless Sandstone

Figure 19. Facies, facies percentages, and average thicknesses of each facies used in near-wellmore modeling process for the McHale #1 core. Facies A represents the non-reservoir intervals while facies B, C, and D comprise mostly reservoir intervals.

Facies Code	Total Footage (ft)	Total %	Avg. Facies Thickness (in)	Standard Deviation (in)
A	23.04	51.49%	3.950	3.411
B	12.34	27.58%	3.365	2.880
C	6.68	14.93%	2.358	2.374
D	2.69	6.01%	2.483	0.937



Facies A - Wavy Laminated Sandstone  
 Facies B - Planar Laminated Sandstone  
 Facies C - Ripple Cross-laminated Sandstone  
 Facies D - Structureless Sandstone

Figure 20. Facies, facies percentages and average thicknesses for each facies used in the near-wellbore modeling for the Champlin 369 core. Facies A represents mostly non-reservoir intervals and facies B, C, and D represent reservoir intervals.

determined and therefore it was assumed that all lamina dip in the same direction. The general pattern observed in mudrock laminae is densely spaced mudrock layers at the base that decrease in density towards the top. Additionally, of all the facies identified, this one appears to contain the least amount of bioturbation. This is likely caused by the higher energy settings in which planar lamina were deposited.

Facies C is a structureless sandstone that contains very little to no mudrock present. It represents approximately 5% of the total facies observed in core. The structureless sandstone can be interpreted as forming in two distinct ways. Both of these interpretations are equally as likely to have occurred based on the depositional setting and lack of evidence indicating either at any facies occurrence. The first possible interpretation is that these are storm deposits that are deposited so rapidly that they do not have time to form coherent layers. As deposition was in relatively shallow water (less than 100 ft (30.5 m)), large storms may have swept large volumes of sand out to sea. Additionally, these deposits may be interpreted as being related to bioturbation. Sand deposited by any process may subsequently have been so extensively bioturbated that it was completely homogenized creating a sandstone that has no structure. Due to the level of bioturbation in the area and surrounding facies, this is a quite viable interpretation. As the structureless sandstones tend to show no significant petrophysical differences, it can be assumed that the exact nature of its origin is not critical to this study.

Facies D contains ripple foresets and was interpreted to be a ripple cross-laminated sandstone. This facies represented approximately 30% of the facies noted in the described cores and averaged just a few inches thick in most places. The ripple laminated sandstones had amplitudes measured in the tenths of inches with wavelengths of 1-2 in (2.5-5 cm). Similar to the planar laminated sandstone above, migration direction of the ripple laminated sandstone was not able to be determined so it was assumed the migration direction of all occurrences of this facies was uniform.

### ***Depositional Environment***

Over the last 40-plus years, the Terry Formation (and to a lesser extent the Hygiene Formation) have been studied in an attempt to determine their characteristics are and their origins (Moredock and Williams, 1976; Porter, 1976; Kiteley, 1977, 1978; Porter and Weimer, 1982; Helsley, 1985; Pittman, 1989; Walker and Bergman, 1993; Al-Raisi et al., 1995; Ladd, 2005; E. G. Gustason, 2012, personal communication). Possible depositional environments for the Terry Formation might include: offshore bars, shoreface beach sands, and deltaic sediments. All of these depositional models fit the environment at the time of deposition, which consisted of the shallow epeiric Cretaceous Western Interior Seaway (Figure 21) (Kiteley, 1977; Ladd, 1995; Al-Raisi et al., 1996; Slatt et al., 1997; Ladd, 2005). The Hygiene Formation is considered to have a similar depositional environment but was more likely a deltaic sandstone deposit (Kiteley, 1977). Based on the facies observed in this study, an offshore bar complex is interpreted as the likely depositional environment for the Terry and Hygiene formations. Porter (1976) provides a good model for the depositional setting of both formations (Figure 22). The offshore bars (and to a lesser extent offshore sheet sandstones) likely formed as sand was moved away from the shoreline by longshore currents. Currents in part of the Cretaceous Western Interior Seaway would have sourced sediments from a nearby delta. The delta that brought sediments to the seaway is problematic, with some authors indicating that it may have been the large Parkman delta in present day Wyoming (Porter and Weimer, 1989). The source of these sediments would have likely been shed from the mountains west of the Cretaceous Western Interior Seaway as both formations lie on the western side of the seaway. Using well log analysis, Cant (1992) provides further evidence of an offshore depositional setting by using a method of well-log comparisons to units with accepted depositional environment interpretations. Cant provides broad “type curves” for formations with different depositional environments including an offshore bar complex. The primary log suites used by Cant (1992) include gamma-ray (GR) and/or spontaneous potential (SP) logs (Figure 23). Cross-sections of

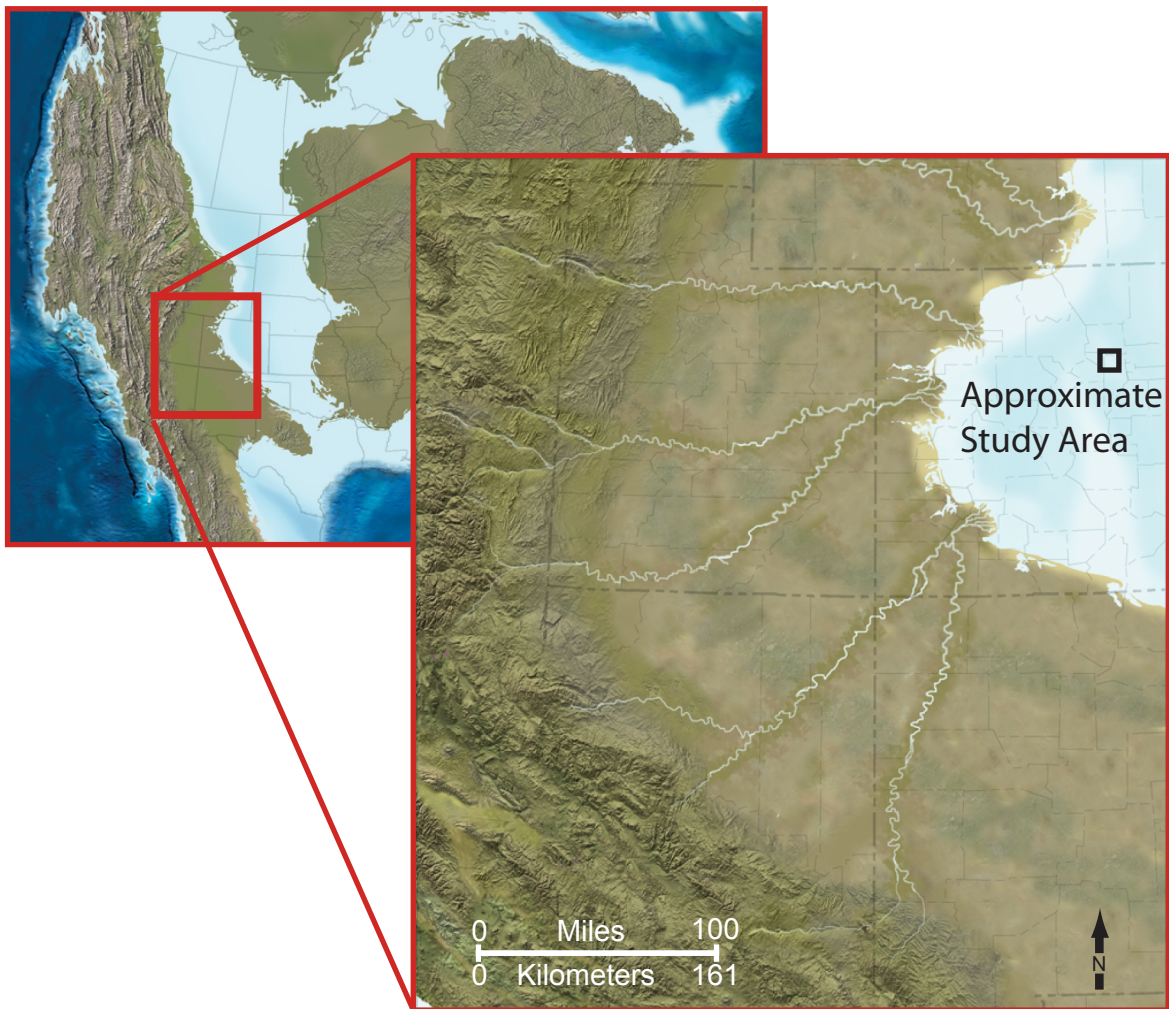


Figure 21. Paleogeographic map of western United States during the Late Cretaceous Campanian age showing the approximate depositional environment of the Terry and Hygiene formations. The Terry and Hygiene formations were both likely deposited in a shallow marine environment relatively near a delta located to the west. Modified from Blakey (1997).

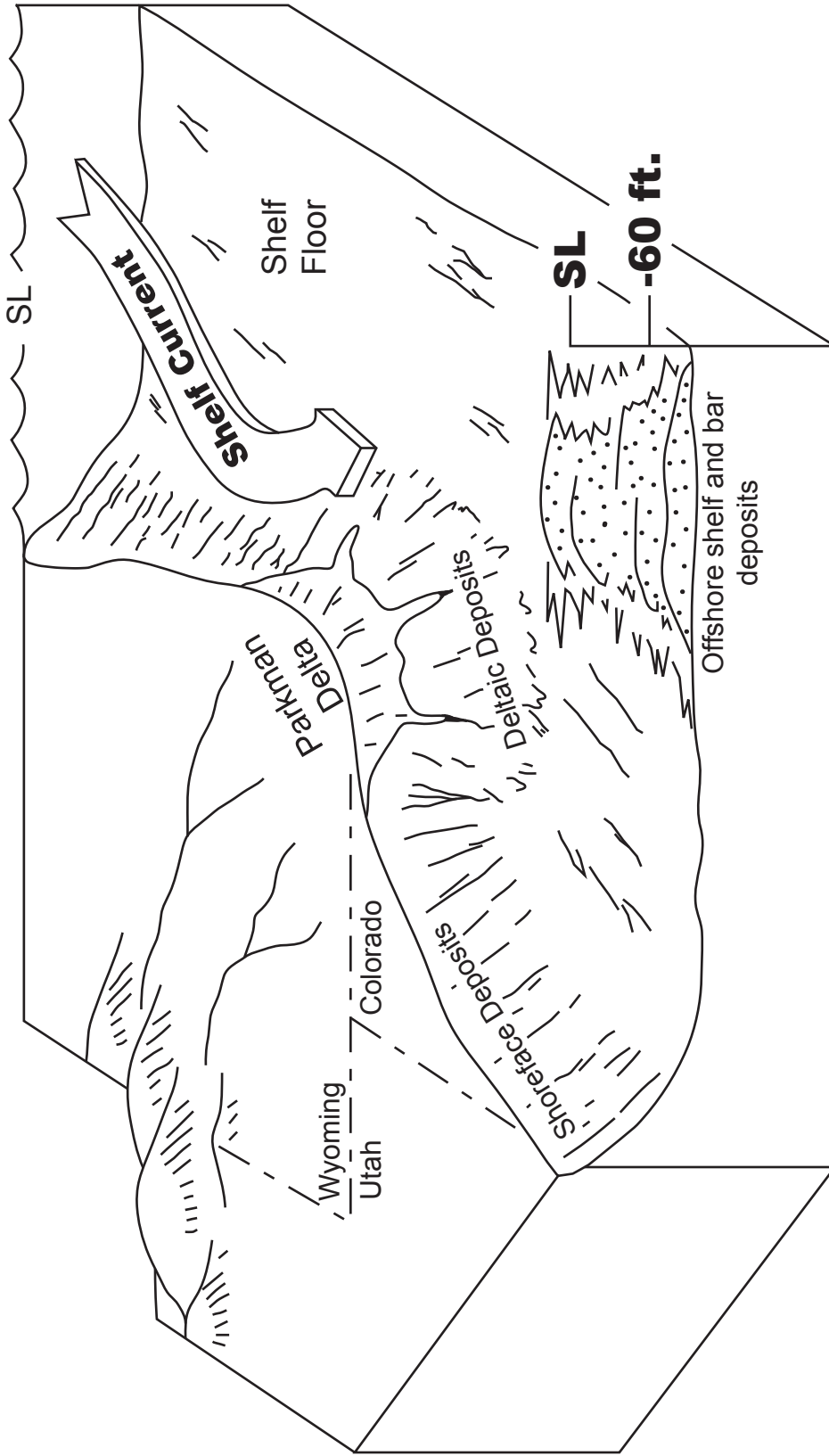


Figure 22. Block diagram of interpreted depositional environments of the Terry and Hygiene formations. This study interprets the environment of deposition for both as offshore shelf and bar complex deposits. SL = Sea Level. Modified from Porter (1978).

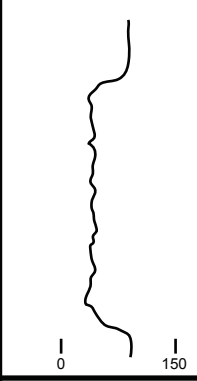
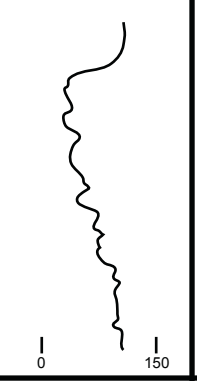

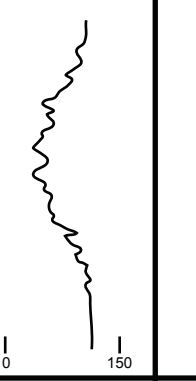
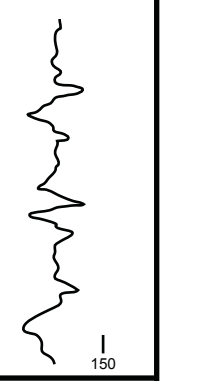
Shape:	Cylindrical	Funnel Shaped	Bell Shaped	Symmetrical	Irregular
Trend:	Clean, No Trend	Abrupt Top Coarsening Upward	Abrupt Base Fining Upward	Rounded Base and Top	Mixed Clean and Shaly, No trend
Typical Gamma-Ray log response					
Interpretation:	aeolian, braded fluvial, carbonate shelf, reef, submarine canyon fill	crevasse splay, distributary mouth bar, clastic strand plain, barrier island, shallow marine sheet sandstone, carbonate shoaling-upward sequence, submarine fan lobe.	fluvial point bar, tidal point bar, deep sea channel, some transgressive shelf sands	sandy offshore bar, some transgressive shelf sands, amalgamated CU and FU units	fluvial floodplain, carbonate slope, clastic slope, canyon fill

Figure 23. Typical gamma-ray response for different depositional environments as determined from log responses. This interpretation method was determined from core-to-log comparisons and can be useful in determining depositional environments. Log interpretation and core descriptions are used to determine depositional environments for the Terry Formation. Modified from Cant (1992) and Sloan (2011).

nearly all logs used in this study are provided in figure 6 and show what Cant (1992) calls a symmetric log shape and a funnel log shape, which indicates a potential offshore bar depositional setting. The symmetric SP (and to a lesser extent GR) log response has been previously shown to represent offshore sandstone bars while the funnel shape log responses may indicate several different environments including shallow marine sheet sandstones. With presence of both of these log shapes in all the Terry and Hygiene formation logs, the depositional environment may be aligned with what Kiteley (1977), Porter and Weimer (1989), and Al-Raisi et al. (1996) interpret as being an offshore bar complex. As previously discussed in a previous section, the facies also provide evidence for a potential offshore bar complex with zones of rapid bar build up and zones of slower deposition and quieter water settings being shown.

### ***Nomenclature***

Nomenclature of the Terry and Hygiene formation has become muddled between industry and academic use. The Terry Formation is commonly referred to in the petroleum industry as the Sussex Formation while the Hygiene Formation is known as the Shannon Sandstone (Moredock and Williams, 1976; Kiteley, 1977). These names come from the better known Sussex and Shannon formations of the Powder River Basin. It was assumed when first encountered that these formations were time equivalent members of the Pierre and Steele shale formation in the Denver and Powder River basins respectively. However, after dating of the formations through ammonite fossil assemblages, the Terry-Sussex formations and the Hygiene-Shannon formations were shown to be of different ages and thus not equivalent (Figure 24). However, given the similar nature of the four formations, their depositional environments may be similar with the Sussex and Shannon formations being sourced from the Parkman Delta in Wyoming and being called shelf-ridge complexes (Porter and Weimer, 1982; Walker and Bergman, 1993).



Period & Stage		Western Interior Ammonite Zones	Previous Denver Basin Studies	Denver Basin <sup>1</sup>	Powder River Basin <sup>2</sup>
Upper Cretaceous	Maastrichtian				
		Hoploscophites nicolleti			
		Sphenodiscus	Fox Hills Sst	Fox Hills Sst	Fox Hills Sst
		Baculites dinolobatus	Shale	Shale	Lewis Shale
		Baculites grandis			
	Baculites bacolus				
	Baculites elias				
	Baculites jenseni				
	Campanian	Baculites reesidei	Richard, Larimer, & Rocky Ridge Sst members	Richard, Larimer, & Rocky Ridge Sst members	Teapot Sst
		Baculites cuneatus	Silty Shale	Shale and Siltstone	
		Baculites compressus			
		Didymoceras cheyennense	Sussex Sst	Terry Sst	
		Exiteloceras jenneyi	Silty Shale	Siltstone	
		Didymoceras sterenoni			
		Didymoceras nebrascense	Shannon Sst	Hygiene Sst	Shale
		Baculites scotti			
		Baculites gregoryensis	Shale	Shale	Parkman Sst member
		Baculites perplexus			
		Baculites sp. (smooth)			
		Baculites asperiformis			
		Baculites mclearni			
		Baculites obtusus			
		Baculites sp. (weak flank ribs)			
		Baculites sp. (smooth)			
		Scaphites hippocrepis III	Niobrara Formation	Niobrara Formation	Shale
		Scaphites hippocrepis II			
		Scaphites hippocrepis I			
		Santonian	Desmoscaphites bassleri	Niobrara Formation	Niobrara Formation
	Desmoscaphites eramanni				

Figure 24. Stratigraphic nomenclature chart for the Denver and Powder River Basins. This study follows the Denver Basin nomenclature established by Kiteley (1970). Modified from (1) Kiteley, (1970) and (2) Gill et al., (1970).

## **Reservoir Zones**

Using digital logs available for the wells in the study area along with core observations and permeability data, four reservoir zones were identified (Figure 5; Figure 25). These zones, the Top Terry, Terry A, Terry B, and Terry C are determined to be both reservoir and non-reservoir, based on the facies present and the facies permeabilities (Figure 5). Reservoir zones are characterized by negative SP shifts, higher resistivity, increased porosity, higher permeabilities (depending on facies), and facies consisting mainly of structureless sandstone and planar cross-laminated sandstone with varying amounts of ripple cross-laminated sandstone. Non-reservoir zones are characterized by SP values on or near the baseline (more positive than reservoir zones), resistivities around 1-2 ohm-meters, lower porosity and permeability values, predominantly wavy laminated sandstone facies. This facies is more mudrock-rich and it's likely the reason why it is most common in non-reservoir zones. These zones can be seen in cross-sectional view as having varying thicknesses, which is likely associated with varying sand bar sizes (Figure 6). Reservoir zones can be visually identified in core by looking at mudrock content and color. Non-reservoir zones tend to be darker (high mud content), while reservoir zones will appear lighter, due to the sparse amount of mud present (Figure 25).

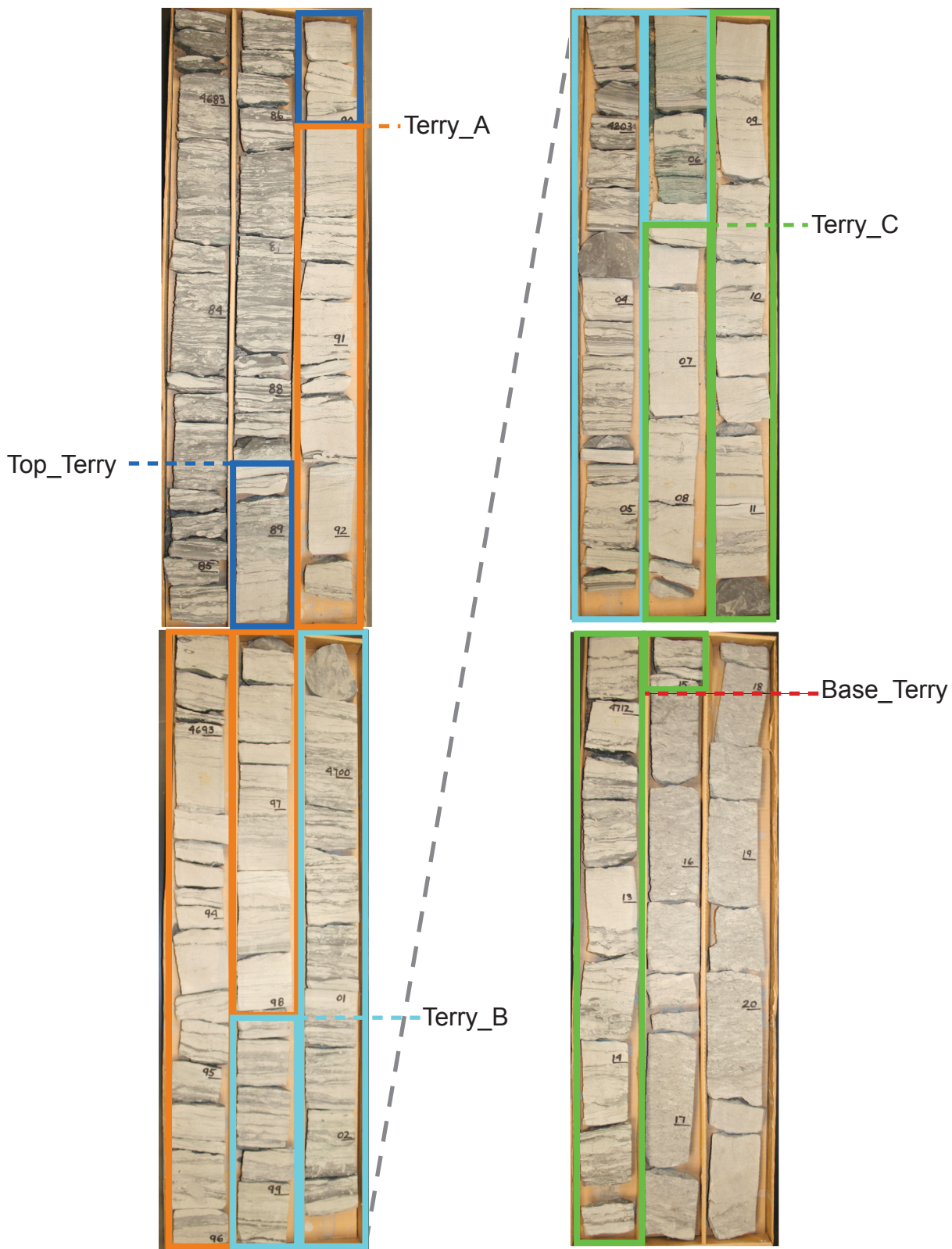


Figure 25. McHale #1 core with reservoir zones (Terry Top, A, B, and C) outlined. Colors correspond to zone tops shown in type log (Figure 5). Non-reservoir zones appear a darker color due to the higher mudrock content. This mudrock adversely affects reservoir properties making it a non-reservoir zone. Reservoir zones appear lighter in color and are cleaner sandstones.

## **Appendix B**

### Permeability Acquisition and Results

### **Permeability Acquisition**

Permeabilities were acquired from four cores in Spindle Field, Denver Basin, Colorado (Figure 1). A probe-permeameter at the University of Colorado-Boulder was used due to its ability to rapidly capture permeability data, to capture individual lamina permeabilities, and to acquire a large amount of data inexpensively. The permeameter works by flowing nitrogen gas through the core sample and measuring the pressure in the gas line. The flow rate of nitrogen gas is controlled by a valve that affects the flow pressure of nitrogen gas in the gas line leading to the sample. When the pressure in the gas line reaches the same pressure as the atmospheric pressure, the flow rate of nitrogen gas into the sample is consistent with the nitrogen gas flow rate out of the sample. This equilibrium is important as the flow at this point in time is used to calculate the permeability of the sample (equation 1). All permeability data are reported at the end of this appendix

$$K_a = \frac{2\mu Q_b P_b T_{act}}{a G_0 (P_1^2 - P_2^2) T_{ref}} * 1000 \quad (1)$$

where:

$K_a$  = air or gas permeability (mD)

$\mu$  = viscosity of gas flowing through sample (cp)

$Q_b$  = volumetric flow rate standard cc/sec. Used to calculate flow rate where flow rate =  $Q_b / 60$

$P_b$  = standard reference pressure for mass flow meters, (atm)

$P_1$  = upstream pressure (pressure at tip). Flow Pressure (psia)

$P_2$  = downstream pressure (atmospheric pressure, psia)

$a$  = Inside radius of tip (cm)

$G_0$  = Geometrical shale factor

$b_d = b / a$  (used to determine  $G_0$ , dimensionless)

$b$  = external radius of tip (cm)

$R_d = R_{core} / a$  (dimensionless)

$R_{core}$  = core radius (cm)

$L_d = L_{core} / a$  (dimensionless)

$L_{core}$  = length of core (cm)

$T_{ref}$  = reference temperature of mass flow meters (K)

$T_{act}$  = actual flowing temperature of gas (K)

The permeability that is calculated using equation (1) by the permeameter is known in this study as the Temco permeability. It was determined through permeability comparisons that the Temco permeability and standards with known point-permeability measurements that the permeameter could not calculate accurate permeability at high and low values. To counter this issue, the permeabilities reported herein are based on calibration of gas flow rate to known core plug permeabilities that are similar to the expected permeabilities of the Terry and Hygiene formations (Figure 26). The standards are core plugs taken from rocks similar to those used in this study. These permeabilities were measured at a given point on each end of the plug. Measurements of these points were completed by Weatherford Laboratories in Houston, Texas. When collecting permeabilities on Terry and Hygiene formation core samples, these core plug standards were measured at the beginning and end of every day and the values were compared with the measurements defined on the standards previously. If the data range was changed this could indicate a leak in nitrogen gas or other potential problems in the machine. If a potential problem was detected, core data for that day would be resampled to ensure the measurements were correct. Additionally, the 1539 measurements of standards were used to create the calibration curve used to equate gas flow rates through core samples to the core samples permeability. All Temco permeabilities were calibrated after all data was collected. This allowed

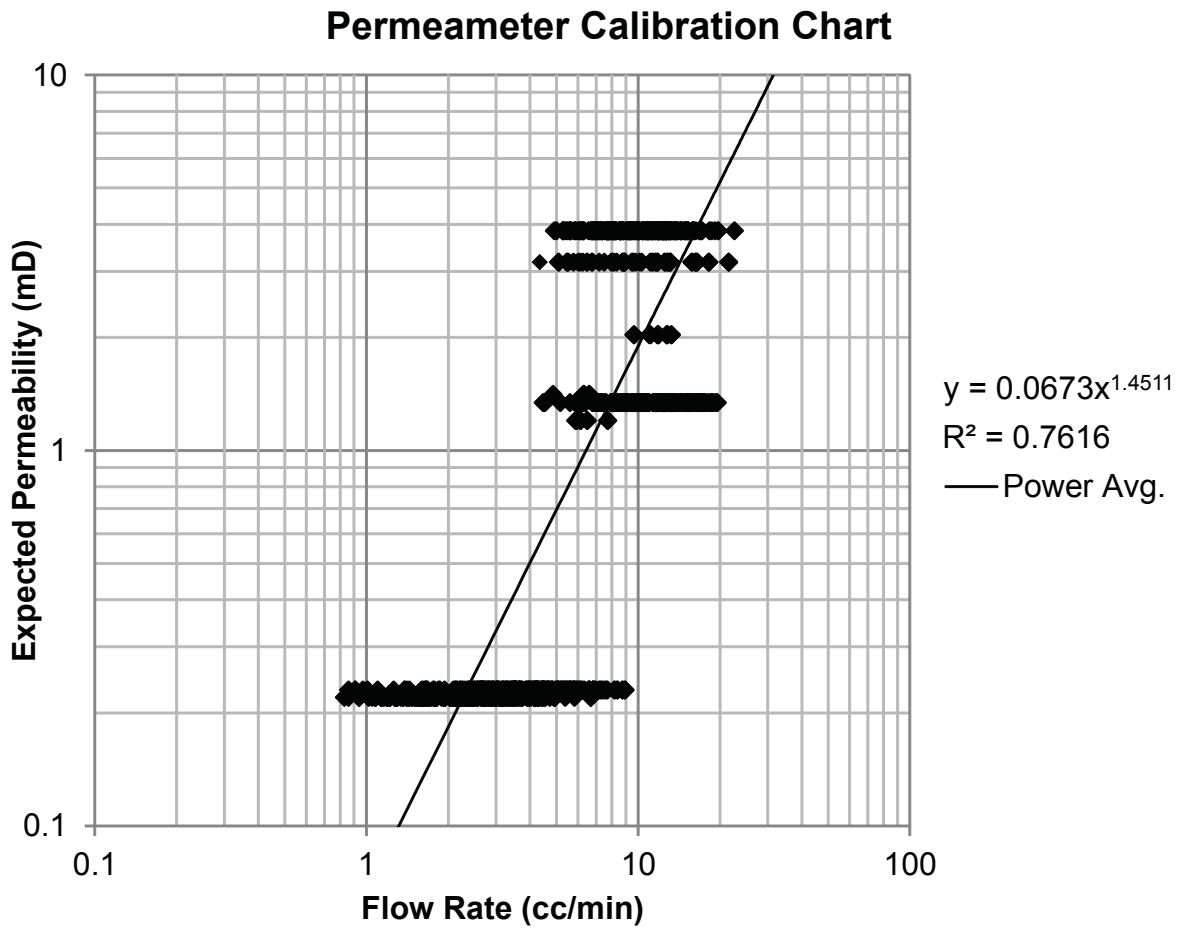


Figure 26. Cross-plot of gas flow rate and known permeabilities of standards used in this study. The best-fit linear regression through this data, the line serves a calibration curve for core measurements and was applied to all measurements on all cores used in this study. N=1539.

for the calibration plot to utilize the maximum amount of data to refine the regression line used for the calibration..

The calibration curve derived from the core-plug standards was applied to all core measures during post-processing. Also during post-processing, each permeability value was evaluated to determine if any anomalous data existed. Due to the nature of the permeameter and the quality of some samples, various anomalies were observed. The anomalous points had high flow rates (permeabilities) that were probably caused by poor tip seals on the core face. Other bad data points that were observed were related to the nature of some lamina, relatively large fractures, or voids that caused the permeability to return abnormally high readings.. Data points were determined to be bad based on observations at the time of the measurement and by evaluation of permeabilities after the data were collected. In post-processing, the data was sorted by facies and lamina type and values that were abnormally high or low were excluded. Typically if a value was larger than one standard deviation from the geometric average of the lamina in that particular facies, the data point was removed. Care was taken at this point to make sure the point was correctly classified as the correct facies. Each suspect data point was compared to the core or core photograph (depending on core availability) at the corresponding depth to determine the facies at the point was measured.

Mudrock lamina also presented a unique challenge for measuring permeabilities. After a significant amount of data from mudrock laminae were collected, a problem with their permeabilities collected was observed. Nearly all mudrock lamina permeabilities were higher than permeabilities observed in the sandstone lamina. It was determined that the mudrock lamina that were large enough to be measured were comprised of multiple mudrock layers that had begun to part along the bedding planes, causing what amount to microfractures to form. These microfractures were likely caused or at least exacerbated by the continual wetting and drying of the cores in decades since their removal from the subsurface. As each lamina was sprayed with water during core descriptions, the mud lamina absorbed the water and expanded



slightly only to contact again as it dried. This would have eventually generated microfractures and higher permeability as the gas flowed preferentially through these fractures. Attempts were made to measure the mudrock perpendicular to the bedding planes so an accurate permeability could be obtained, however this proved difficult. The measurements were taken on surfaces where the core had fractured along mudrock layers. These breaks in the core were often sub-parallel to the lamina so when a measurement was taken, some of the gas was still being flowed through the fractures between bedding planes. Additionally, the nature of the breaks made it difficult to get a good tip seal and to make sure that there was no leaking of nitrogen around the tip. Due to these issues, a definitely and accurate mudrock permeability was unable to be obtained for this study and it was assumed all values would have a permeability of 0.004 mD .

### McHale #1 Core Permeability Data

N2 Flow Press. (psia)	Atm Press. (psia)	Flow Rate (cc/min)	TEMCO Perm (mD)	Calc. Perm (mD)	Core Depth (ft)	Facies
36.29	12.24	4.83	0.663	0.616	4701.00	A
36.26	12.23	10.38	1.426	1.828	4688.33	D
36.28	12.23	8.40	1.153	1.353	4688.33	D
36.28	12.23	9.51	1.305	1.614	4688.33	D
36.23	12.23	17.07	2.350	3.710	4688.33	D
36.22	12.23	13.40	1.846	2.629	4688.33	D
36.22	12.23	17.91	2.468	3.972	4688.33	D
36.25	12.23	14.55	2.001	2.956	4688.33	D
36.25	12.23	5.04	0.693	0.654	4688.33	D
36.30	12.23	8.56	1.174	1.390	4688.33	D
36.26	12.23	2.19	0.301	0.200	4688.33	D
36.16	12.20	6.29	0.871	0.896	4689.58	B
36.22	12.20	1.22	0.168	0.087	4689.58	B
36.21	12.20	3.35	0.463	0.366	4689.58	B
36.20	12.20	0.64	0.088	0.035	4689.58	B
36.18	12.20	1.19	0.165	0.084	4689.58	B
36.18	12.20	4.28	0.592	0.518	4689.58	B
36.23	12.23	5.10	0.703	0.665	4689.58	B
36.21	12.23	5.50	0.759	0.741	4689.58	B
36.21	12.20	4.14	0.572	0.494	4689.58	B
36.22	12.20	0.78	0.108	0.046	4689.58	B
36.21	12.20	3.32	0.459	0.361	4689.58	B
36.19	12.20	5.69	0.787	0.777	4689.58	B
36.22	12.20	2.73	0.377	0.273	4689.58	B
36.16	12.20	5.19	0.719	0.682	4689.58	B
36.19	12.20	15.76	2.179	3.311	4691.08	D
36.23	12.20	6.31	0.870	0.900	4691.08	D
36.24	12.20	4.45	0.613	0.548	4691.08	D
36.19	12.20	12.70	1.756	2.436	4691.08	D
36.25	12.20	9.84	1.355	1.694	4691.08	D
36.18	12.20	13.62	1.884	2.691	4691.08	D
36.19	12.20	9.02	1.247	1.497	4691.08	D
36.24	12.20	8.81	1.214	1.448	4691.08	D
36.16	12.20	9.14	1.265	1.525	4691.08	D
36.21	12.20	9.33	1.288	1.571	4691.08	D
36.21	12.20	5.55	0.766	0.750	4691.92	D
36.23	12.20	8.59	1.183	1.396	4691.92	D
36.20	12.20	7.18	0.992	1.082	4691.92	D
36.18	12.20	10.25	1.417	1.796	4691.92	D
36.25	12.20	13.95	1.920	2.784	4691.92	D
36.25	12.20	11.77	1.620	2.186	4691.92	D
36.23	12.20	10.98	1.513	1.980	4691.92	D
36.24	12.20	10.22	1.408	1.788	4691.92	D
36.24	12.20	11.59	1.597	2.139	4691.92	D
36.20	12.20	5.24	0.724	0.691	4691.92	D
36.23	12.20	7.60	1.048	1.173	4691.92	D
36.22	12.20	7.45	1.028	1.140	4691.92	D
36.19	12.20	5.83	0.806	0.805	4691.92	D
36.21	12.20	6.54	0.903	0.947	4691.92	D
36.23	12.20	6.16	0.849	0.870	4691.92	D
36.22	12.20	6.00	0.828	0.838	4691.92	D
36.23	12.20	7.99	1.101	1.260	4691.92	D
36.19	12.18	5.92	0.813	0.822	4691.92	D
36.14	12.18	6.28	0.865	0.894	4691.92	D
36.21	12.18	8.57	1.177	1.392	4691.92	D
36.22	12.18	5.83	0.800	0.805	4691.92	D
36.18	12.18	4.71	0.648	0.594	4691.92	D
36.21	12.18	6.17	0.848	0.872	4691.92	D

N2 Flow Press. (psia)	Atm Press. (psia)	Flow Rate (cc/min)	TEMCO Perm (mD)	Calc. Perm (mD)	Core Depth (ft)	Facies
36.18	12.18	12.72	1.752	2.441	4693.83	E
36.20	12.18	8.98	1.236	1.488	4693.83	E
36.23	12.18	12.52	1.719	2.387	4693.83	E
36.18	12.18	11.25	1.550	2.050	4693.83	E
36.23	12.18	10.76	1.478	1.924	4693.83	E
36.23	12.18	9.63	1.323	1.643	4693.83	E
36.13	12.18	11.82	1.635	2.199	4693.83	E
36.19	12.18	11.32	1.560	2.068	4693.83	E
36.16	12.18	8.34	1.152	1.339	4693.83	E
36.19	12.18	12.98	1.789	2.512	4693.83	E
36.21	12.18	5.22	0.719	0.687	4694.58	A
36.19	12.18	3.02	0.417	0.316	4694.58	A
36.22	12.18	4.39	0.604	0.537	4694.58	A
36.19	12.18	3.66	0.505	0.415	4694.58	A
36.15	12.18	6.54	0.905	0.947	4694.58	A
36.14	12.18	4.89	0.676	0.626	4694.58	A
36.19	12.18	14.32	1.975	2.889	4694.58	A
36.14	12.18	11.55	1.598	2.128	4694.58	A
36.18	12.18	20.48	2.827	4.807	4694.58	A
36.18	12.18	14.49	2.000	2.938	4694.58	A
36.17	12.18	7.41	1.024	1.132	4694.58	A
36.18	12.18	8.99	1.241	1.490	4694.58	A
36.17	12.18	16.58	2.291	3.559	4694.58	A
36.19	12.21	4.59	0.634	0.573	4695.42	B
36.20	12.21	8.34	1.152	1.339	4695.42	B
36.24	12.21	6.40	0.882	0.919	4695.42	B
36.24	12.21	7.57	1.043	1.167	4695.42	B
36.23	12.21	12.75	1.757	2.449	4695.42	B
36.26	12.21	9.04	1.244	1.502	4695.42	B
36.21	12.21	9.86	1.361	1.699	4695.42	B
36.19	12.21	4.67	0.645	0.587	4695.42	B
36.26	12.21	5.71	0.785	0.781	4695.42	B
36.20	12.21	4.34	0.599	0.529	4695.42	B
36.26	12.21	6.04	0.831	0.846	4695.42	B
36.23	12.21	6.86	0.945	1.014	4695.42	B
36.24	12.21	7.09	0.977	1.063	4695.42	B
36.25	12.21	2.75	0.379	0.276	4695.42	B
36.26	12.21	3.54	0.487	0.396	4695.42	B
36.22	12.21	4.78	0.659	0.607	4695.42	B
36.26	12.21	5.62	0.773	0.764	4695.42	B
36.26	12.21	5.22	0.718	0.687	4695.42	B
35.25	12.21	2.91	0.427	0.299	4695.42	B
36.25	12.21	4.05	0.558	0.479	4696.58	D
36.19	12.21	5.23	0.723	0.689	4696.58	D
36.24	12.21	4.73	0.652	0.598	4696.58	D
36.17	12.21	4.32	0.598	0.525	4696.58	D
36.21	12.21	6.87	0.948	1.016	4696.58	D
36.19	12.21	5.41	0.748	0.723	4696.58	E
36.18	12.21	8.68	1.200	1.417	4696.58	E
36.18	12.21	6.37	0.881	0.913	4696.58	E
36.20	12.21	6.42	0.887	0.923	4696.58	E
36.19	12.21	7.15	0.988	1.076	4696.58	E
36.25	12.21	6.47	0.891	0.933	4697.25	D
36.22	12.21	5.61	0.774	0.762	4697.25	D
36.18	12.21	3.29	0.455	0.356	4697.25	D
36.26	12.21	5.62	0.773	0.764	4697.25	D
36.31	12.27	5.13	0.699	0.671	4697.25	D
35.30	12.27	3.54	0.514	0.396	4697.25	D
36.29	12.27	3.71	0.507	0.423	4697.25	D
36.29	12.27	6.27	0.857	0.892	4697.25	D
36.27	12.27	6.05	0.828	0.848	4697.25	D

N2 Flow Press. (psia)	Atm Press. (psia)	Flow Rate (cc/min)	TEMCO Perm (mD)	Calc. Perm (mD)	Core Depth (ft)	Facies
36.27	12.27	2.68	0.367	0.266	4697.25	D
36.25	12.27	3.90	0.535	0.454	4697.25	D
36.30	12.27	3.65	0.500	0.413	4697.25	D
36.23	12.24	4.25	0.586	0.513	4697.25	D
36.27	12.24	2.82	0.388	0.286	4697.25	D
36.23	12.24	3.45	0.475	0.381	4697.25	D
36.22	12.24	3.27	0.451	0.353	4697.25	D
36.28	12.24	2.84	0.390	0.289	4697.25	D
36.25	12.24	2.37	0.326	0.224	4697.25	D
36.27	12.24	1.57	0.216	0.124	4697.25	D
36.25	12.24	2.74	0.377	0.275	4697.25	D
36.22	12.24	1.47	0.203	0.113	4697.25	D
36.26	12.24	2.39	0.329	0.226	4697.25	D
36.25	12.27	3.30	0.454	0.358	4697.92	D
36.20	12.24	2.47	0.341	0.237	4697.92	D
36.27	12.24	2.97	0.408	0.308	4697.92	D
36.28	12.27	2.39	0.328	0.226	4697.92	D
36.26	12.27	5.63	0.774	0.766	4697.92	D
36.26	12.27	2.34	0.322	0.220	4697.92	D
36.29	12.27	5.24	0.719	0.691	4697.92	D
36.27	12.27	3.21	0.441	0.344	4697.92	D
36.32	12.27	2.92	0.400	0.301	4697.92	D
36.22	12.24	1.65	0.228	0.134	4699.08	C
36.24	12.24	4.44	0.612	0.546	4699.08	C
36.27	12.24	3.72	0.512	0.425	4699.08	C
36.27	12.24	3.11	0.428	0.329	4699.08	C
36.27	12.24	4.27	0.587	0.517	4699.08	C
36.25	12.24	1.07	0.147	0.072	4699.08	D
36.24	12.24	2.48	0.342	0.238	4699.08	D
36.24	12.24	2.79	0.385	0.282	4699.08	D
36.19	12.24	1.92	0.265	0.166	4699.08	D
36.23	12.24	5.66	0.780	0.771	4701.00	D
36.24	12.24	2.29	0.315	0.213	4701.00	D
36.26	12.24	5.81	0.799	0.801	4701.00	D
36.25	12.24	3.72	0.512	0.425	4701.00	D
36.29	12.24	5.67	0.778	0.773	4701.00	D
36.27	12.24	6.69	0.920	0.979	4701.00	D
36.26	12.24	7.64	1.051	1.182	4701.00	D
36.25	12.24	9.28	1.277	1.559	4701.00	D
36.27	12.24	0.95	0.131	0.061	4701.00	D
36.25	12.24	2.09	0.288	0.187	4701.00	D
36.25	12.24	0.70	0.096	0.039	4701.00	D
36.20	12.24	3.19	0.440	0.341	4701.00	D
36.28	12.24	2.92	0.401	0.301	4701.00	D
36.29	12.24	7.67	1.053	1.189	4701.00	D
36.29	12.24	8.60	1.181	1.399	4701.00	D
36.29	12.25	1.77	0.241	0.148	4702.83	A
36.25	12.25	4.26	0.583	0.515	4702.83	A
36.29	12.25	6.13	0.837	0.864	4702.83	A
36.28	12.25	2.10	0.287	0.188	4702.83	A
36.28	12.25	2.00	0.274	0.176	4702.83	A
36.29	12.25	4.26	0.582	0.515	4704.92	C
36.23	12.25	4.96	0.681	0.639	4704.92	C
36.25	12.25	4.77	0.654	0.605	4704.92	C
36.20	12.25	2.73	0.376	0.273	4704.92	C
36.23	12.25	3.81	0.524	0.439	4704.92	C
36.26	12.25	3.42	0.469	0.377	4704.92	C
36.25	12.25	3.79	0.520	0.436	4704.92	C
36.28	12.25	2.24	0.308	0.206	4705.92	D
36.23	12.25	2.89	0.398	0.296	4705.92	D
36.27	12.25	3.07	0.422	0.323	4705.92	D

N2 Flow Press. (psia)	Atm Press. (psia)	Flow Rate (cc/min)	TEMCO Perm (mD)	Calc. Perm (mD)	Core Depth (ft)	Facies
36.29	12.25	1.56	0.214	0.123	4705.92	D
36.27	12.25	3.86	0.530	0.447	4705.92	D
36.29	12.25	6.60	0.905	0.960	4705.92	D
36.26	12.25	4.41	0.606	0.541	4705.92	D
36.29	12.25	4.20	0.576	0.505	4705.92	D
36.29	12.25	2.41	0.331	0.229	4705.92	D
36.28	12.25	4.07	0.559	0.483	4705.92	D
36.21	12.25	2.47	0.341	0.237	4705.92	D
36.24	12.25	2.98	0.411	0.310	4705.92	D
36.26	12.25	1.15	0.158	0.080	4705.92	D
36.26	12.25	1.39	0.191	0.105	4705.92	D
36.28	12.25	0.90	0.123	0.056	4705.92	D
36.26	12.25	1.23	0.169	0.088	4705.92	D
36.18	12.16	4.49	0.620	0.555	4712.08	C
36.14	12.16	4.79	0.663	0.608	4712.08	C
36.11	12.16	5.45	0.755	0.731	4712.08	C
36.16	12.16	4.62	0.638	0.578	4712.08	C
36.18	12.16	5.91	0.816	0.820	4712.08	C
36.20	12.20	1.10	0.152	0.075	4713.00	C
36.22	12.20	2.11	0.291	0.189	4713.00	C
36.19	12.20	1.66	0.229	0.135	4713.00	C
36.23	12.20	3.15	0.434	0.335	4713.00	C
36.24	12.20	0.91	0.125	0.057	4713.00	C
36.22	12.20	1.36	0.187	0.101	4713.00	C
36.21	12.20	2.33	0.321	0.218	4713.00	C
36.19	12.20	2.17	0.300	0.197	4713.00	C
36.25	12.20	2.61	0.359	0.256	4715.25	A
36.21	12.20	2.17	0.299	0.197	4715.25	A
36.23	12.20	2.74	0.378	0.275	4715.25	A
36.23	12.20	4.18	0.576	0.501	4715.25	A
36.18	12.20	3.28	0.453	0.355	4715.25	A
36.24	12.20	3.36	0.463	0.367	4715.25	A
36.20	12.20	4.25	0.587	0.513	4715.25	A
36.16	12.20	4.54	0.628	0.564	4715.25	A
36.17	12.20	1.81	0.250	0.152	4718.42	A
36.21	12.20	1.85	0.255	0.157	4718.42	A
36.19	12.20	1.26	0.174	0.091	4718.42	A
36.21	12.20	3.23	0.446	0.347	4718.42	A
36.18	12.20	1.47	0.203	0.113	4718.42	A
36.22	12.20	1.11	0.153	0.076	4718.42	A
36.19	12.20	1.71	0.236	0.141	4718.42	A
36.17	12.20	2.68	0.371	0.266	4718.42	A
36.22	12.20	0.77	0.106	0.045	4720.33	A
36.24	12.20	1.17	0.161	0.082	4720.33	A
36.22	12.20	3.20	0.441	0.343	4720.33	A
36.24	12.20	2.78	0.383	0.281	4720.33	A
36.19	12.20	1.10	0.152	0.075	4720.33	A
36.23	12.20	0.61	0.084	0.032	4720.33	A
36.24	12.20	0.54	0.074	0.027	4720.33	A
36.23	12.20	1.48	0.204	0.114	4720.33	A
36.25	12.20	0.93	0.128	0.059	4720.33	A
36.16	12.20	3.16	0.437	0.337	4720.33	A
36.18	12.20	2.36	0.326	0.222	4720.33	A

### Champlin 369 Core Permeability Data

N2 Flow Press. (psia)	Atm Press. (psia)	Flow Rate (cc/min)	TEMCO Perm (mD)	Calc. Perm (mD)	Core Depth (ft)	Facies
36.13	12.15	2.95	0.408	0.305	4836.42	A
36.17	12.15	2.43	0.335	0.232	4836.42	A
36.19	12.15	3.29	0.454	0.356	4836.42	A
36.16	12.15	2.22	0.307	0.204	4836.42	A
36.19	12.15	1.86	0.257	0.158	4836.42	A
36.15	12.15	2.50	0.346	0.241	4836.42	A
36.17	12.15	5.13	0.708	0.671	4837.33	D
36.10	12.15	6.65	0.922	0.970	4837.33	D
36.14	12.15	10.03	1.389	1.741	4837.33	D
36.20	12.15	5.18	0.714	0.680	4837.33	D
36.20	12.15	6.92	0.954	1.027	4837.33	D
36.10	12.15	8.78	1.218	1.441	4837.33	D
36.15	12.15	8.07	1.116	1.278	4837.33	D
36.15	12.15	3.71	0.513	0.423	4837.33	D
36.24	12.23	0.61	0.083	0.032	4838.75	D
36.25	12.23	0.51	0.070	0.025	4838.75	D
36.24	12.23	0.53	0.073	0.027	4838.75	D
36.25	12.23	0.54	0.074	0.027	4838.75	D
36.23	12.23	0.74	0.101	0.043	4838.75	D
36.26	12.23	0.52	0.071	0.026	4838.75	D
36.23	12.23	2.43	0.334	0.232	4841.17	A
36.22	12.23	1.30	0.179	0.095	4841.17	A
36.20	12.23	3.16	0.435	0.337	4841.17	A
36.26	12.23	28.42	3.893	7.661	4841.17	C
36.20	12.23	11.75	1.616	2.181	4841.17	C
36.19	12.23	23.23	3.198	5.751	4841.17	C
36.27	12.23	30.97	4.245	8.658	4841.83	A
36.20	12.23	22.94	3.159	5.649	4841.83	A
36.20	12.23	41.66	5.737	13.201	4841.83	A
36.27	12.23	28.95	3.972	7.866	4841.83	A
36.24	12.23	11.99	1.647	2.244	4841.83	A
36.20	12.23	11.83	1.630	2.202	4841.83	A
36.25	12.23	8.13	1.117	1.291	4842.83	C
36.26	12.23	6.00	0.824	0.838	4842.83	C
36.21	12.23	9.45	1.301	1.600	4842.83	C
36.24	12.23	1.84	0.253	0.156	4842.83	D
36.24	12.23	1.93	0.265	0.167	4842.83	D
36.25	12.23	1.34	0.184	0.099	4842.83	D
36.18	12.23	5.76	0.795	0.791	4844.25	C
36.23	12.23	0.91	0.125	0.057	4844.25	C
36.19	12.23	13.47	1.858	2.648	4844.25	C
36.23	12.23	3.48	0.479	0.386	4846.33	C
36.23	12.23	2.21	0.304	0.202	4846.33	C
36.19	12.23	9.09	1.254	1.514	4846.33	C
36.20	12.23	3.65	0.503	0.413	4846.33	C
36.25	12.23	9.65	1.326	1.648	4847.50	D
36.25	12.23	26.30	3.615	6.861	4847.50	D
36.21	12.23	50.48	6.957	17.349	4847.50	D
36.21	12.23	1.51	0.208	0.118	4847.50	D
36.20	12.23	2.37	0.327	0.224	4847.50	D
36.24	12.23	3.19	0.439	0.341	4847.50	D
36.22	12.23	56.78	7.823	20.509	4848.17	A
36.19	12.23	37.67	5.199	11.440	4848.17	A
36.25	12.23	7.90	1.086	1.240	4848.17	A
36.24	12.23	3.34	0.460	0.364	4848.17	A
36.19	12.23	3.85	0.531	0.446	4848.17	A
36.26	12.23	34.73	4.774	10.191	4849.25	B
36.22	12.23	18.43	2.540	4.137	4849.25	B

N2 Flow Press. (psia)	Atm Press. (psia)	Flow Rate (cc/min)	TEMCO Perm (mD)	Calc. Perm (mD)	Core Depth (ft)	Facies
36.26	12.23	34.02	4.677	9.896	4849.25	B
36.22	12.23	3.78	0.521	0.434	4849.25	B
36.26	12.23	6.78	0.932	0.997	4849.25	B
36.25	12.23	6.31	0.867	0.900	4849.25	B
36.23	12.23	11.12	1.532	2.016	4854.25	C
36.25	12.23	6.24	0.859	0.886	4854.25	C
36.18	12.23	8.07	1.115	1.278	4854.25	C
36.26	12.23	3.24	0.445	0.349	4854.25	C
36.25	12.23	3.76	0.517	0.431	4854.25	C
36.27	12.23	15.91	2.186	3.356	4855.83	C
36.23	12.23	41.54	5.723	13.147	4855.83	C
36.23	12.23	43.59	6.005	14.080	4855.83	C
36.24	12.23	30.13	4.148	8.326	4855.83	C
36.19	12.23	28.87	3.987	7.835	4855.83	C
36.21	12.23	3.60	0.497	0.405	4856.67	A
36.27	12.23	0.83	0.114	0.050	4856.67	A
36.22	12.23	2.33	0.321	0.218	4856.67	A
36.25	12.23	2.76	0.380	0.278	4856.67	C
36.26	12.23	1.32	0.182	0.097	4856.67	C
36.23	12.23	2.33	0.321	0.218	4856.67	C
36.23	12.25	14.04	1.920	2.809	4857.75	C
36.27	12.25	4.01	0.548	0.472	4857.75	C
36.29	12.25	9.44	1.289	1.597	4857.75	C
36.24	12.25	11.04	1.513	1.996	4857.75	C
36.23	12.25	13.94	1.913	2.781	4857.75	C
36.29	12.25	7.22	0.988	1.091	4857.75	D
36.28	12.25	9.50	1.300	1.612	4857.75	D
36.27	12.25	4.84	0.663	0.617	4857.75	D
36.26	12.25	1.27	0.174	0.092	4859.33	B
36.26	12.25	2.63	0.361	0.259	4859.33	B
36.24	12.25	3.73	0.513	0.426	4859.33	B
36.25	12.25	4.90	0.673	0.628	4859.33	B
36.27	12.25	2.19	0.301	0.200	4861.00	A
36.24	12.25	3.04	0.418	0.319	4861.00	A
36.25	12.25	1.51	0.208	0.118	4861.00	A
36.25	12.25	79.98	10.998	33.390	4862.08	E
36.20	12.25	14.96	2.064	3.075	4862.08	E
36.23	12.25	40.11	5.524	12.508	4862.08	E
36.24	12.25	24.83	3.418	6.322	4862.08	E
36.30	12.25	6.98	0.957	1.039	4863.33	B
36.25	12.25	9.42	1.296	1.592	4863.33	B
36.26	12.25	7.90	1.086	1.240	4863.33	B
36.28	12.25	17.40	2.389	3.812	4863.33	E
36.23	12.25	18.56	2.556	4.179	4863.33	E
36.26	12.25	23.63	3.249	5.892	4863.33	E
36.24	12.25	52.68	7.253	18.434	4863.33	E
36.23	12.25	8.13	1.120	1.291	4864.67	C
36.25	12.25	12.28	1.690	2.322	4864.67	C
36.27	12.25	11.90	1.635	2.220	4864.67	C
36.23	12.25	9.01	1.241	1.495	4864.67	D
36.29	12.25	12.07	1.658	2.266	4864.67	D
36.28	12.25	11.87	1.630	2.212	4864.67	D
36.27	12.25	7.70	1.058	1.195	4864.67	D
36.23	12.25	44.80	6.172	14.639	4865.75	A
36.29	12.25	25.08	3.442	6.413	4865.75	A
36.27	12.25	16.85	2.316	3.642	4865.75	A
36.30	12.25	7.42	1.018	1.134	4865.75	A
36.27	12.25	7.66	1.053	1.186	4865.75	A
36.21	12.25	4.02	0.555	0.474	4865.75	A
36.29	12.25	14.37	1.972	2.904	4866.17	C
36.27	12.25	46.02	6.329	15.210	4866.17	C

N2 Flow Press. (psia)	Atm Press. (psia)	Flow Rate (cc/min)	TEMCO Perm (mD)	Calc. Perm (mD)	Core Depth (ft)	Facies
36.21	12.25	16.28	2.246	3.468	4866.17	C
36.23	12.25	14.54	2.003	2.953	4866.17	C
36.28	12.25	10.73	1.474	1.916	4866.17	C
36.21	12.25	61.68	8.509	23.072	4868.08	D
36.27	12.25	27.87	3.831	7.451	4868.08	D
36.29	12.25	12.63	1.734	2.417	4868.08	D
36.24	12.25	9.09	1.252	1.514	4868.08	D
36.26	12.25	11.67	1.605	2.160	4869.67	B
36.24	12.25	14.02	1.931	2.804	4869.67	B
36.27	12.25	12.06	1.658	2.263	4869.67	B
36.26	12.25	13.21	1.817	2.576	4869.67	B
36.27	12.25	8.63	1.186	1.406	4869.67	B
36.28	12.25	8.42	1.157	1.357	4869.67	B
36.25	12.25	48.33	6.652	16.307	4871.42	E
36.24	12.25	32.82	4.520	9.403	4871.42	E
36.27	12.25	48.59	6.679	16.432	4871.42	E
36.25	12.25	46.79	6.440	15.573	4871.42	E
36.30	12.25	28.09	3.854	7.535	4871.42	E
36.27	12.25	28.45	3.910	7.673	4873.92	A
36.27	12.25	27.60	3.791	7.349	4873.92	A
36.23	12.25	21.96	3.026	5.309	4873.92	A
36.27	12.25	4.59	0.631	0.573	4873.92	A
36.27	12.25	11.03	1.516	1.993	4873.92	A
36.23	12.25	68.88	9.491	26.996	4875.67	E
36.21	12.25	29.25	4.035	7.982	4875.67	E
36.29	12.25	16.52	2.268	3.541	4875.67	E
36.27	12.25	11.65	1.601	2.154	4875.67	E
36.28	12.25	20.70	2.843	4.881	4875.67	E
36.23	12.26	7.88	1.078	1.235	4876.17	B
36.30	12.26	12.72	1.735	2.441	4876.17	B
36.24	12.26	19.57	2.681	4.506	4876.17	E
36.26	12.26	36.67	5.021	11.010	4876.17	E
36.30	12.26	42.67	5.829	13.659	4876.17	E
36.28	12.26	50.28	6.881	17.251	4876.17	E
36.28	12.26	1.50	0.205	0.117	4877.92	C
36.24	12.26	1.83	0.251	0.155	4877.92	C
36.30	12.26	2.93	0.401	0.302	4877.92	C
36.29	12.26	4.45	0.609	0.548	4877.92	C
36.26	12.26	11.36	1.558	2.078	4877.92	C
36.26	12.26	11.63	1.596	2.149	4877.92	C
36.24	12.26	1.92	0.264	0.166	4878.83	E
36.25	12.26	3.16	0.434	0.337	4878.83	E
36.27	12.26	3.35	0.460	0.366	4878.83	E
36.27	12.26	5.96	0.818	0.830	4878.83	E
36.21	12.26	51.88	7.146	18.037	4880.17	A
36.28	12.26	52.08	7.143	18.136	4880.17	A
36.23	12.26	64.68	8.899	24.684	4880.17	A
36.29	12.26	1.08	0.148	0.073	4880.92	A
36.20	12.26	1.02	0.141	0.067	4880.92	A
36.25	12.26	1.47	0.202	0.113	4880.92	A
36.25	12.26	3.12	0.429	0.331	4880.92	A
36.27	12.26	2.62	0.360	0.258	4880.92	A
36.26	12.26	3.36	0.462	0.367	4880.92	A
36.24	12.26	5.86	0.806	0.810	4882.17	D
36.24	12.26	6.70	0.922	0.981	4882.17	D
36.30	12.26	6.49	0.890	0.937	4882.17	D
36.25	12.26	12.22	1.681	2.306	4882.17	D



### Sidwell Core Permeability Data

N2 Flow Press. (psia)	Atm Press. (psia)	Flow Rate (cc/min)	TEMCO Perm (mD)	Calc. Perm (mD)	Core Depth (ft)	Facies
36.15	12.20	50.88	6.98	20.16	4840.50	D
36.22	12.20	27.94	3.82	8.45	4840.50	D
36.22	12.20	43.06	5.89	15.82	4840.50	D
36.23	12.20	28.20	3.86	8.56	4840.50	D
36.21	12.20	42.02	5.76	15.27	4840.50	D
36.25	12.20	21.76	2.98	5.88	4840.50	D
36.21	12.20	2.86	0.39	0.31	4841.00	B
36.21	12.20	9.04	1.24	1.64	4841.00	B
36.24	12.20	5.42	0.74	0.78	4841.00	B
36.18	12.20	1.37	0.19	0.11	4841.50	D
36.22	12.20	2.55	0.35	0.26	4841.50	D
36.24	12.20	3.94	0.54	0.49	4841.50	D
36.16	12.20	4.60	0.63	0.62	4841.67	C
36.17	12.20	5.87	0.81	0.88	4841.67	C
36.18	12.20	7.54	1.04	1.26	4841.67	C
36.39	12.34	0.64	0.09	0.04	4842.83	B
36.31	12.34	0.93	0.13	0.06	4842.83	B
36.36	12.34	1.44	0.20	0.11	4842.83	B
36.35	12.34	0.64	0.09	0.04	4842.83	B
36.32	12.34	0.61	0.08	0.03	4842.83	B
36.34	12.34	1.43	0.19	0.11	4842.83	B
36.32	12.34	15.87	2.17	3.72	4844.00	D
36.32	12.34	72.68	9.94	33.82	4844.00	D
36.33	12.34	27.67	3.78	8.33	4844.00	D
36.34	12.34	2.19	0.30	0.21	4844.50	A
36.30	12.34	4.85	0.66	0.67	4844.50	A
36.37	12.34	3.18	0.43	0.36	4844.50	A
36.31	12.34	25.48	3.49	7.39	4844.50	C
36.32	12.34	14.93	2.04	3.40	4844.50	C
36.32	12.34	3.82	0.52	0.47	4844.50	C
36.35	12.34	1.08	0.15	0.08	4844.83	B
36.34	12.34	0.95	0.13	0.06	4844.83	B
36.36	12.34	1.11	0.15	0.08	4844.83	B
36.36	12.34	25.03	3.42	7.20	4845.00	D
36.34	12.34	38.80	5.31	13.60	4845.00	D
36.34	12.34	17.04	2.33	4.12	4845.00	D
36.32	12.34	0.71	0.10	0.04	4846.42	B
36.37	12.34	0.90	0.12	0.06	4846.42	B
36.38	12.34	1.40	0.19	0.11	4846.42	B
36.33	12.34	4.24	0.58	0.55	4846.42	B
36.37	12.34	5.16	0.71	0.73	4846.42	B
36.34	12.34	4.83	0.66	0.66	4846.42	B
36.38	12.34	1.81	0.25	0.16	4846.42	C
36.31	12.34	0.96	0.13	0.06	4846.42	C
36.33	12.34	3.39	0.46	0.40	4846.42	C
36.38	12.34	0.93	0.13	0.06	4848.08	D
36.32	12.34	0.75	0.10	0.04	4848.08	D
36.36	12.34	1.46	0.20	0.12	4848.08	D
36.38	12.34	0.83	0.11	0.05	4848.42	B
36.35	12.34	0.59	0.08	0.03	4848.42	B
36.30	12.31	2.63	0.36	0.27	4848.58	A
36.31	12.31	1.75	0.24	0.15	4848.58	A
36.31	12.31	1.67	0.23	0.14	4848.58	A
36.35	12.31	4.27	0.58	0.55	4848.58	A
36.34	12.31	1.16	0.16	0.08	4848.58	A
36.27	12.31	2.28	0.31	0.22	4848.58	A
36.36	12.31	14.49	1.97	3.26	4849.00	D
36.34	12.31	13.08	1.78	2.81	4849.00	D

N2 Flow Press. (psia)	Atm Press. (psia)	Flow Rate (cc/min)	TEMCO Perm (mD)	Calc. Perm (mD)	Core Depth (ft)	Facies
36.30	12.31	19.91	2.72	5.17	4849.00	D
36.31	12.31	2.87	0.39	0.31	4849.67	B
36.34	12.31	2.53	0.35	0.26	4849.67	B
36.29	12.31	2.38	0.33	0.24	4849.67	B
36.34	12.31	74.88	10.22	35.31	4849.83	D
36.33	12.31	49.09	6.71	19.13	4849.83	D
36.32	12.31	54.38	7.43	22.20	4849.83	D
36.31	12.31	5.63	0.77	0.83	4850.50	B
36.35	12.31	3.01	0.41	0.33	4850.50	B
36.34	12.31	2.15	0.29	0.20	4850.50	B
36.33	12.31	9.68	1.32	1.81	4851.00	B
36.34	12.31	10.87	1.49	2.15	4851.00	B
36.28	12.31	9.74	1.34	1.83	4851.00	B
36.31	12.31	4.74	0.65	0.64	4851.83	B
36.33	12.31	10.32	1.41	1.99	4851.83	B
36.34	12.31	18.69	2.56	4.71	4851.83	B
36.31	12.31	9.19	1.26	1.68	4851.83	B
36.32	12.31	13.97	1.91	3.09	4851.83	B
36.34	12.31	9.79	1.34	1.84	4851.83	B
36.28	12.31	11.66	1.60	2.38	4851.83	B
36.36	12.31	9.51	1.30	1.77	4851.83	B
36.30	12.31	9.06	1.24	1.65	4851.83	B
36.30	12.31	1.91	0.26	0.17	4853.00	A
36.32	12.31	5.71	0.78	0.84	4853.00	A
36.34	12.31	6.18	0.85	0.95	4853.00	A
36.31	12.31	2.01	0.28	0.19	4854.00	B
36.29	12.31	3.62	0.50	0.44	4854.00	B
36.31	12.31	8.71	1.19	1.56	4854.00	B
36.30	12.31	1.24	0.17	0.09	4854.08	A
36.32	12.31	3.69	0.51	0.45	4854.08	A
36.31	12.31	3.95	0.54	0.49	4854.08	A
36.31	12.28	0.66	0.09	0.04	4855.00	B
36.26	12.28	2.57	0.35	0.26	4855.00	B
36.26	12.28	4.49	0.61	0.59	4855.00	B
36.30	12.28	1.02	0.14	0.07	4855.08	C
36.28	12.28	3.94	0.54	0.49	4855.08	C
36.30	12.28	0.63	0.09	0.03	4855.75	B
36.31	12.28	1.26	0.17	0.09	4855.75	B
36.31	12.28	1.16	0.16	0.08	4855.75	B
36.32	12.28	26.63	3.63	7.88	4856.50	D
36.30	12.28	47.16	6.43	18.05	4856.50	D
36.31	12.28	51.33	7.00	20.41	4856.50	D
36.29	12.28	1.42	0.19	0.11	4857.08	B
36.28	12.28	1.95	0.27	0.18	4857.08	B
36.24	12.28	2.82	0.39	0.30	4857.08	B
36.28	12.28	0.72	0.10	0.04	4858.42	A
36.29	12.28	2.10	0.29	0.20	4858.42	A
36.23	12.28	1.42	0.20	0.11	4858.42	A
36.28	12.28	20.00	2.74	5.20	4858.83	D
36.29	12.28	53.48	7.32	21.67	4858.83	D
36.27	12.28	18.77	2.57	4.74	4858.83	D
36.28	12.28	4.41	0.60	0.58	4860.00	A
36.26	12.28	16.23	2.23	3.84	4860.00	A
36.33	12.28	3.41	0.47	0.40	4860.00	A
36.33	12.28	0.76	0.10	0.05	4861.58	B
36.33	12.28	1.98	0.27	0.18	4861.58	B
36.28	12.28	2.80	0.38	0.30	4861.83	B
36.25	12.28	6.79	0.93	1.08	4861.83	B
36.27	12.29	9.56	1.30	1.78	4862.75	B
36.29	12.29	10.87	1.48	2.15	4862.75	B
36.28	12.29	9.20	1.25	1.68	4862.75	B

N2 Flow Press. (psia)	Atm Press. (psia)	Flow Rate (cc/min)	TEMCO Perm (mD)	Calc. Perm (mD)	Core Depth (ft)	Facies
36.29	12.29	1.01	0.14	0.07	4864.33	A
36.26	12.29	2.67	0.37	0.28	4864.33	A
36.33	12.29	2.33	0.32	0.23	4864.33	A
36.25	12.29	2.33	0.32	0.23	4865.50	A
36.33	12.29	4.30	0.59	0.56	4865.50	A
36.29	12.29	1.41	0.19	0.11	4865.50	A
36.29	12.29	1.02	0.14	0.07	4866.00	B
36.28	12.29	0.65	0.09	0.04	4866.00	B
36.34	12.29	0.82	0.11	0.05	4866.00	B
36.30	12.29	2.78	0.38	0.30	4866.67	C
36.27	12.29	4.23	0.58	0.55	4866.67	C
36.29	12.29	3.79	0.52	0.47	4866.67	C
36.32	12.29	4.17	0.57	0.53	4866.67	C
36.33	12.29	4.58	0.63	0.61	4867.58	A
36.29	12.29	5.18	0.71	0.73	4867.58	A
36.34	12.29	5.24	0.72	0.74	4867.58	A
36.32	12.29	0.75	0.10	0.04	4868.08	A
36.28	12.29	2.13	0.29	0.20	4868.08	A
36.26	12.29	3.73	0.51	0.45	4868.08	A
36.24	12.27	53.68	7.32	21.78	4869.08	D
36.28	12.27	37.12	5.05	12.75	4869.08	D
36.27	12.27	53.98	7.35	21.96	4869.08	D
36.26	12.27	0.58	0.08	0.03	4870.08	A
36.23	12.27	1.10	0.15	0.08	4870.08	A
36.27	12.27	1.68	0.23	0.14	4870.08	A
36.25	12.27	4.92	0.67	0.68	4870.83	B
36.27	12.27	7.21	0.99	1.18	4870.83	B
36.28	12.27	7.35	1.00	1.22	4870.83	B
36.28	12.27	51.67	7.06	20.61	4870.92	C
36.32	12.27	33.54	4.58	11.01	4870.92	C
36.31	12.27	21.10	2.88	5.62	4870.92	C
36.27	12.27	13.94	1.91	3.08	4870.92	C
36.30	12.27	0.65	0.09	0.04	4872.08	A
36.27	12.27	1.70	0.23	0.15	4872.08	A
36.26	12.27	2.56	0.35	0.26	4872.08	A
36.26	12.27	6.29	0.86	0.97	4873.00	A
36.26	12.27	1.51	0.21	0.12	4873.08	A
36.28	12.27	3.76	0.51	0.46	4873.08	A
36.25	12.27	3.15	0.43	0.36	4873.08	A
36.27	12.27	4.15	0.57	0.53	4873.83	A
36.31	12.27	5.37	0.73	0.77	4873.83	A
36.26	12.27	13.84	1.90	3.05	4874.08	D
36.27	12.27	24.82	3.40	7.11	4874.08	D
36.24	12.27	45.41	6.24	17.09	4874.08	D
36.30	12.27	1.19	0.16	0.09	4875.42	A
36.31	12.27	4.24	0.58	0.55	4875.42	A
36.26	12.27	1.79	0.25	0.16	4875.42	A
36.29	12.27	9.05	1.24	1.65	4876.58	A
36.28	12.27	8.47	1.16	1.49	4876.58	A
36.26	12.27	7.57	1.04	1.27	4876.58	A
36.27	12.27	1.41	0.19	0.11	4878.00	A
36.26	12.27	0.67	0.09	0.04	4878.00	A
36.28	12.27	3.59	0.49	0.43	4878.00	A
36.28	12.27	7.09	0.97	1.15	4879.17	B
36.31	12.27	9.74	1.33	1.83	4879.17	B
36.30	12.27	11.89	1.63	2.44	4879.17	B
36.26	12.27	3.48	0.48	0.41	4879.42	A
36.26	12.27	4.54	0.62	0.60	4879.42	A
36.31	12.27	7.74	1.06	1.31	4879.42	A
36.28	12.27	17.66	2.42	4.34	4880.08	D
36.27	12.27	41.17	5.65	14.82	4880.92	D

N2 Flow Press. (psia)	Atm Press. (psia)	Flow Rate (cc/min)	TEMCO Perm (mD)	Calc. Perm (mD)	Core Depth (ft)	Facies
36.28	12.27	12.18	1.67	2.53	4880.92	D
36.25	12.27	3.76	0.52	0.46	4882.33	A
36.26	12.27	1.06	0.15	0.07	4882.33	A
36.29	12.27	0.99	0.14	0.07	4882.33	A
36.27	12.27	1.40	0.19	0.11	4882.75	B
36.25	12.27	2.16	0.30	0.21	4882.75	B
36.27	12.27	3.62	0.50	0.44	4882.75	B
36.24	12.20	0.67	0.09	0.04	4883.92	A
36.15	12.20	1.95	0.27	0.18	4883.92	A
36.24	12.20	3.65	0.50	0.44	4883.92	A
36.23	12.20	2.92	0.40	0.32	4884.50	A
36.23	12.20	4.53	0.62	0.60	4884.50	A
36.19	12.20	2.60	0.36	0.27	4884.50	A
36.18	12.20	4.25	0.58	0.55	4885.08	A
36.23	12.20	6.25	0.86	0.96	4885.08	A
36.19	12.20	5.38	0.74	0.77	4885.08	A
36.21	12.20	18.14	2.49	4.51	4885.67	D
36.22	12.20	16.27	2.23	3.85	4885.67	D
36.24	12.20	17.68	2.42	4.35	4885.67	D
36.20	12.20	9.73	1.34	1.83	4886.08	B
36.19	12.20	8.30	1.14	1.45	4886.08	B
36.19	12.20	4.32	0.59	0.56	4886.08	B
36.22	12.20	6.30	0.87	0.97	4887.25	C
36.19	12.20	9.42	1.30	1.74	4887.25	C
36.17	12.20	11.20	1.54	2.24	4887.25	C
36.23	12.20	2.56	0.35	0.26	4887.67	C
36.20	12.20	5.73	0.79	0.85	4887.67	C
36.26	12.28	4.67	0.64	0.63	4887.67	C
36.30	12.28	5.54	0.75	0.81	4887.67	C
36.30	12.28	9.69	1.32	1.82	4887.67	C
36.28	12.28	6.43	0.88	1.00	4888.17	B
36.24	12.28	7.89	1.08	1.35	4888.17	B
36.30	12.28	8.06	1.10	1.39	4888.17	B
36.26	12.28	8.20	1.12	1.43	4888.25	A
36.32	12.28	5.20	0.71	0.74	4888.25	A
36.28	12.28	3.18	0.43	0.36	4888.25	A
36.30	12.28	3.94	0.54	0.49	4888.50	C
36.29	12.28	5.56	0.76	0.81	4888.50	C
36.28	12.28	10.58	1.45	2.06	4889.42	A
36.28	12.28	23.22	3.18	6.46	4889.42	A
36.28	12.28	9.18	1.26	1.68	4889.42	A
36.27	12.28	3.85	0.53	0.48	4890.00	A
36.28	12.28	2.72	0.37	0.29	4890.00	A
36.27	12.28	4.65	0.64	0.63	4890.00	A
36.28	12.28	2.23	0.31	0.22	4890.58	A
36.26	12.28	1.16	0.16	0.08	4890.58	A
36.30	12.28	6.61	0.91	1.04	4890.58	A
36.27	12.28	1.76	0.24	0.15	4891.08	A
36.29	12.28	2.31	0.32	0.23	4891.08	A
36.30	12.28	3.95	0.54	0.49	4891.08	A

### Moser #1 Core Permeability Data

N2 Flow Press. (psia)	Atm Press. (psia)	Flow Rate (cc/min)	TEMCO Perm (mD)	Calc. Perm (mD)	Core Depth (ft)	Facies
36.23	12.20	2.98	0.410	0.310	4441.25	B
36.24	12.20	3.31	0.455	0.360	4441.25	B
36.24	12.20	2.75	0.378	0.276	4441.25	B
36.24	12.20	3.06	0.421	0.322	4441.25	B
36.23	12.20	2.13	0.293	0.192	4441.25	C
36.22	12.20	3.52	0.485	0.392	4441.25	C
36.24	12.20	2.66	0.366	0.263	4441.25	C
36.26	12.24	2.62	0.359	0.258	4442.33	D
36.25	12.24	3.08	0.423	0.325	4442.33	D
36.23	12.24	2.40	0.330	0.228	4442.33	D
36.26	12.24	2.83	0.388	0.288	4442.33	D
36.23	12.24	3.85	0.529	0.446	4442.33	D
36.23	12.24	3.17	0.434	0.338	4446.25	C
36.27	12.24	2.35	0.321	0.221	4446.25	C
36.20	12.24	1.83	0.251	0.155	4446.25	C
36.22	12.24	3.78	0.519	0.434	4446.25	C
36.24	12.24	1.98	0.272	0.173	4446.25	C
36.26	12.24	4.64	0.636	0.581	4446.25	C
36.27	12.24	1.57	0.215	0.124	4447.00	A
36.26	12.24	1.32	0.181	0.097	4447.00	A
36.23	12.24	2.64	0.363	0.261	4447.00	A
36.29	12.24	2.04	0.280	0.181	4447.00	A
36.25	12.24	2.30	0.316	0.214	4447.00	A
36.20	12.24	0.88	0.121	0.055	4447.00	A
36.21	12.24	3.11	0.429	0.329	4447.00	A
36.23	12.24	2.48	0.342	0.238	4448.00	A
36.19	12.24	2.30	0.318	0.214	4448.00	A
36.22	12.18	1.04	0.143	0.069	4448.00	A
36.18	12.18	1.53	0.211	0.120	4448.00	A
36.23	12.18	0.52	0.071	0.026	4448.00	A
36.19	12.18	0.56	0.077	0.029	4448.00	A
36.22	12.18	1.51	0.208	0.118	4448.00	A
36.23	12.18	2.49	0.342	0.240	4448.00	A
36.21	12.18	3.31	0.455	0.360	4449.08	D
36.18	12.18	1.18	0.163	0.083	4449.08	D
36.15	12.18	2.45	0.339	0.234	4449.08	D
36.21	12.18	3.71	0.511	0.423	4449.08	D
36.19	12.18	3.08	0.425	0.325	4449.08	D
36.17	12.18	5.33	0.736	0.708	4450.67	D
36.16	12.18	5.21	0.720	0.686	4450.67	D
36.20	12.18	4.50	0.620	0.557	4450.67	D
36.19	12.18	6.06	0.836	0.850	4450.67	D
36.17	12.18	6.85	0.946	1.012	4450.67	D
36.21	12.18	4.73	0.652	0.598	4450.67	D
36.19	12.18	4.73	0.653	0.598	4450.67	D
36.17	12.18	5.11	0.706	0.667	4450.67	D
36.22	12.18	3.66	0.504	0.415	4451.67	D
36.14	12.18	5.23	0.724	0.689	4451.67	D
36.18	12.18	3.68	0.508	0.418	4451.67	D
36.19	12.18	2.74	0.378	0.275	4451.67	D
36.17	12.18	2.91	0.402	0.299	4453.67	B
36.16	12.18	3.79	0.524	0.436	4453.67	B
36.20	12.18	3.06	0.422	0.322	4453.67	B
36.22	12.18	1.99	0.274	0.174	4453.67	B
36.20	12.18	1.62	0.223	0.130	4453.67	D
36.21	12.18	0.61	0.084	0.032	4453.67	D
36.13	12.18	2.26	0.313	0.209	4453.67	D
36.22	12.18	2.23	0.307	0.205	4453.67	D

N2 Flow Press. (psia)	Atm Press. (psia)	Flow Rate (cc/min)	TEMCO Perm (mD)	Calc. Perm (mD)	Core Depth (ft)	Facies
36.19	12.16	3.67	0.503	0.416	4454.67	A
36.17	12.16	2.43	0.334	0.232	4454.67	A
36.14	12.16	5.14	0.706	0.673	4454.67	C
36.19	12.16	4.47	0.613	0.551	4454.67	C
36.21	12.16	1.63	0.223	0.131	4454.67	D
36.20	12.16	2.44	0.334	0.233	4454.67	D
36.16	12.16	0.73	0.100	0.042	4457.00	A
36.15	12.16	1.01	0.139	0.066	4457.00	A
36.16	12.16	0.83	0.114	0.050	4457.00	A
36.19	12.16	1.62	0.223	0.130	4457.00	A
36.14	12.16	0.90	0.124	0.056	4457.00	A
36.15	12.16	1.27	0.175	0.092	4457.00	A
36.17	12.16	1.83	0.252	0.155	4457.00	A
36.16	12.16	1.67	0.230	0.136	4457.00	A
36.18	12.16	1.14	0.157	0.079	4460.00	A
36.18	12.16	5.80	0.800	0.799	4460.00	A
36.15	12.16	5.22	0.721	0.687	4460.00	A
36.19	12.16	4.14	0.571	0.494	4460.00	A
36.16	12.16	2.86	0.395	0.292	4460.00	A
36.16	12.16	4.60	0.635	0.574	4460.00	A
36.20	12.16	2.87	0.395	0.294	4460.00	A
36.17	12.16	2.48	0.342	0.238	4460.00	A
36.16	12.16	1.24	0.171	0.089	4462.50	A
36.18	12.16	2.56	0.353	0.249	4462.50	A
36.19	12.16	1.04	0.143	0.069	4462.50	A
36.20	12.16	0.55	0.076	0.028	4462.50	A
36.12	12.16	1.90	0.263	0.163	4462.50	A
36.16	12.16	1.02	0.141	0.067	4462.50	A
36.15	12.16	3.13	0.433	0.332	4462.50	A
36.14	12.16	4.90	0.678	0.628	4462.50	A
36.16	12.16	0.93	0.129	0.059	4462.50	A
36.15	12.16	3.18	0.439	0.340	4465.00	A
36.20	12.16	5.75	0.791	0.789	4465.00	A
36.19	12.16	2.80	0.386	0.283	4465.00	A
36.18	12.16	5.03	0.693	0.652	4465.00	A
36.10	12.16	6.75	0.935	0.991	4465.00	A
36.17	12.16	2.81	0.387	0.285	4465.00	A
36.16	12.16	2.38	0.328	0.225	4465.00	A
36.18	12.16	5.09	0.702	0.663	4465.00	A
36.21	12.16	6.69	0.921	0.979	4465.00	A
36.13	12.16	7.01	0.970	1.046	4465.00	A
36.16	12.16	3.36	0.464	0.367	4466.83	A
36.16	12.16	2.62	0.362	0.258	4466.83	A
36.17	12.16	3.16	0.436	0.337	4466.83	A
36.20	12.16	2.78	0.383	0.281	4466.83	A
36.18	12.16	1.38	0.190	0.104	4468.00	A
36.18	12.16	2.74	0.378	0.275	4468.00	A
36.15	12.16	2.76	0.382	0.278	4468.00	A
36.16	12.16	5.56	0.768	0.752	4468.00	A
36.20	12.20	1.31	0.179	0.096	4468.75	A
36.19	12.20	2.65	0.364	0.262	4468.75	A
36.22	12.20	3.50	0.480	0.389	4468.75	A
36.15	12.20	5.43	0.748	0.727	4468.75	A
36.24	12.20	0.74	0.101	0.043	4469.58	A
36.16	12.20	1.08	0.149	0.073	4469.58	A
36.21	12.20	1.50	0.206	0.117	4469.58	A
36.23	12.20	2.39	0.328	0.226	4469.58	A
36.21	12.20	1.21	0.166	0.086	4471.25	A
36.22	12.20	1.48	0.203	0.114	4471.25	A
36.22	12.20	1.18	0.162	0.083	4471.25	A
36.23	12.20	1.91	0.262	0.164	4471.25	A

N2 Flow Press. (psia)	Atm Press. (psia)	Flow Rate (cc/min)	TEMCO Perm (mD)	Calc. Perm (mD)	Core Depth (ft)	Facies
36.23	12.20	1.70	0.234	0.139	4472.08	A
36.16	12.20	1.84	0.254	0.156	4472.08	A
36.19	12.20	1.70	0.234	0.139	4472.08	A
36.20	12.20	2.02	0.278	0.178	4472.08	A
36.20	12.20	4.00	0.551	0.471	4472.92	A
36.15	12.20	10.19	1.409	1.781	4472.92	A
36.24	12.20	2.05	0.282	0.182	4472.92	A
36.19	12.20	2.74	0.378	0.275	4472.92	A
36.23	12.20	2.69	0.370	0.268	4472.92	A
36.16	12.20	4.28	0.591	0.518	4472.92	A
36.18	12.20	2.34	0.323	0.220	4472.92	A
36.18	12.20	4.76	0.657	0.603	4474.67	A
36.15	12.20	7.10	0.982	1.065	4474.67	A
36.24	12.20	12.39	1.703	2.352	4474.67	A
36.16	12.20	8.64	1.194	1.408	4474.67	A
36.24	12.20	7.78	1.070	1.213	4474.67	A
36.22	12.20	4.89	0.673	0.626	4474.67	A
36.22	12.25	0.88	0.121	0.055	4476.17	A
36.26	12.25	2.76	0.378	0.278	4476.17	A
36.28	12.25	1.67	0.228	0.136	4476.17	A
36.28	12.25	7.14	0.976	1.073	4476.92	A
36.26	12.25	10.32	1.414	1.813	4476.92	A
36.25	12.25	4.43	0.607	0.544	4476.92	A
36.28	12.25	5.62	0.769	0.764	4476.92	A
36.23	12.25	6.97	0.957	1.037	4477.17	A
36.25	12.25	10.62	1.457	1.888	4477.17	A
36.20	12.25	14.11	1.942	2.829	4477.17	A
36.22	12.25	4.16	0.572	0.498	4478.42	A
35.25	12.25	3.52	0.515	0.392	4478.42	A
35.27	12.25	2.42	0.354	0.230	4478.42	A
36.21	12.25	5.19	0.714	0.682	4478.42	D
36.21	12.25	3.32	0.457	0.361	4478.42	D
36.23	12.25	6.24	0.858	0.886	4479.33	A
36.24	12.25	6.98	0.959	1.039	4479.33	A
36.29	12.25	5.50	0.754	0.741	4479.33	A
35.25	12.25	9.92	1.451	1.714	4479.33	D
36.27	12.25	4.95	0.679	0.637	4479.33	D
36.20	12.25	2.81	0.387	0.285	4479.33	D
36.20	12.25	2.17	0.299	0.197	4479.83	A
36.25	12.25	4.74	0.651	0.599	4479.83	A
36.28	12.25	1.09	0.150	0.074	4479.83	A
36.22	12.25	4.55	0.627	0.565	4479.83	A
36.22	12.25	5.67	0.781	0.773	4479.83	A
36.24	12.25	9.69	1.333	1.658	4479.83	A
36.27	12.25	9.59	1.317	1.633	4479.83	A
36.22	12.25	8.79	1.211	1.443	4480.83	A
36.27	12.25	3.89	0.534	0.452	4480.83	A
36.23	12.25	7.16	0.986	1.078	4480.83	D
36.27	12.25	6.63	0.911	0.966	4480.83	D
36.30	12.25	2.23	0.306	0.205	4480.83	D
36.24	12.25	2.54	0.350	0.247	4481.92	A
36.25	12.25	4.45	0.612	0.548	4481.92	A
36.23	12.25	3.74	0.515	0.428	4481.92	A
36.21	12.25	13.55	1.869	2.671	4481.92	A
36.25	12.25	5.32	0.732	0.706	4481.92	A
36.20	12.25	5.07	0.700	0.660	4481.92	A
36.21	12.25	11.70	1.614	2.167	4481.92	A
36.22	12.25	7.67	1.057	1.189	4483.17	A
36.22	12.25	1.81	0.250	0.152	4483.17	A
36.20	12.25	4.27	0.589	0.517	4483.17	A
36.29	12.25	2.21	0.303	0.202	4483.17	A

<b>N2 Flow Press. (psia)</b>	<b>Atm Press. (psia)</b>	<b>Flow Rate (cc/min)</b>	<b>TEMCO Perm (mD)</b>	<b>Calc. Perm (mD)</b>	<b>Core Depth (ft)</b>	<b>Facies</b>
36.23	12.25	6.02	0.829	0.842	4483.17	A
36.27	12.20	0.76	0.104	0.044	4483.92	A
36.21	12.20	1.79	0.245	0.150	4483.92	A
36.22	12.20	0.95	0.130	0.061	4483.92	A
36.17	12.20	3.72	0.512	0.425	4483.92	A
36.24	12.20	4.88	0.668	0.625	4483.92	A
36.23	12.20	3.61	0.495	0.407	4483.92	A
36.18	12.20	1.52	0.209	0.119	4484.75	A
36.20	12.20	3.16	0.434	0.337	4484.75	A
36.22	12.20	1.41	0.194	0.107	4484.75	A
36.23	12.20	2.42	0.332	0.230	4484.75	A
36.16	12.20	3.33	0.459	0.363	4484.75	A
36.18	12.20	7.94	1.094	1.249	4484.75	A
36.19	12.20	2.36	0.325	0.222	4485.58	A
36.17	12.20	5.51	0.760	0.742	4485.58	A
36.17	12.20	9.24	1.274	1.549	4485.58	A
36.19	12.20	4.96	0.683	0.639	4485.58	A
36.21	12.20	2.32	0.319	0.217	4485.58	D
36.16	12.20	2.85	0.393	0.291	4486.75	A
36.21	12.20	8.63	1.188	1.406	4486.75	A
36.22	12.20	8.25	1.135	1.319	4486.75	A
36.18	12.20	6.42	0.885	0.923	4486.75	A
36.16	12.20	6.55	0.904	0.950	4487.08	A
36.18	12.20	4.75	0.655	0.601	4487.08	A
36.21	12.20	2.23	0.307	0.205	4487.08	A
36.23	12.20	3.63	0.499	0.410	4487.08	D
36.24	12.20	2.89	0.397	0.296	4488.08	A
36.17	12.20	2.34	0.323	0.220	4488.08	A
36.17	12.20	4.47	0.617	0.551	4488.08	A
36.20	12.20	3.35	0.462	0.366	4488.08	A



## **Appendix C**

Near-wellbore Modeling and Upscaling Results

### ***Facies Modeling***

The near-wellbore facies modeling for the McHale #1 and Champlin 369 cores was done by compiling the four defined facies into a 3-D representation of the formations respective cores. To start, a generic facies model of each of the four facies was modeled for both formations, generating four generic facies for each formation. A generic facies model for this research is defined as a gross representation of an observed facies that is used as the base for populating a 3-D core model. Each facies is customized as it is used in the 3-D core model to match the observed and measured characteristics of the facies at a given depth (Figure 31). Multiple variations of each facies were designed and modeled to give greater flexibility in the specific modeling of specific facies. Additionally, the generic variations that are designed early save time when modeling specific facies in the cores as less variables have to be changed later. These different variations are all of the same basic design and use the same depositional processes. Only minor variables within each facies were changed (e.g. increased or decreased mudrock content, higher ripple amplitude or wavelength, thickness of mudrock or sandstone laminas, etc.) In this study, these generic facies models are known as sub-models.

Once the generic sub-models were completed, detailed core photographs were taken and loaded into the modeling software. The photographs were taken at a foot interval with each photo only representing a one foot section of the core. The photos were cropped and straightened so that only the core face is seen. Each was carefully depth calibrated so that it would display at the depths marked on the core. These photographs are the primary guide for determining the facies at a given depth. Core descriptions were not detailed enough to provide every facies within in the core as the majority of them are at most several inches thick (Appendix A). However, the cores were on hand during the modeling process so direct measurements could be taken from the core as needed (facies thickness, ripple amplitude, wavy lamina wavelengths, etc.).


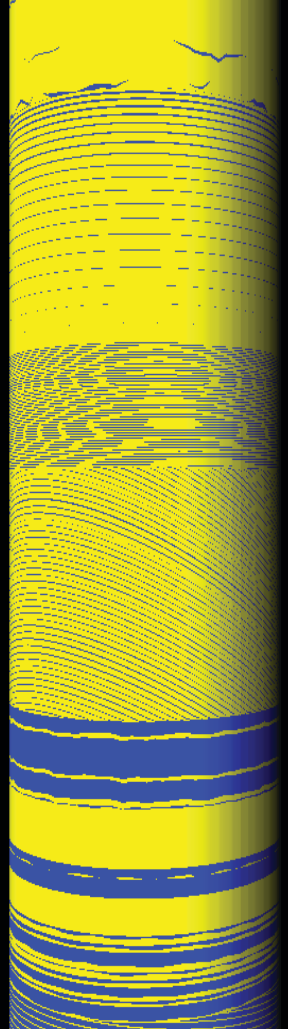
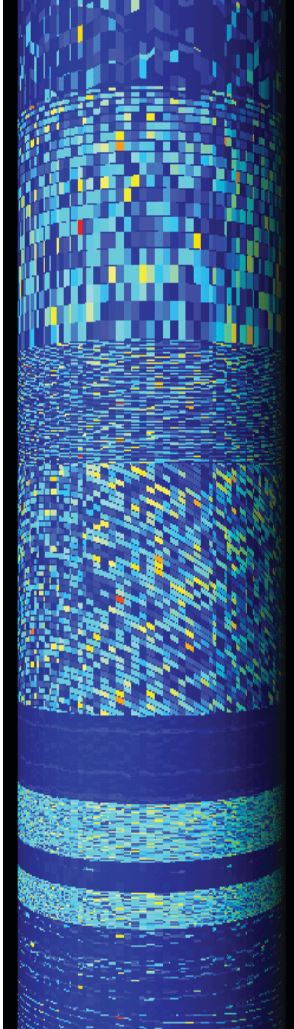
Core Photograph	3-D Bedding Structure Model	3-D Original Permeability Distribution Model	Effective Permeability (mD)
			0.116
			0.604
			0.471
			0.510
			0.037
			1.47
			0.009
			1.47
0.061			

Figure 31. Schematic showing core photograph of McHale #1 core (~4705'-4706') and the corresponding near-wellbore models. The left-middle column shows the facies model as it corresponds to the photograph (known as bedding structure model); right-middle column shows original permeability distribution in the near-wellbore model. The permeability model is upscaled to generate a single effective-permeability value for each facies modeled (right column).

Core photos were displayed along with all well-log data available for each core and each facies was hand drawn on top of them. This was used particularly with the core photos as the well-log suites have a much coarser resolution and do not differentiate facies at that scale. As the boundaries for each facies were designated, each was populated with one of the generic sub-models created earlier. This was done one facies occurrence at a time. As each facies occurrence was populated, the model facies was rendered and compared to the core photographs and the actual core. Adjustments were made and the facies was regenerated and compared again for photographs and the actual core. This process was continued until the modeled 3-D core matched what was observed in the core photographs and actual core. Following this, the next set of facies boundaries were created and the process was repeated throughout the entire cored interval for the McHale #1 and Champlin 369 cores.

### ***Permeability Modeling***

Once the facies models were completed, permeability models were created (Figure 31). The mini-permeameter data measurements were collected by lamina type for each compiled and a mean and standard deviation were determined for each sandstone lamina in each facies. The mean for the permeability data was determined using a geometric average of calibrated permeability measurements. Similarly, the standard deviation was derived from the calibrated measurements as well. The inputs for the model were done by lamina type within each facies (e.g. sandstone or mudrock), and for simplicity it was assumed there was only one type of sandstone and one type of mudrock for each facies. Due to the small-scale nature of the measurements and irregular spacing of the measurements, variograms could not be used. A minimum permeability of 0.0001 mD was applied along with a maximum permeability of 15.0 mD. If any values were modeled as being outside of these values, they were rounded to the minimum or maximum values depending on whether the value was higher or lower than each.

### ***Permeability Upscaling and Results***

Once the permeability models were created, an upscaling case was defined. The upscaling process used in this study is a flow-based algorithm that simulates flow through each facies and determines the effective permeability. The size of each block upscaled is determined by the facies boundaries defined previously. This was preferred over the alternative, which would be defining an upscaling block size. That would cause multiple facies with different permeability values to be lumped together with effective values generated no longer corresponding to a single facies. This would make comparison of original- to effective-permeability values difficult. With the upscaling boundaries being the same the facies boundaries, each facies is given an effective value and a comparison of that facies original permeability and the resulting effective permeability could be completed.

Choosing the type of upscaling process, either single-phase or multi-phase upscaling is important. This study uses a single-phase upscaling process. Single phase was chosen instead of a multi-phase upscaling because of the lack of data required for multi-phase upscaling. Multi-phase upscaling is typically done for two fluids, water and oil. To do this type of upscaling, more data is required including fluid viscosity and saturation functions for each lamina.

After determining what type of upscaling will be done, determining the boundary conditions is next. The boundary conditions that are chosen for the upscaling process can be considered one of the more important variables. This study uses what are known as periodic boundary conditions (PBC) due to its effectiveness in producing accurate results in heterogeneous reservoirs. Pickup et al. (1994) showed that PBC proved to be robust in evaluating permeabilities in the x- and y-directions. Additionally, this method was determined to be very effective at handling complex geometries and in the context of a small-scale model like this; PBC creates symmetric effective permeabilities (Durlofsky, 1991). Periodic boundary conditions are best applied to reservoirs that are heterogeneous and contain repeating

geological structures. The Terry and Hygiene formations at these locations are heterogeneous but also contain a stacking pattern among the four facies. The three sandstone-rich facies occur together with regular frequency and the sandstone-poor wavy-laminated facies occurring with ripple-laminated facies regularly as well. While this pattern isn't absolute, enough of a pattern exists to further warrant using this set of boundary conditions. The periodic boundary conditions used produces a pressure gradient and there is no limitation to flow through any bounding surface (Figure 32). The results of the upscaling are presented for both the McHale #1 and Champlin 369 cores in summary in Tables 1 and 3 and in detail for each facies in Tables 4 and 5.

A comparison of the original-permeability values and effective-permeability values was conducted by facies as well. Similar to the overall trend for the cores as a whole (Figure 8), each individual facies shows a reduction in the range of effective permeabilities relative to original permeabilities, with the exception of facies D, the structures sandstone (Figures 33, 34, 35, 36). This facies was least affected by the upscaling due to its lack of mudrock. This causes the effective permeability to be almost the same as the original permeability after the upscaling is completed.

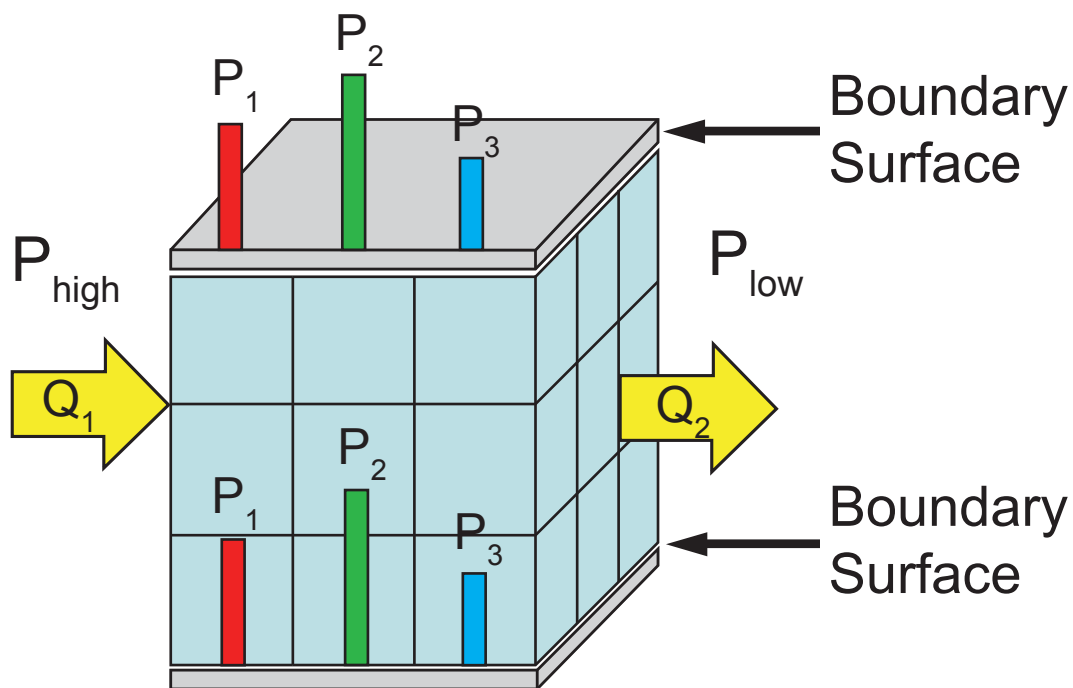


Figure 32. Schematic of flow-based upscaling boundary conditions. No limitations in flow occur across boundary conditions. This set of boundary conditions is ideally suited for heterogeneous samples. Effective permeabilities using these boundary condition parameters are measured in six directions. Modified from SBED Users Manual v4.1.

Original Permeability (mD)			Effective Permeability (mD)		
Sand lamina Avg.	Sand Lamina Std. Dev.	Mud Lamina Avg. *	Geometric Avg.	Arithmetic Avg.	Standard Dev.
1.50	6.17	0.004	0.24	0.28	0.16
3.08	3.93	0.004	0.21	0.53	0.60
5.29	8.26	0.004	3.55	3.56	0.26
0.73	2.27	N/A	0.34	0.37	0.22

Table 3. Original- and effective-permeability values for Champlin 369 core.



### McHale #1 Upscaling Results

Facies	Effective Perm (mD)	Top (ft)	Bottom (ft)	Thickness (ft)
A	0.10	4688.00	4688.41	0.41
B	0.53	4688.41	4688.57	0.16
A	0.08	4688.57	4689.13	0.56
D	0.21	4689.13	4689.51	0.38
B	0.42	4689.51	4689.60	0.09
A	0.14	4689.60	4689.94	0.34
D	0.21	4689.94	4690.23	0.29
A	0.16	4690.23	4690.31	0.08
D	0.21	4690.31	4690.37	0.06
A	0.17	4690.37	4690.51	0.14
A	0.21	4690.51	4690.62	0.11
A	0.16	4690.62	4691.05	0.43
B	0.52	4691.05	4691.10	0.05
A	0.17	4691.10	4691.38	0.28
C	1.46	4691.38	4691.56	0.18
A	0.18	4691.56	4691.77	0.21
B	0.56	4691.77	4692.07	0.30
D	0.21	4692.07	4692.19	0.12
A	0.18	4692.19	4692.33	0.14
B	0.49	4692.33	4692.45	0.12
B	0.43	4692.45	4692.70	0.25
A	0.13	4692.70	4693.02	0.32
A	0.13	4693.02	4693.17	0.15
D	0.21	4693.17	4693.38	0.21
C	1.45	4693.38	4693.59	0.21
A	0.13	4693.59	4693.74	0.15
C	1.46	4693.74	4693.85	0.11
A	0.09	4693.85	4693.94	0.09
D	0.22	4693.94	4694.46	0.52
A	0.20	4694.46	4694.65	0.19
C	1.47	4694.65	4694.73	0.08
A	0.10	4694.73	4694.91	0.18
C	1.46	4694.91	4695.05	0.14
A	0.18	4695.05	4695.14	0.09
D	0.21	4695.14	4695.50	0.36
B	0.43	4695.50	4695.58	0.08
A	0.05	4695.58	4695.70	0.12
C	1.46	4695.70	4695.81	0.11
A	0.05	4695.81	4695.88	0.07
A	0.17	4695.88	4696.51	0.63
B	0.46	4696.51	4696.63	0.12
C	1.47	4696.63	4696.69	0.06
B	0.61	4696.69	4696.79	0.10
B	0.36	4696.79	4697.02	0.23
A	0.06	4697.02	4697.24	0.22
B	0.55	4697.24	4697.32	0.08
B	0.42	4697.32	4697.52	0.20
D	0.21	4697.52	4697.59	0.07
B	0.29	4697.59	4697.68	0.09
B	0.38	4697.68	4697.74	0.06
B	0.70	4697.74	4697.89	0.15
D	0.22	4697.89	4697.93	0.04
B	0.61	4697.93	4698.01	0.08
D	0.22	4698.01	4698.06	0.05
A	0.01	4698.06	4698.17	0.11

<b>Facies</b>	<b>Effective Perm (mD)</b>	<b>Top (ft)</b>	<b>Bottom (ft)</b>	<b>Thickness (ft)</b>
D	0.21	4698.17	4698.22	0.05
A	0.13	4698.22	4698.72	0.50
D	0.2137	4698.72	4698.84	0.12
A	0.07	4698.84	4698.95	0.11
D	0.21	4698.95	4699.08	0.13
B	0.43	4699.08	4699.13	0.05
A	0.10	4699.13	4699.25	0.12
B	0.60	4699.25	4699.52	0.27
A	0.03	4699.52	4699.63	0.11
C	1.46	4699.63	4699.72	0.09
A	0.00	4699.72	4699.79	0.07
C	1.47	4699.79	4699.83	0.04
A	0.02	4699.83	4700.18	0.35
D	0.20	4700.18	4700.26	0.08
B	0.16	4700.26	4700.33	0.07
D	0.17	4700.33	4700.66	0.33
A	0.02	4700.66	4700.92	0.26
B	0.50	4700.92	4701.08	0.16
A	0.14	4701.08	4701.21	0.13
D	0.21	4701.21	4701.25	0.04
A	0.06	4701.25	4701.61	0.36
D	0.21	4701.61	4701.70	0.09
A	0.08	4701.70	4701.75	0.05
B	0.58	4701.75	4701.93	0.18
B	0.25	4701.93	4702.10	0.17
A	0.01	4702.10	4702.21	0.11
D	0.21	4702.21	4702.30	0.09
A	0.14	4702.30	4702.58	0.28
D	0.21	4702.58	4702.69	0.11
B	0.31	4702.69	4702.82	0.13
A	0.04	4702.82	4702.91	0.09
D	0.21	4702.91	4702.97	0.06
A	0.02	4702.97	4703.10	0.13
A	0.11	4703.10	4703.23	0.13
D	0.21	4703.23	4703.26	0.03
A	0.12	4703.26	4703.44	0.18
B	0.38	4703.44	4703.64	0.20
B	0.59	4703.64	4703.93	0.29
B	0.45	4703.93	4704.04	0.11
B	0.31	4704.04	4704.28	0.24
A	0.00	4704.28	4704.31	0.03
D	0.20	4704.31	4704.37	0.06
B	0.30	4704.37	4704.62	0.25
B	0.30	4704.62	4704.81	0.19
A	0.19	4704.81	4705.07	0.26
A	0.12	4705.07	4705.23	0.16
B	0.60	4705.23	4705.44	0.21
B	0.47	4705.44	4705.54	0.10
B	0.51	4705.54	4705.76	0.22
A	0.04	4705.76	4705.83	0.07
C	1.47	4705.83	4705.88	0.05
A	0.01	4705.88	4705.91	0.03
C	1.47	4705.91	4705.94	0.03
A	0.06	4705.94	4706.01	0.07
B	0.11	4706.01	4706.17	0.16
C	1.47	4706.17	4706.23	0.06
A	0.07	4706.23	4706.26	0.03

<b>Facies</b>	<b>Effective Perm (mD)</b>	<b>Top (ft)</b>	<b>Bottom (ft)</b>	<b>Thickness (ft)</b>
D	0.22	4706.26	4706.34	0.08
B	0.68	4706.34	4706.60	0.26
D	0.21	4706.60	4707.17	0.57
B	0.68	4707.17	4707.35	0.18
A	0.08	4707.35	4708.23	0.88
B	0.55	4708.23	4708.33	0.10
D	0.21	4708.33	4708.46	0.13
B	0.61	4708.46	4708.79	0.33
A	0.07	4708.79	4709.15	0.36
D	0.21	4709.15	4709.44	0.29
A	0.12	4709.44	4709.54	0.10
A	0.05	4709.54	4709.64	0.10
B	0.57	4709.64	4709.68	0.04
C	1.47	4709.68	4709.73	0.05
A	0.17	4709.73	4709.79	0.06
C	1.46	4709.79	4709.92	0.13
A	0.03	4709.92	4710.19	0.27
B	0.29	4710.19	4710.28	0.09
D	0.21	4710.28	4710.51	0.23
B	0.32	4710.51	4710.59	0.08
D	0.21	4710.59	4710.67	0.08
A	0.03	4710.67	4710.71	0.04
D	0.21	4710.71	4710.80	0.09
B	0.51	4710.80	4710.96	0.16
B	0.63	4710.96	4711.00	0.04
B	0.60	4711.00	4711.05	0.05
B	0.51	4711.05	4711.07	0.02
A	0.04	4711.07	4711.24	0.17
D	0.21	4711.24	4711.78	0.54
A	0.08	4711.78	4712.00	0.22
A	0.10	4712.00	4712.14	0.14
A	0.06	4712.14	4712.22	0.08
A	0.18	4712.22	4712.36	0.14
A	0.04	4712.36	4712.84	0.48
D	0.21	4712.84	4713.18	0.34
A	0.10	4713.18	4713.70	0.52
A	0.17	4713.70	4713.88	0.18
B	0.43	4713.88	4714.00	0.12
A	0.10	4714.00	4714.20	0.20
A	0.11	4714.20	4714.36	0.16
A	0.17	4714.36	4714.58	0.22
A	0.05	4714.58	4714.75	0.17
A	0.10	4714.75	4714.99	0.24
D	0.21	4714.99	4715.04	0.05

Table 4. Upscaled results from McHale #1 core. (N=156)

### Champlin 369 Upscaling Results

<b>Facies</b>	<b>Effective Perm (mD)</b>	<b>Top (ft)</b>	<b>Bottom (ft)</b>	<b>Thickness (ft)</b>
A	0.45	4836.25	4836.88	0.63
B	0.05	4836.88	4838.06	1.18
B	1.30	4838.06	4838.14	0.08
B	0.05	4838.14	4839.05	0.91
C	3.42	4839.05	4839.29	0.24
B	0.07	4839.29	4839.71	0.42
B	0.07	4839.71	4839.93	0.22
A	0.39	4839.93	4839.99	0.06
A	0.50	4839.99	4840.57	0.58
B	0.04	4840.57	4841.05	0.48
A	0.25	4841.05	4841.21	0.16
A	0.41	4841.21	4842.04	0.83
C	3.61	4842.04	4842.19	0.15
B	0.08	4842.19	4842.71	0.52
A	0.17	4842.71	4842.86	0.15
B	0.09	4842.86	4843.00	0.14
A	0.30	4843.00	4843.26	0.26
B	1.73	4843.26	4843.58	0.32
A	0.05	4843.58	4843.69	0.11
D	0.31	4843.69	4843.80	0.11
A	0.36	4843.80	4844.12	0.32
A	0.29	4844.12	4844.58	0.46
A	0.62	4844.58	4845.15	0.57
A	0.34	4845.15	4845.36	0.21
D	0.33	4845.36	4845.53	0.17
B	0.01	4845.53	4845.62	0.09
A	0.46	4845.62	4846.04	0.42
B	0.11	4846.04	4846.13	0.09
A	0.23	4846.13	4846.39	0.26
A	0.07	4846.39	4846.69	0.30
C	3.71	4846.69	4846.80	0.11
A	0.61	4846.80	4846.87	0.07
C	3.49	4846.87	4847.07	0.20
A	0.77	4847.07	4847.32	0.25
B	0.10	4847.32	4847.69	0.37
A	0.24	4847.69	4848.00	0.31
C	3.80	4848.00	4848.07	0.07
A	0.37	4848.07	4849.15	1.08
B	1.59	4849.15	4849.32	0.17
A	0.57	4849.32	4850.09	0.77
C	3.74	4850.09	4850.19	0.10
B	1.71	4850.19	4850.25	0.06
Core Break	0.00	4850.25	4852.00	1.75
B	1.58	4852.00	4852.46	0.46
A	0.06	4852.46	4852.61	0.15
C	3.73	4852.61	4852.71	0.10
A	0.40	4852.71	4852.89	0.18
B	0.02	4852.89	4853.12	0.23
A	0.13	4853.12	4853.23	0.11
D	0.32	4853.23	4853.47	0.24
A	0.21	4853.47	4854.24	0.77
A	0.70	4854.24	4854.60	0.36
B	0.96	4854.60	4854.71	0.11
A	0.09	4854.71	4854.87	0.16
C	3.60	4854.87	4855.02	0.15

<b>Facies</b>	<b>Effective Perm (mD)</b>	<b>Top (ft)</b>	<b>Bottom (ft)</b>	<b>Thickness (ft)</b>
B	0.08	4855.02	4855.48	0.46
B	0.07	4855.48	4855.67	0.19
C	3.79	4855.67	4855.74	0.07
B	0.59	4855.74	4855.92	0.18
D	0.32	4855.92	4856.31	0.39
D	1.14	4856.31	4856.45	0.14
D	0.31	4856.45	4856.69	0.24
A	0.02	4856.69	4856.79	0.10
A	0.34	4856.79	4856.94	0.15
B	0.01	4856.94	4857.07	0.13
B	0.08	4857.07	4857.46	0.39
D	0.32	4857.46	4857.70	0.24
B	0.02	4857.70	4857.83	0.13
A	0.30	4857.83	4858.38	0.55
B	0.72	4858.38	4858.48	0.10
A	0.17	4858.48	4858.78	0.30
C	3.12	4858.78	4859.20	0.42
A	0.23	4859.20	4859.41	0.21
B	0.22	4859.41	4859.52	0.11
C	3.49	4859.52	4859.73	0.21
B	0.13	4859.73	4860.33	0.60
B	0.51	4860.33	4860.73	0.40
A	0.29	4860.73	4860.92	0.19
A	0.60	4860.92	4861.12	0.20
B	1.16	4861.12	4861.20	0.08
A	0.33	4861.20	4861.50	0.30
B	0.93	4861.50	4861.71	0.21
A	0.19	4861.71	4862.11	0.40
C	2.51	4862.11	4863.31	1.20
B	0.12	4863.31	4863.36	0.05
C	3.77	4863.36	4863.45	0.09
B	0.90	4863.45	4863.91	0.46
B	1.49	4863.91	4864.61	0.70
B	0.10	4864.61	4864.73	0.12
D	0.33	4864.73	4864.88	0.15
B	0.08	4864.88	4865.09	0.21
C	3.74	4865.09	4865.18	0.09
A	0.53	4865.18	4865.25	0.07
C	3.63	4865.25	4865.39	0.14
A	0.20	4865.39	4865.68	0.29
D	0.33	4865.68	4865.80	0.12
A	0.27	4865.80	4866.04	0.24
C	3.59	4866.04	4866.20	0.16
A	0.08	4866.20	4866.50	0.30
A	0.08	4866.50	4866.66	0.16
B	1.25	4866.66	4866.97	0.31
C	3.56	4866.97	4867.14	0.17
A	0.33	4867.14	4867.38	0.24
B	1.74	4867.38	4867.52	0.14
A	0.17	4867.52	4867.56	0.04
C	3.48	4867.56	4867.77	0.21
A	0.19	4867.77	4867.85	0.08
B	0.10	4867.85	4868.46	0.61
A	0.13	4868.46	4868.78	0.32
A	0.22	4868.78	4868.96	0.18
C	3.65	4868.96	4869.09	0.13
B	1.55	4869.09	4869.14	0.05

<b>Facies</b>	<b>Effective Perm (mD)</b>	<b>Top (ft)</b>	<b>Bottom (ft)</b>	<b>Thickness (ft)</b>
D	0.32	4869.14	4869.35	0.21
A	0.22	4869.35	4869.47	0.12
C	3.51	4869.47	4869.66	0.19
B	0.82	4869.66	4869.80	0.14
B	0.04	4869.80	4870.07	0.27
A	0.22	4870.07	4870.30	0.23
A	0.43	4870.30	4871.03	0.73
C	3.57	4871.03	4871.20	0.17
A	0.10	4871.20	4871.33	0.13
C	3.55	4871.33	4871.50	0.17
Core Break	0.00	4871.50	4872.00	0.50
C	3.27	4872.00	4872.33	0.33
A	0.32	4872.33	4872.72	0.39
B	0.35	4872.72	4872.82	0.10
C	3.47	4872.82	4873.03	0.21
A	0.13	4873.03	4873.13	0.10
C	3.84	4873.13	4873.19	0.06
A	0.29	4873.19	4873.32	0.13
C	3.71	4873.32	4873.43	0.11
A	0.17	4873.43	4873.47	0.04
D	0.31	4873.47	4873.77	0.30
A	0.39	4873.77	4874.09	0.32
C	3.74	4874.09	4874.19	0.10
A	0.14	4874.19	4874.45	0.26
C	3.81	4874.45	4874.52	0.07
A	0.18	4874.52	4874.90	0.38
C	3.51	4874.90	4875.10	0.20
D	0.20	4875.10	4875.23	0.13
A	0.42	4875.23	4875.51	0.28
C	3.09	4875.51	4875.96	0.45
A	0.15	4875.96	4876.05	0.09
C	3.71	4876.05	4876.16	0.11
B	0.22	4876.16	4876.30	0.14
A	0.26	4876.30	4876.35	0.05
C	3.75	4876.35	4876.44	0.09
A	0.14	4876.44	4876.57	0.13
A	0.52	4876.57	4876.64	0.07
A	0.19	4876.64	4876.92	0.28
A	0.25	4876.92	4877.17	0.25
A	0.24	4877.17	4877.37	0.20
A	0.23	4877.37	4877.77	0.40
A	0.30	4877.77	4878.15	0.38
A	0.23	4878.15	4878.70	0.55
C	3.30	4878.70	4879.01	0.31
D	0.32	4879.01	4879.26	0.25
A	0.36	4879.26	4880.35	1.09
B	0.33	4880.35	4880.42	0.07
C	3.74	4880.42	4880.52	0.10
A	0.16	4880.52	4882.06	1.54
B	0.04	4882.06	4882.20	0.14
A	0.10	4882.20	4883.25	1.05

Table 5. Upscaled results from Champlin 369 core. (N=161)

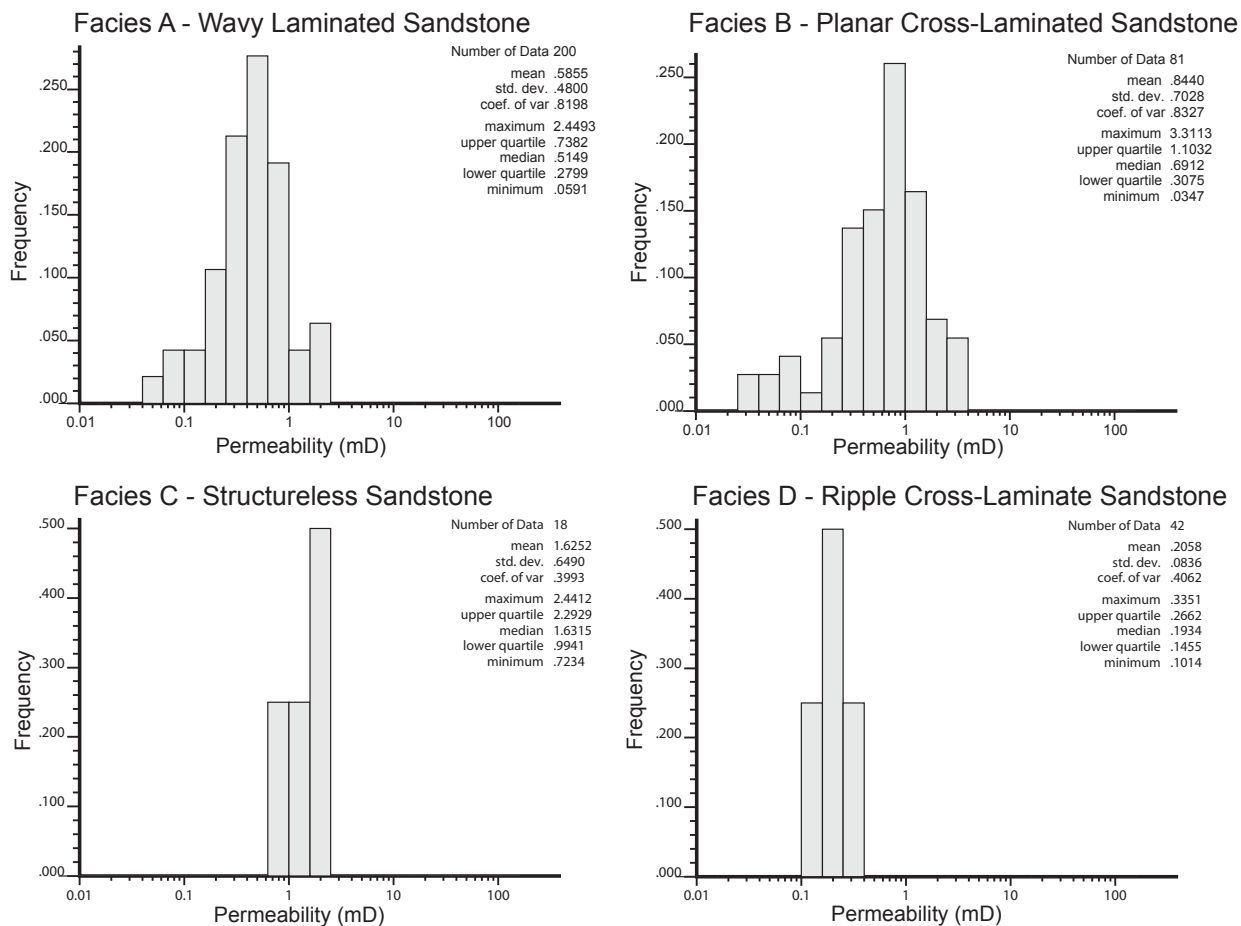


Figure 33. Frequency histograms of permeabilities originally measured for the Terry Formation in the McHale #1 and Moser #1 cores. This data is used to populate 3-D original-permeability models. Permeabilities are calibrated values and assigned to facies based on core descriptions.

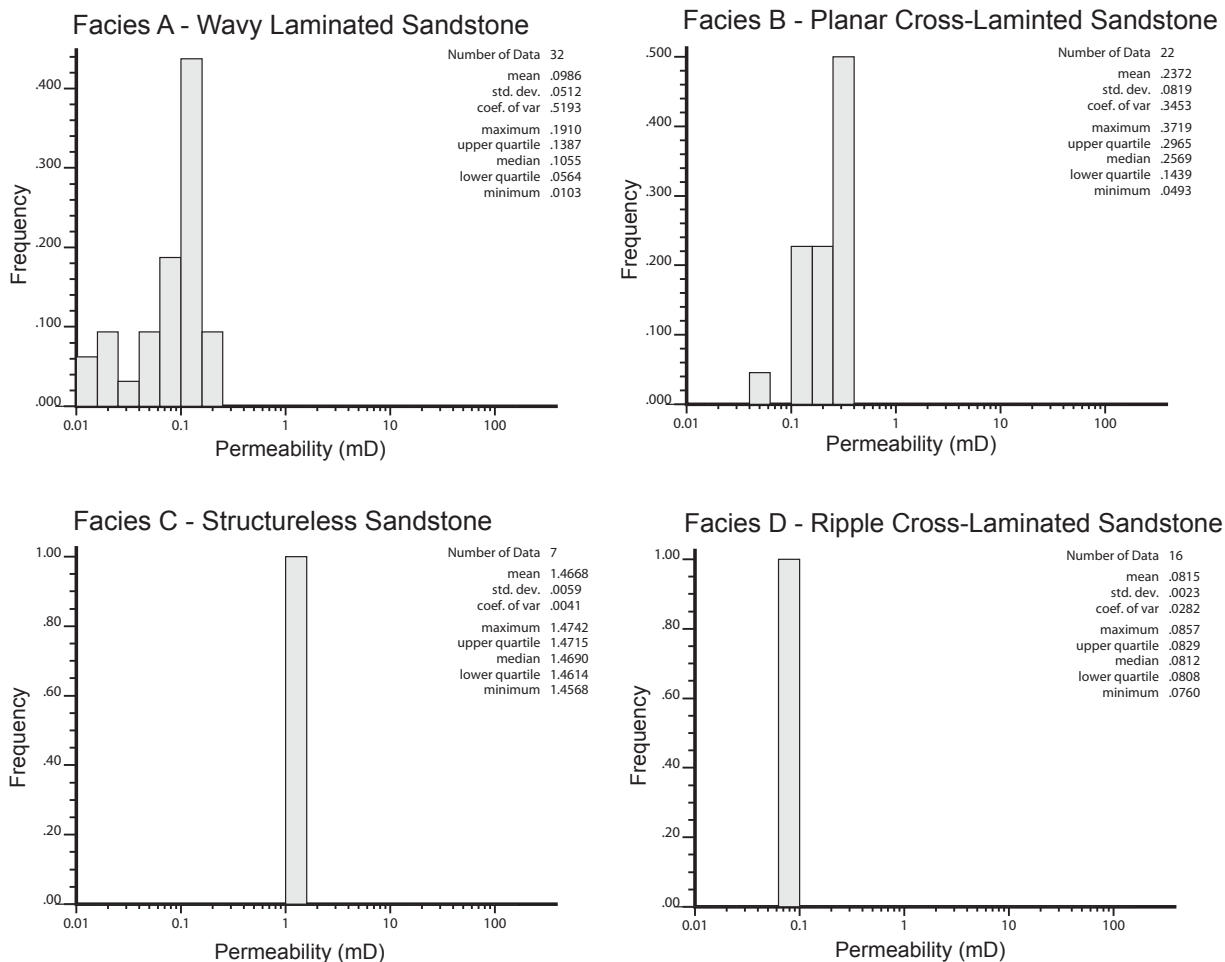


Figure 34. Frequency histograms of permeability values generated for the Terry Formation during the upscaling process in the McHale #1 core. Effective permeabilities show a narrowed range compared to original values and decreased mean effective-permeability values for all facies.



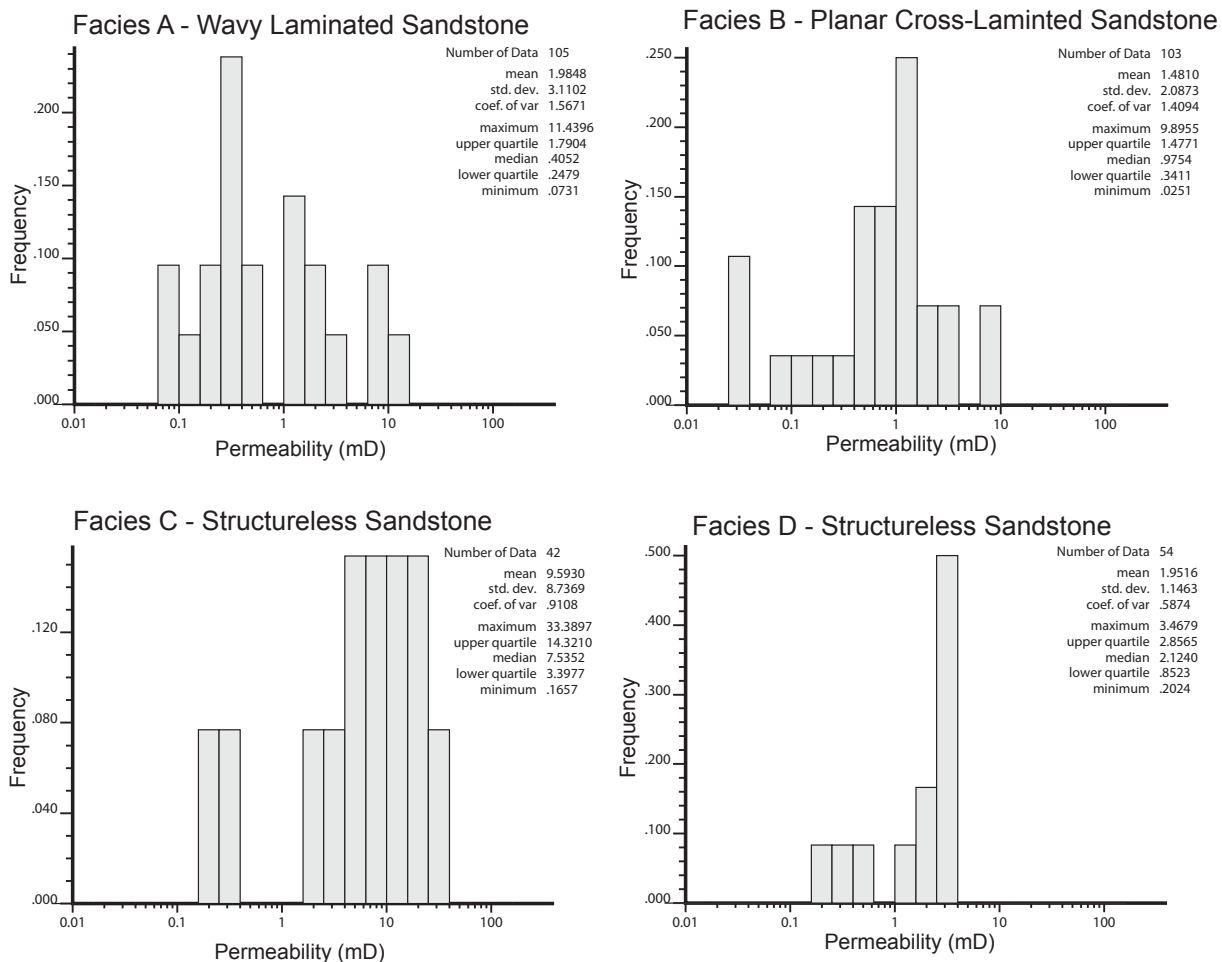


Figure 35. Frequency histograms of permeabilities originally measured for the Hygiene Formation in the Champlin 369 and Sidwell #1 cores. This data is used to populate 3-D original-permeability models. Permeabilities are calibrated values and are assigned to facies based on core descriptions.

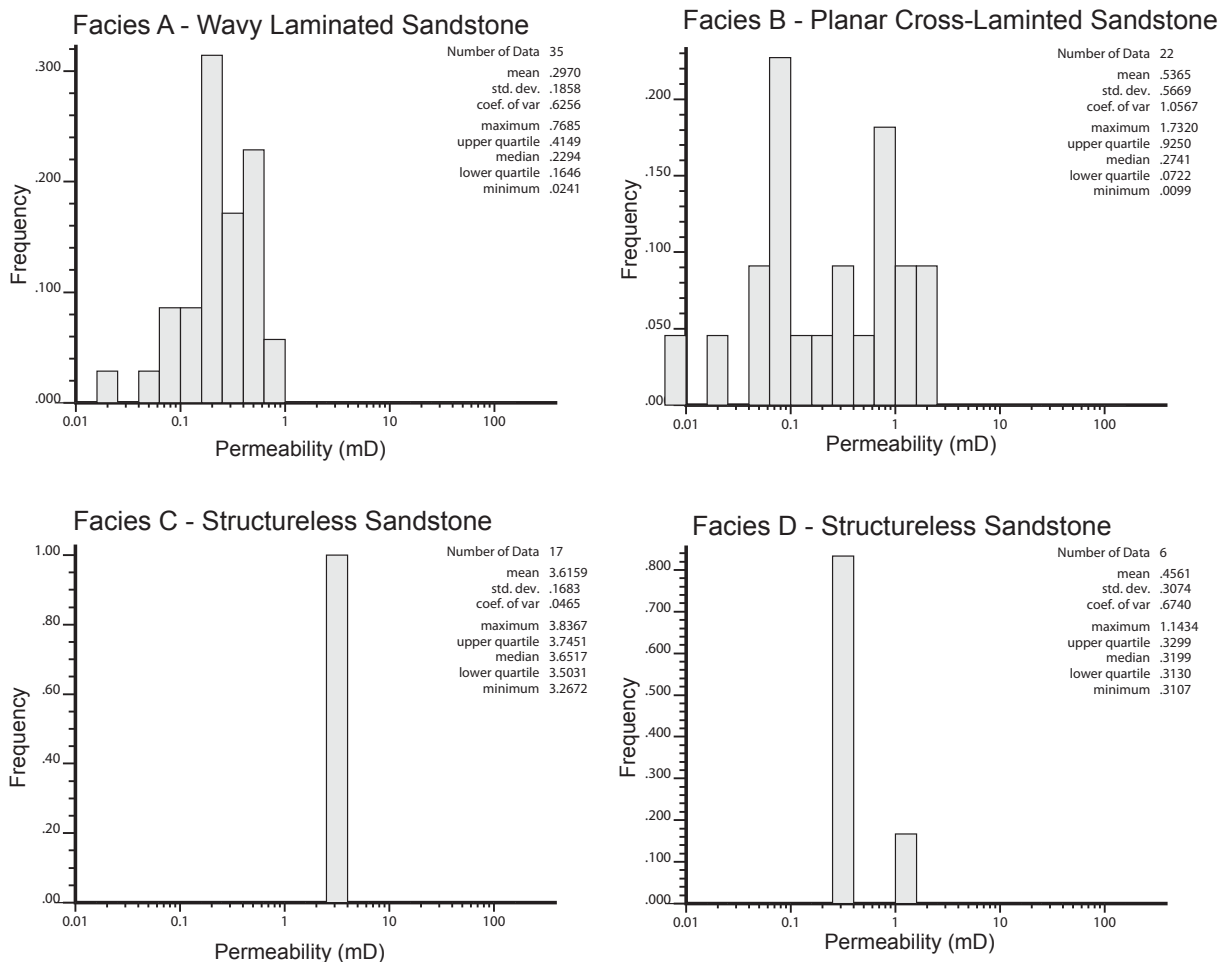


Figure 36. Frequency histograms of permeability values for the Hygiene Formation generated during the upscaling process for the Champlin 369 core. Effective permeabilities show a narrowed range compared to original values and decreased mean effective permeability values for all facies.

## **Appendix D**

### **Field-scale Modeling**

### ***Well-log Data***

For the field-scale modeling, well-log data is used as the primary input data. The one exception is the permeability modeling in which permeability data is obtained from cores. Digital well-log data was obtained for all nine wells within the model area (Figure 2). The primary well-log curves used in this study were GR, SP, RESD, and DPHI. GR, SP. The RESD logs were used to determine reservoir zonation. Additionally, SP logs were used to create a volume probability model for each facies as SP correlates with the relative amounts of each facies within a zone. Density-porosity logs were used to create the porosity models for this study. While it is preferable to use additional porosity logs (e.g. neutron-porosity or sonic-porosity logs), only select wells had those logs. It was decided to only use density-porosity logs so that porosity values in all wells were based on similar data sets. Finally, 3-D field scale models were related back to the McHale #1 logs of the Terry Formation by normalizing the log responses to the logs in the McHale #1 well. The normalization process involved stretching and compressing the well-log curves for the other wells in the study area to the same range as in the McHale #1 log. This allows for the overall shape of the log curve to remain the same with high values still being high and low values still being low relative to the original log curve. The high and low values are determined automatically from the logs for the McHale #1 core.

### ***Model Framework***

It is necessary to accurately create a stratigraphic framework for 3-D reservoir models. In this case, the study area is approximately 2828 ft by 2900 ft (length, width; 826 x 887 m; Figure 2) and includes the Terry Formation which varies in thickness but averages approximately 25 ft (6.2 m) (Weimer, 1997). The cell size based on these measurements is 29.8 x 30 x 1 ft (9.08 x 9.1 x 0.3 m) for each individual cell in the model area. To create the layering within the model, five stratigraphic horizons were interpreted based on well log and core-to-log comparisons (Figure 5; Table 6). These stratigraphic horizons define four zones within the

API	Well name	Measured Depth (ft)							
		Top Terry	Terry A	Terry_B	Terry_C	Base Terry	Hygiene	Base Hygiene	
05123076430000	McHale #1	4692.9	4694.5	4703.5	4710.2	4717.7	--	--	
05123078320000	Hart B Unit #1	4656.0	4658.2	4668.7	4672.5	4682.8	--	--	
05123089400000	Vonasek Unit C #2	4676.0	4680.1	4691.3	4699.4	4707.6	--	--	
05123147970000	Weld Co. Pooling Unit #2	4690.3	4692.8	4705.0	4710.0	4719.7	5229.0	--	
05123089980000	McHale #3	4688.0	4692.7	4704.3	4713.0	4722.2	--	--	
05123089730000	McHale #4	4685.7	4687.7	4700.7	4708.5	4720.0	--	--	
05123089590000	Champlin #1-35	4673.8	4676.1	4685.6	4694.4	4701.7	--	--	
05123090960000	UPRR 42 Pan Am AF #3	4689.6	4691.4	4705.5	4710.6	4720.1	--	--	
05123208600000	Newton #3-35A	4743.5	4748.7	4756.7	4761.8	4770.0	5122.0	--	
05123076670000	Montoya #1	4748.8	4754.8	4764.4	4769.2	4780.5	--	--	
05123090540000	Champlin 369 *	4463.3	--	--	--	4514.6	4834.3	4882.9	
05123074700000	Moser #1 *	4431	--	--	--	--	--	--	
05123079080000	Sidwell #1 *	4366	--	--	--	--	4838	--	

Table 6. Stratigraphic horizons determined for all wells used in this study. Wells denoted with astrick (\*) are only used for permeability acquisition. Remaining wells used in field-scale 3-D models.

model area that are then broken down into layers that define the cell size in the model. The number of layers within each zone was determined to give each cell an approximate 1 ft thickness (Table 7). It is important to have each cell in the 3-D model sized appropriately for the scale of the structures that are trying to be modeled. Based on limited outcrop availability and research, the vertical cell size of 1 ft was determined to be large enough to represent the vertical variability of the facies but also small enough as to not lump all of the permeability data heterogeneities which is on a much smaller scale.

### ***SP Volume Probability and Facies Modeling***

The lack of facies log data across the model area inhibited the use of variograms for controlling facies lateral distributions. Instead, control on facies distribution was obtained by using a SP-derived lithology probability volume model. This probability model is a 3-D model the same size as the other models used in this study. Each cell is given a probability for containing either a sandstone-rich or sandstone-poor facies. This probability was determined using the correlation between facies and SP log response (Figure 37). The SP logs from all 9 wells were used to create a SP model that was then rescaled from zero to one depending on whether it was being used as a probability model for sandstone-rich or sandstone-poor facies. For the sandstone-rich facies, the more negative the SP values the cleaner the sandstone, which implies that the most negative SP values coincide with the structureless sandstone facies. The intermediate SP values, where the log curve is moving from zero toward the low end of the sandstone-rich facies, contain more mudrock (e.g. facies B and D). The B, C, and D facies could all be modeled with a single lithology probability volume model (Figure 9); however a new lithology probability volume model had to be created for the sandstone-poor facies (Figure 37). This model appears as the inverse of the sandstone-rich lithology probability volume model and is created in a similar way with the SP log values being closer to zero when the sandstone-poor facies is present (Figure 37).

<b>Zone #</b>	<b>Zone</b>	<b>Layering Scheme</b>	<b>Number of Layers</b>
1	Top Terry to Terry_A (Non-reservoir)	Proportional	8
2	Terry_A to Terry_B (Reservoir)	Proportional	16
3	Terry_B to Terry_C (Non-reservoir)	Proportional	10
4	Terry_C to Base_Terry (Reservoir)	Proportional	10

Table 7. Layering scheme sorted by zone within the 3-D model framework. Layers average 1 ft (0.3 m) thickness.

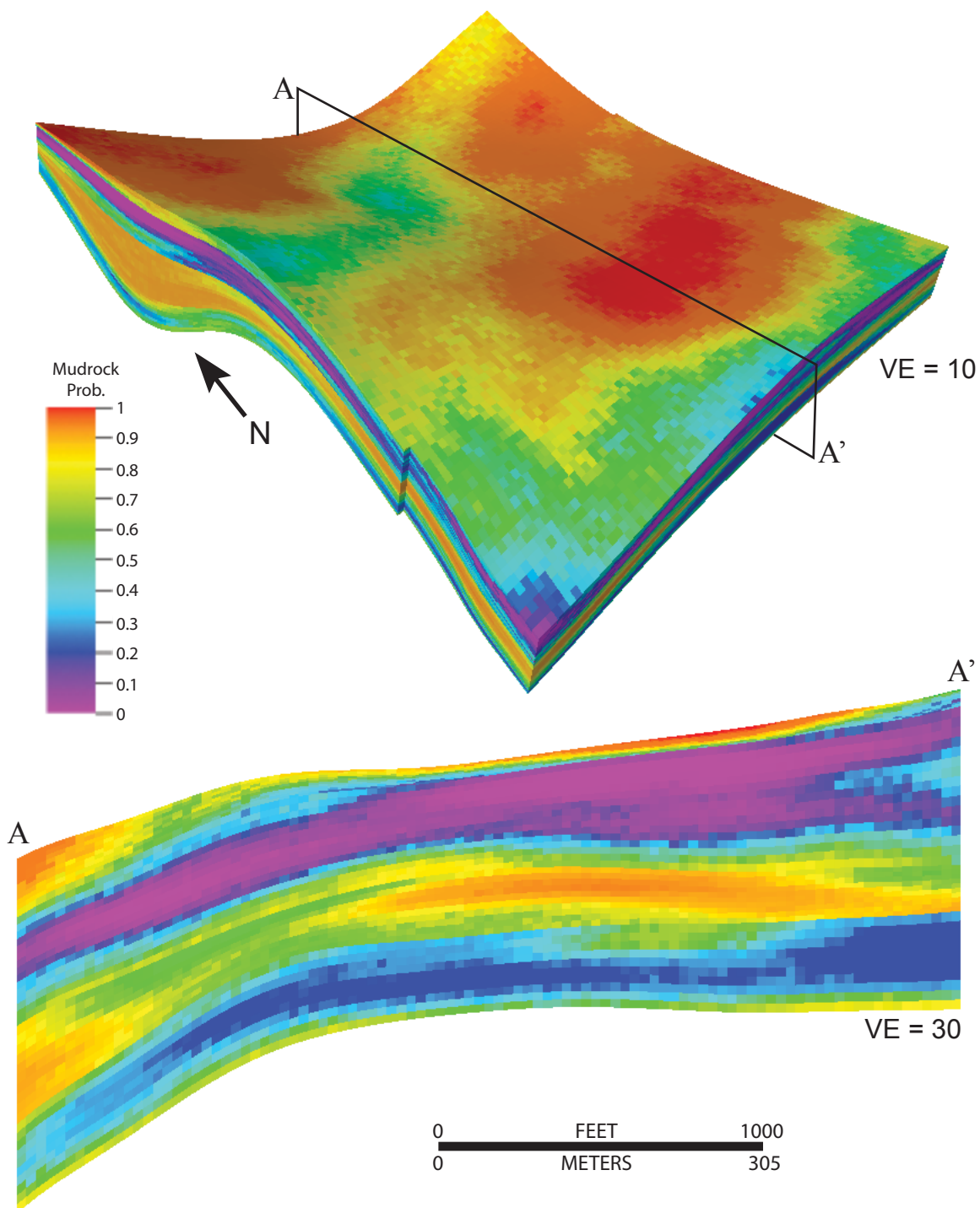


Figure 37. SP mud-rich facies volume probability model (SSMP) used to constrain wavy laminated sandstone facies distribution. Higher values indicate a higher probability of mud-rich facies.



To complete the facies modeling, each facies was assigned to its respective sandstone-rich or sandstone-poor lithology probability volume model to control its lateral distribution. Each lateral facies variogram utilized a spherical variogram and assumed major and minor ranges of 500 ft (152.4 m) with no nugget. In the vertical direction, a traditional variogram was used to control vertical spatial distribution (Table 8). The vertical variogram was determined using the cored McHale #1 well with the vertical range set for each individual facies in each zone separately (Table 8). All four facies were not present in each zone and are modeled accordingly.

The field-scale facies models were created using the sequential-Gaussian simulation (SGS) algorithm. This is a stochastic process-based modeling technique that uses variograms and other geostatistics to spatially distribute the facies (Delbari, 2009). Additionally, SGS honors the original input data of facies so the percentage of facies in the entire model is the same or nearly the same as the numbers in the original McHale #1 facies log (Figure 38). While variograms were used in this process, the lithology probability volume models were the primary control on lateral distributions. The variograms primarily determine the level of heterogeneity within the larger geobodies determined by the lithology probability volume models.

Using all of this information, two types of facies models were created, a model that was derived from a single modeling attempt and a combination of thirty facies models in which thirty realizations are generated and, for a given cell, the facies that occurs most often in the thirty realizations is assigned to that cell. These are referenced herein as the single facies model (SFM) and the average facies model (AFM). The AFM model was generated in an attempt at creating a modeling similar to one that might be generated using a krigging algorithm. The AFM model is preferred for this study as it generates a smoother distribution of facies throughout the model and does not appear as heterogeneous within a given facies body (Figure 11). This was assumed to be a more accurate facies model based on limited outcrop data and is the facies model used going forward. The outcrop data that is available suggests the facies are likely continuous at the scale greater than 10-30 ft (3.0-9.1 m). Outcrops were observed at Water

<b>Zone</b>	<b>Facies</b>	<b>Variogram Model</b>	<b>Maximum Range (ft)</b>	<b>Minimum Range (ft)</b>	<b>Vertical Range (ft)</b>
1	Facies A	Spherical	500	500	1.1
	Facies B	N/A			
	Facies C	N/A			
	Facies D	Spherical	500	500	2.0
2	Facies A	Spherical	500	500	4.5
	Facies B	Spherical	500	500	8.3
	Facies C	Spherical	500	500	3.6
	Facies D	Spherical	500	500	4.9
3	Facies A	Spherical	500	500	7.7
	Facies B	Spherical	500	500	7.8
	Facies C	N/A			
	Facies D	Spherical	500	500	2.7
4	Facies A	Spherical	500	500	4.5
	Facies B	N/A			
	Facies C	Spherical	500	500	3.8
	Facies D	Spherical	500	500	3.4

Table 8. Detailed summary of maximum and minimum horizontal and vertical ranges used in facies modeling as determined from the McHale #1 facies log (vertical) and limited outcrop data (horizontal).

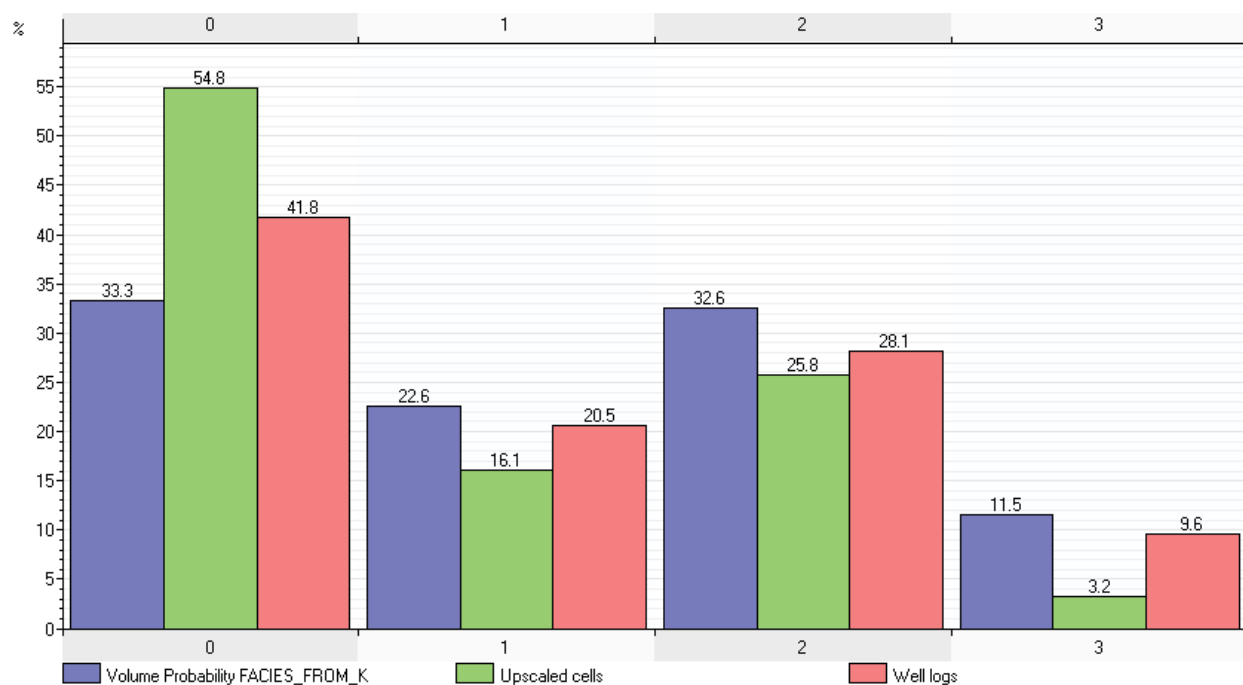


Figure 38. Facies histogram showing the percentage of facies from the McHale #1 core (red), upscaled model cells (green), and the entire AFM model (purple). The relative percentages of each facies is approximately the same throughout the entire modeling process as the facies log on the McHale #1 well is upscaled and then modeled across the entire area.

Supply and Storage Reservoir Number 3 located 5.5 mi (8.9 km) north of Fort Collins, Colorado (Figure 39). Due to limited access and water levels, the upper portion of the Terry formation was only observed from across a channel but continuous beds were visible.

### ***Petrophysical Modeling***

Porosity modeling was completed using the sequential indicator simulation (SIS) algorithm. Density-porosity logs were the primary input for the porosity modeling and were derived from eight of the nine wells in the model area. As mentioned previously, only density-porosity logs were used as there was a lack of other porosity logs to substitute or combine with the density-porosity logs. The distribution of porosity in the entire model area generally matches what the original histogram of porosity values from the well logs indicates is in the model area (Figure 40). A single porosity realization was generated along with an average of thirty porosity realizations. Each of these two types was biased towards the average facies model as porosity variations among reservoir zones and thus facies is observed in well-log data. Like facies modeling, variograms were also used to control the lateral and vertical variability and distribution (Table 9) with the vertical variograms being determined from the McHale #1 well. Horizontal variograms used spherical variogram with assumed major and minor ranges of 250 ft (76 m).

Permeability modeling was completed after porosity modeling in a similar fashion by using the SIS algorithm. However, unlike the porosity models, only a single permeability log for the McHale #1 well exists within the model area. One solution to this problem would involve correlating permeability data to porosity data and having the porosity model control the distribution of the permeability data. However, due to the different measurement techniques (mini-permeameter vs. well-log), the scale of investigation for porosity and permeability measurements is dramatically different (several cubic centimeters and several cubic feet respectively). This in turn results in no correlation between permeability and porosity or other well-log data (Figure 41). The solution to this problem was a bivariate transformation (cloud

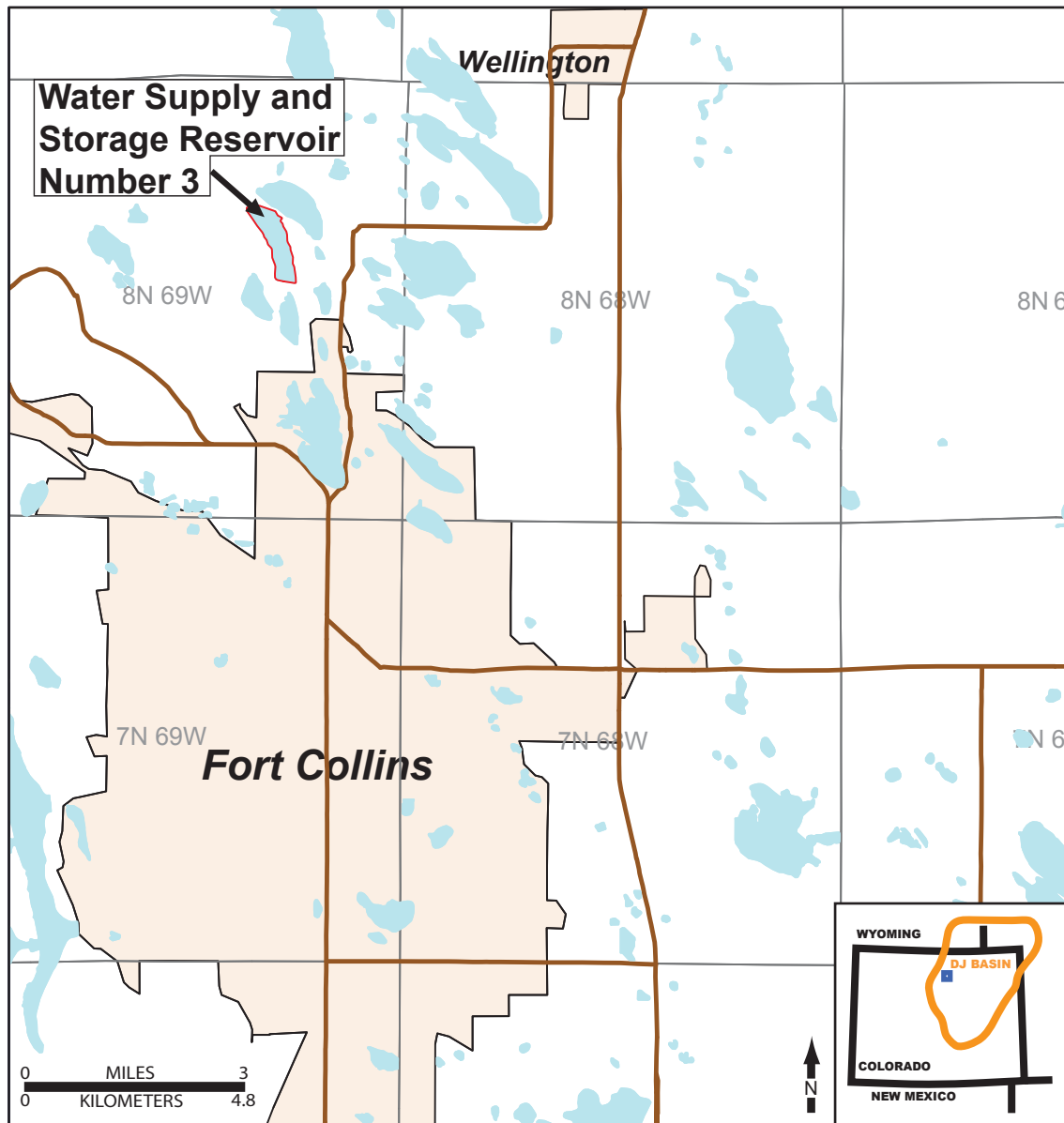


Figure 39. Map showing Water Supply and Storage Reservoir Number 3 (outlined in red) located 5.5 mi (8.9 km) north of Fort Collins, Colorado. Location shown on inset map. Terry outcrop is located on the northeast corner of the lake along a diversion channel.

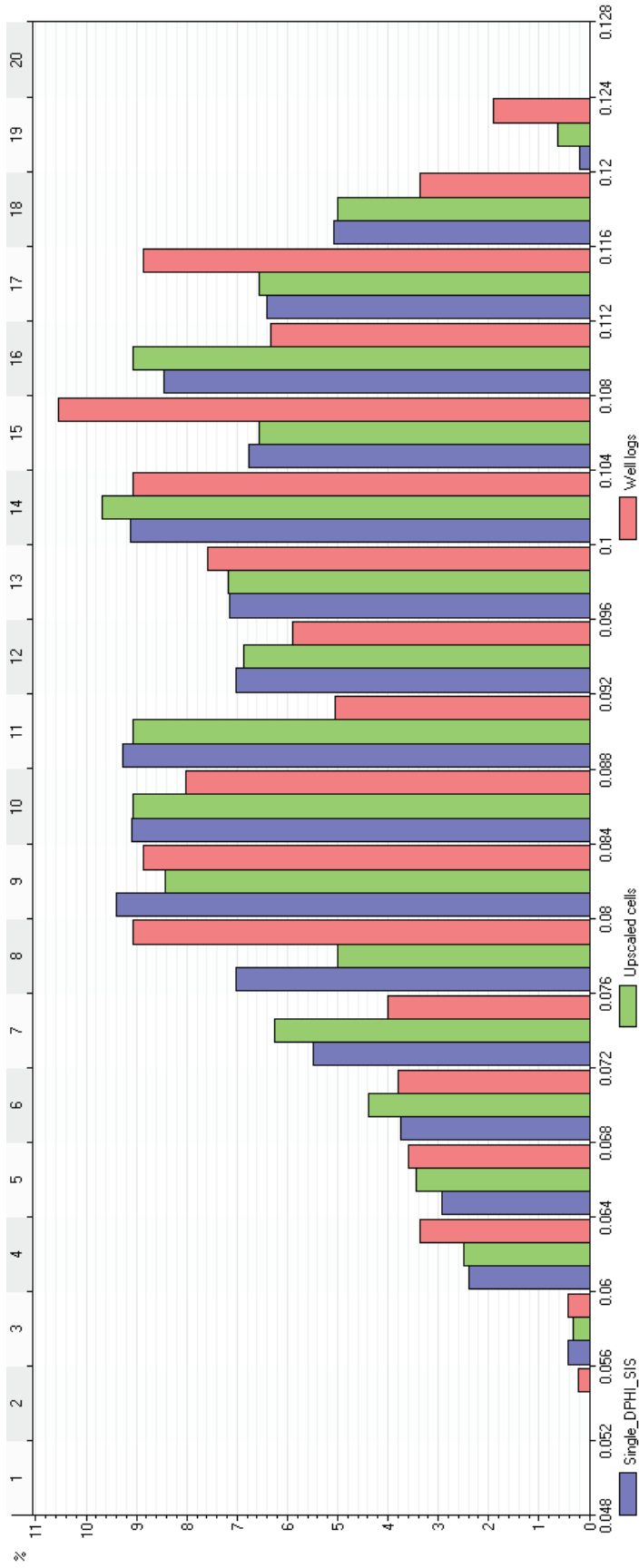


Figure 40. Porosity histogram showing the range of porosity values in well logs (blue), upscaled cells (well logs, green), and all model cells (red). The distribution for all three is nearly identical with both the upscaled cells and the model cells honoring the input data. Porosity values on the x-axis are measured in decimals.

<b>Zone</b>	<b>Facies</b>	<b>Variogram Model</b>	<b>Maximum Range (ft)</b>	<b>Minimum Range (ft)</b>	<b>Vertical Range (ft)</b>
1	Facies A	Spherical	250	250	1.3
	Facies B	N/A			
	Facies C	N/A			
	Facies D	Spherical	250	250	2.0
2	Facies A	Spherical	250	250	7.3
	Facies B	Spherical	250	250	4.8
	Facies C	Spherical	250	250	1.3
	Facies D	Spherical	250	250	4.2
3	Facies A	Spherical	250	250	7.1
	Facies B	Spherical	250	250	3.3
	Facies C	N/A			
	Facies D	Spherical	250	250	1.6
4	Facies A	Spherical	250	250	5.4
	Facies B	N/A			
	Facies C	Spherical	250	250	6.0
	Facies D	Spherical	250	250	0.6

Table 9. Detailed summary of maximum and minimum horizontal ranges and vertical ranges used in porosity modeling. Vertical ranges from variogram based on density porosity log of McHale #1 well. Horizontal ranges assumed based on limited outcrop data.

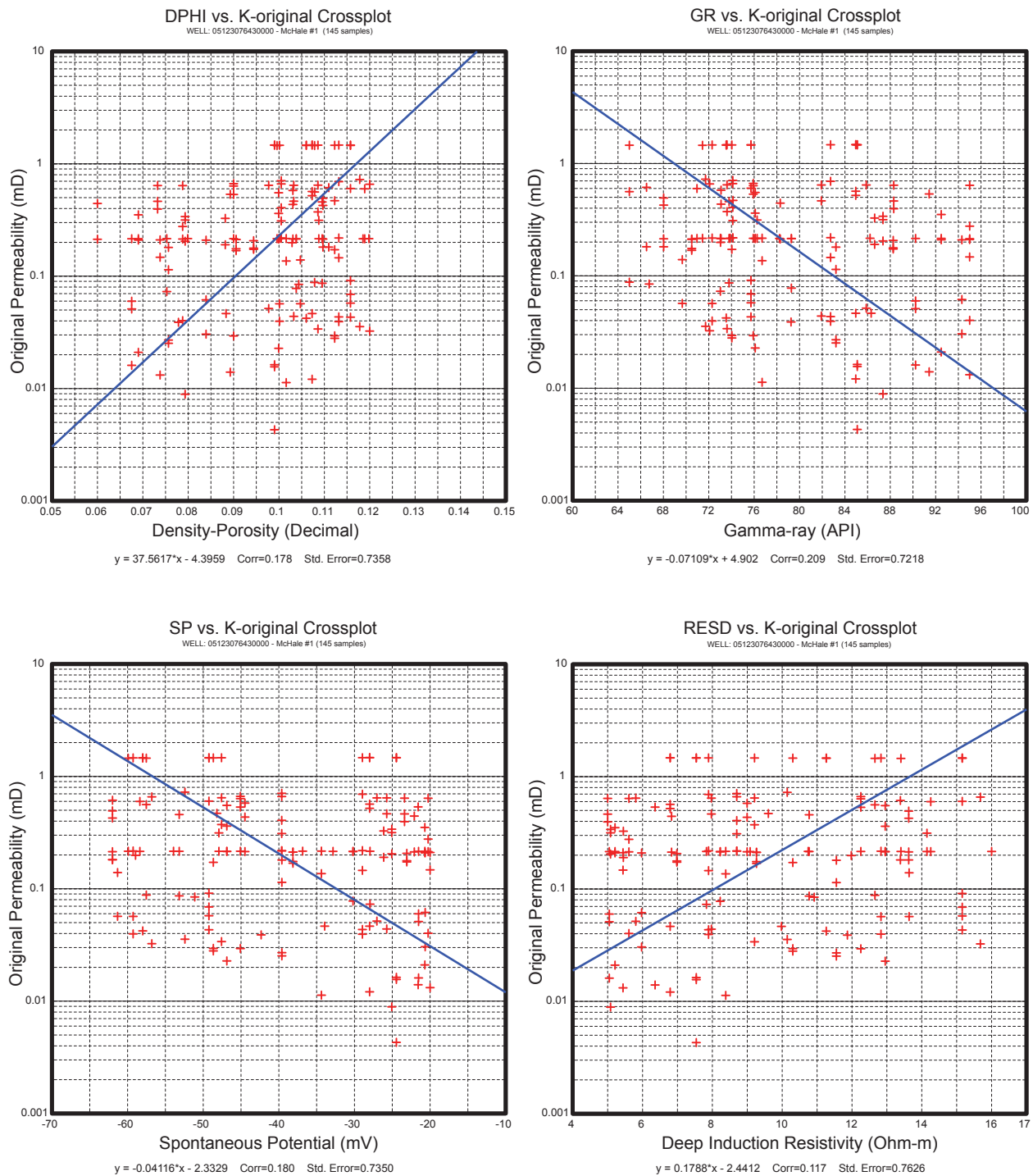


Figure 41. Well-log crossplots showing the lack of a relationship between original permeability and well-log measured properties. Upper left: Density porosity vs. Permeability. Upper right: Gamma-ray vs. Permeability. Lower left: Spontaneous potential vs. Permeability. Lower right: Deep resistivity vs. Permeability. Blue line=line of best fit, equation displayed below each graph.



transformation) that links the permeability values to the porosity values despite the lack of correlation between the two. This method entails creating a porosity and permeability cross-plot and defining a series of bins based on the porosity values (Figure 42). These bins are then sampled and a cumulative frequency histogram is generated in which permeability values are linked to the porosity values. This cross-plot and bin data is then used to produce a permeability value for a cell based on the corresponding cell in the porosity model. As this study used two different permeability types (e.g. original and effective permeabilities), two cross-plots were generated (Figure 42). For each permeability type, a single permeability realization and an average of thirty permeability realizations was produced. The thirty realizations tends to give a smoother distribution of permeabilities that grade into higher or lower values without random values. Due to the lack of data determining which distribution is correct in the permeability models, all four permeabilities models were explored for static connectivity to determine how upscaling of permeability might affect reservoir modeling.

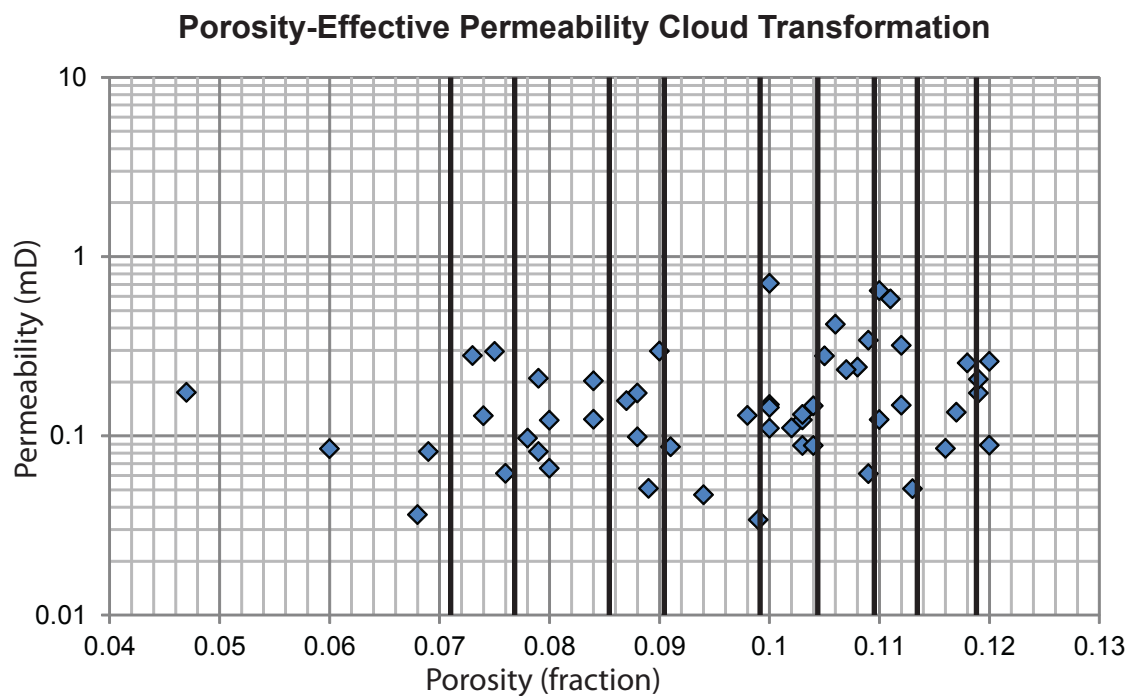
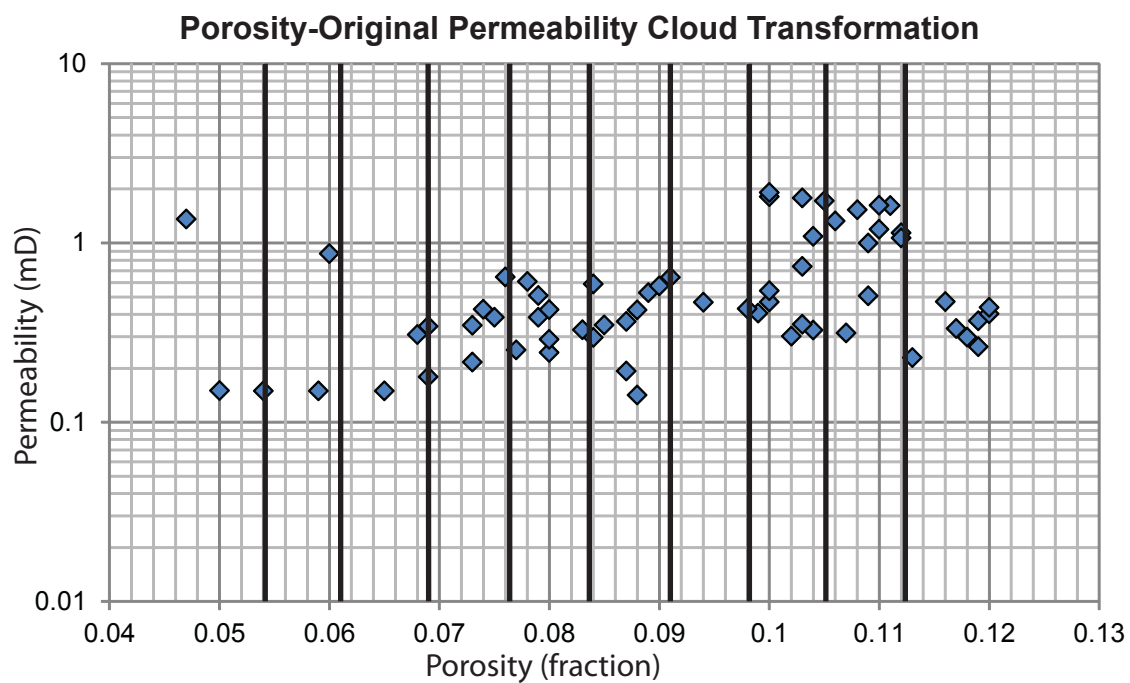


Figure 42. Porosity-permeability crossplots used to create a cloud transformation (bivariate transformation) to link permeability to porosity. Dark black lines indicate bins used for transformation.

## **Appendix E**

Static Connectivity

### ***Static Connectivity Model Area***

Static connectivity to a wellbore is used herein to compare how reservoirs are affected by using effective-permeabilities derived from flow-based upscaling techniques and by using unaltered original-permeability measurements. To start the comparison, pseudowells were added to the model area and the model area was reduced in size (Figure 2). The reduction in size was done to eliminate or reduce potential errors associated with edge-effects created during the previous modeling of facies, porosity, and permeability. The outside area of each of those models was removed so that cells between the original model boundary and the static connectivity boundary are not considered in static connectivity analysis. Additionally, 20 pseudowells were added that penetrated the entire model in a regular 5-ac (2-hectacre) spacing. These wells were added and used for the static connectivity analysis as there are only a few wells that penetrated the smaller area. Additionally, the regularly spaced wells offer an analogous relationship to infill drilling patterns.

Static connectivity was determined by applying a porosity and permeability cutoff to determine what is and is not a reservoir cell in the reservoir model. These reservoir cells are then analyzed for their spatial arrangement and a determination is made as to whether or not they are connected to a well bore, be it directly (touching the wellbore) or indirectly (touch other cells which touch a wellbore) (Table 10). The connectivity is reported as a bulk volume of the connected cells. This volume is then compared with the model's total bulk volume and a percentage of connectivity is determined. This was done for each of the four permeability models.

Additionally, the bulk volume of all reservoir cells was evaluated for all the permeability models (Table 11). This was done to determine how many of the total reservoir cells in the model are connected to a wellbore at a given permeability cutoff. At the lowest cutoff (1.0 mD), all of the potential reservoir cells that could be connected are connected. This is likely caused by the dense well spacing of the pseudowells in the model area, which likely penetrate each

### Effective Permeability Models

K cutoff (md)	SIS Single	SIS Average	Bulk Model	Connectivity	
				(Single $\Phi$ Model)	(Avg. $\Phi$ Model)
		(ft <sup>3</sup> )			
0	52248992	66518436	83615056	62.49%	79.55%
0.15	15797639	9521457	83615056	18.89%	11.39%
0.3	4164627	130404	83615056	4.98%	0.16%
0.45	38668	15275	83615056	0.05%	0.02%
0.6	11797	7552	83615056	0.01%	0.01%
0.75	502	1004	83615056	0.00%	0.00%
0.9	0	502	83615056	0.00%	0.00%
1.05	0	0	83615056	0.00%	0.00%
1.2	0	0	83615056	0.00%	0.00%
1.35	0	0	83615056	0.00%	0.00%
1.5	0	0	83615056	0.00%	0.00%
1.65	0	0	83615056	0.00%	0.00%
1.8	0	0	83615056	0.00%	0.00%
1.95	0	0	83615056	0.00%	0.00%

### Original Permeability Models

K cutoff (md)	SIS Single	SIS Average	Bulk Model	Connectivity	
				(Single $\Phi$ Model)	(Avg. $\Phi$ Model)
		(ft <sup>3</sup> )			
0	52248992	66518436	83615056	62.49%	79.55%
0.15	52248992	66518436	83615056	62.49%	79.55%
0.3	47819652	49079060	83615056	57.19%	58.70%
0.45	28203824	27510206	83615056	33.73%	32.90%
0.6	7076063	13199585	83615056	8.46%	15.79%
0.75	3744301	7370615	83615056	4.48%	8.81%
0.9	3390688	6777145	83615056	4.06%	8.11%
1.05	2679715	6049038	83615056	3.20%	7.23%
1.2	1794726	4977874	83615056	2.15%	5.95%
1.35	1167196	4507737	83615056	1.40%	5.39%
1.5	480240	4077384	83615056	0.57%	4.88%
1.65	22458	3539519	83615056	0.03%	4.23%
1.8	3758	1163983	83615056	0.00%	1.39%
1.95	502	502	83615056	0.00%	0.00%

Table 10. Static connectivity results from all permeability models. SIS=Porosity Model.

### Effective Permeability Models

K cutoff (md)	SIS Single	SIS Average	Bulk Model	Percent of Total Model	
				(Single $\Phi$ Model)	(Avg. $\Phi$ Model)
		(ft <sup>3</sup> )			
0	52248992	66518436	83615056	62.49%	79.55%
0.15	15797639	11146096	83615056	18.89%	13.33%
0.3	4164627	135081	83615056	4.98%	0.16%
0.45	1691031	16294	83615056	2.02%	0.02%
0.6	723675	8058	83615056	0.87%	0.01%
0.75	1004	1004	83615056	0.00%	0.00%
0.9	502	502	83615056	0.00%	0.00%
1.05	0	0	83615056	0.00%	0.00%
1.2	0	0	83615056	0.00%	0.00%
1.35	0	0	83615056	0.00%	0.00%
1.5	0	0	83615056	0.00%	0.00%
1.65	0	0	83615056	0.00%	0.00%
1.8	0	0	83615056	0.00%	0.00%
1.95	0	0	83615056	0.00%	0.00%

### Original Permeability Models

K cutoff (md)	SIS Single	SIS Average	Bulk Model	Percent of Total Model	
				(Single $\Phi$ Model)	(Avg. $\Phi$ Model)
		(ft <sup>3</sup> )			
0	52248992	66518436	83615056	62.49%	79.55%
0.15	52248992	66518436	83615056	62.49%	79.55%
0.3	47819652	63010816	83615056	57.19%	75.36%
0.45	28203824	35008020	83615056	33.73%	41.87%
0.6	14249642	15109075	83615056	17.04%	18.07%
0.75	8857820	8311898	83615056	10.59%	9.94%
0.9	8362829	7629447	83615056	10.00%	9.12%
1.05	7344968	6806986	83615056	8.78%	8.14%
1.2	4746485	5614799	83615056	5.68%	6.72%
1.35	3769438	5083262	83615056	4.51%	6.08%
1.5	3018834	4606231	83615056	3.61%	5.51%
1.65	1545343	4013858	83615056	1.85%	4.80%
1.8	490346	1294235	83615056	0.59%	1.55%
1.95	502	502	83615056	0.00%	0.00%

Table 11. Bulk volumes for reservoir criteria in the entire model area. SIS=Porosity Model

dense body of reservoir cells. As each petrophysical property model is biased towards the facies model, which shows distinct groupings of reservoir facies (facies consisting mostly of sandstone with higher porosities relative to sandstone-poor facies), the cells that are likely to be defined as reservoir cells would also occur in these groupings. As the permeability cutoff value is increased, differences do appear between the bulk reservoir cell volume and connected reservoir bulk volume (Figure 43). This is due to more individual reservoir cells becoming isolated from other reservoir cells.

Pore volume was evaluated in a similar way as bulk reservoir volume was. A pore-volume model was first created by taking the average porosity model and combining it with the bulk volume model. The result has the pore volume for each cell based on the porosity that was modeled. The total pore volume was then calculated for each of the reservoir cutoffs (porosity >8.75% and a variable permeability variable). The results are then compared to the total pore volume with no restrictions by dividing the pore volume at a given reservoir definition and dividing it by the total pore volume and multiplying by 100. This is then a percentage of total model pore volume (Table 12).

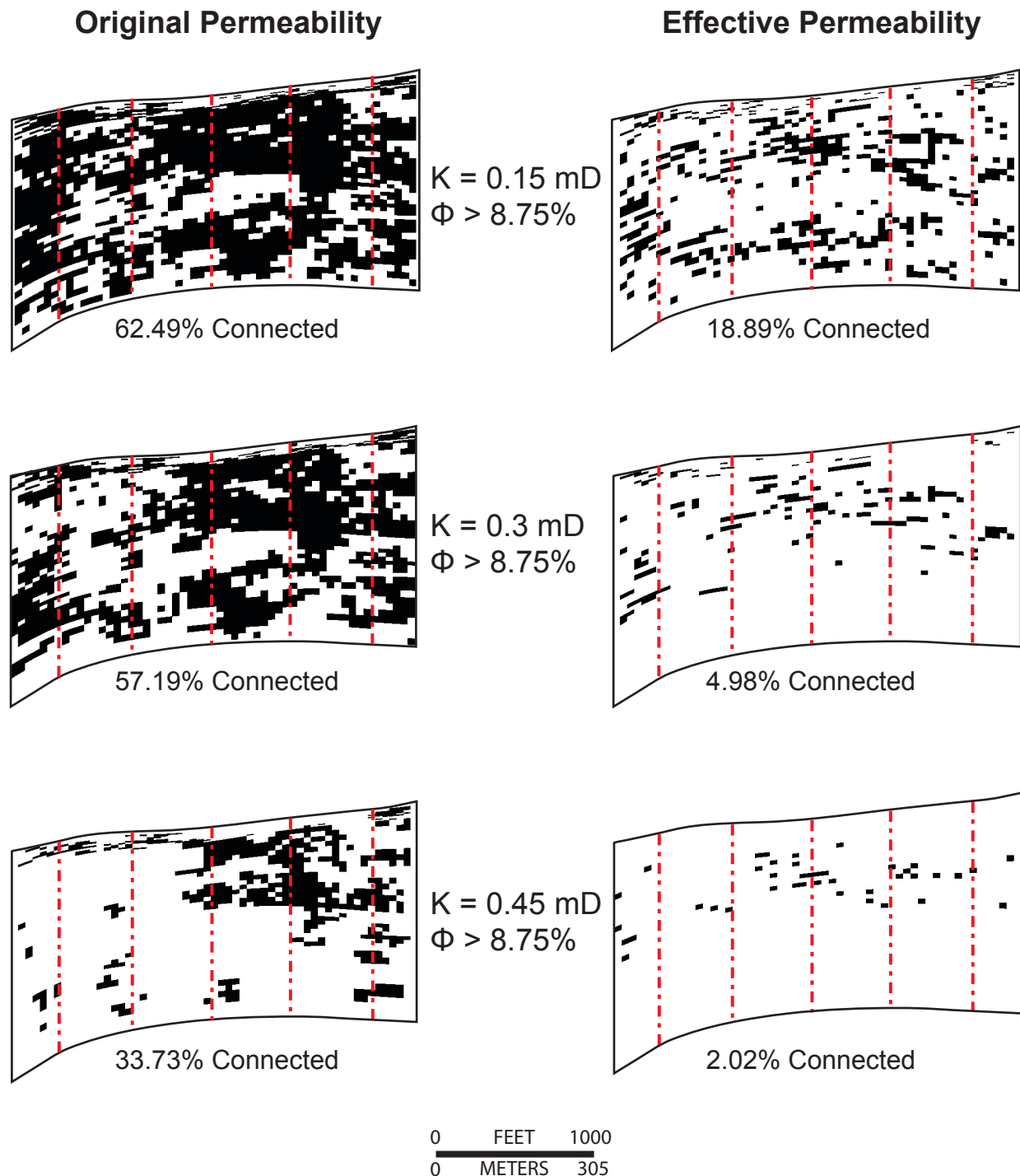


Figure 43. Bulk reservoir volume (expressed as percentage of bulk model volume) comparison in cross-sectional view (cross-sectional plane:  $l=54$ ) of single porosity referenced original- and effective-permeability models. The view shows how many cells in the given plane fit the criteria to be called a reservoir cell. Cross-sectional plane is shown in figure 13 and is consistent with all model cross-sections. Red lines indicate wellbores.  $VE = 30x$



